

ENERGY- AND ANGLE-RESOLVED
INFRARED-LASER-ASSISTED XUV SINGLE- AND
TWO-PHOTON DOUBLE IONIZATION OF HELIUM

by

AIHUA LIU

M.S., University of Science and Technology of China, China, 2007

B.S., China University of Geosciences, China, 2004

AN ABSTRACT OF A DISSERTATION

submitted in partial fulfillment of the
requirements for the degree

DOCTOR OF PHILOSOPHY

Department of Physics
College of Arts and Sciences

KANSAS STATE UNIVERSITY

Manhattan, Kansas

2015

Abstract

Although the latest and most powerful supercomputer today, Tianhe-2 in China, can finish 33.86 quadrillion floating-point operations per second (www.top500.org), it is still a big challenge to simulate the simplest few-electron system - the helium atom - a three-body system with one nucleus and two electrons. Within the fixed-nucleus approximation and time-dependent close coupling (TDCC) approach, we developed software to solve the time-dependent Schrödinger equation (TDSE) accurately, implementing the finite-element discrete-variable representation (FE-DVR) scheme. The general idea of the method is to expand the wave functions in the eigenvectors of the angular momentum operator, which further transform the six-dimensional TDSE to a set of infinite two-dimensional coupled equations. Although there are infinitely many coupled equations, they can be truncated to a finite number of equations by applying selection rules and physical requirements, and solved with our current computational resources.

By numerically solving the TDSE in full dimensionality, we investigate the double photoionization of helium atoms in external fields. In co-planar emission geometry with and without the presence of a comparatively weak infrared (IR) laser pulse, we discuss the double ionization (DI) dynamics of helium atoms irradiated by ultrashort pulses of extreme ultraviolet (XUV) laser light.

We first investigate the degree of electronic correlation by correlated photoelectron angular distributions for two-photon double ionization (TPDI) of helium atoms in the sequential and non-sequential DI regime. We quantify sequential and non-sequential contributions to TPDI driven by an XUV pulse with central photon energy $\hbar\omega_{\text{XUV}}$ near the sequential DI threshold. If the spectral width of the XUV pulse is broad enough, both the sequential ($\hbar\omega_{\text{XUV}} > 54.4$ eV) and non-sequential ($\hbar\omega_{\text{XUV}} < 54.4$ eV) channels are open. Therefore,

the sequential and non-sequential DI mechanisms are difficult to distinguish. By tracking the DI asymmetry in joint photoelectron angular distributions, we introduce the forward-backward-emission asymmetry as a measure that allows the distinction of sequential and non-sequential contributions. Specifically, for $\hbar\omega_{\text{XUV}} = 50$ eV pulses with a sine-squared temporal profile, we find that the sequential DI contribution is the largest at a pulse length of 650 as (1 as = 10^{-18} s), due to competing temporal and spectral constraints. In addition, we validate a simple heuristic expression for the sequential DI contribution in comparison with *ab initio* calculations.

We then investigate the influence of the laser field on the DI of helium by a single XUV pulse. For IR-laser-assisted single-XUV-photon DI our joint angular distributions show that the IR-laser field enhances back-to-back electron emission and induces a characteristic splitting in the angular distribution for electrons that are emitted symmetrically relative to the identical linear polarization directions of the XUV and IR pulse. These IR-pulse-induced changes in photoelectron angular distributions are (i) imposed by different symmetry constraints for XUV-pulse-only and laser-assisted XUV-photon DI, (ii) robust over a large range of energy sharing between the emitted electrons, and (iii) consistent with the transfer of discrete IR-photon momenta to both photoelectrons from the assisting IR-laser field. While selection-rule forbidden at equal energy sharing, for increasingly unequal energy sharing we find back-to-back emission to become more likely and to compete with symmetric emission.

To obtain a high level of accuracy, accurate quantum-mechanical calculations of three Coulomb interacting particles exposed to an intense XUV and weak IR field are at the limit of current computational power. Any direct extension (such as strong laser-field intensity, elliptically-polarized field, and laser-induced DI) of our approach to more complicated systems appears to be currently out of reach. At the end of this thesis, we give suggestions on how to improve the efficiency of TDSE calculations for simulations of these complicated many-photon processes.

ENERGY- AND ANGLE-RESOLVED
INFRARED-LASER-ASSISTED XUV SINGLE- AND
TWO-PHOTON DOUBLE IONIZATION OF HELIUM

by

AIHUA LIU

M.S., University of Science and Technology of China, China, 2007

B.S., China University of Geosciences, China, 2004

A DISSERTATION

submitted in partial fulfillment of the
requirements for the degree

DOCTOR OF PHILOSOPHY

Department of Physics
College of Arts and Sciences

KANSAS STATE UNIVERSITY

Manhattan, Kansas

2015

Approved by:

Major Professor
Uwe Thumm

Copyright

Aihua Liu

© 2015

Abstract

Although the latest and most powerful supercomputer today, Tianhe-2 in China, can finish 33.86 quadrillion floating-point operations per second (www.top500.org), it is still a big challenge to simulate the simplest few-electron system - the helium atom - a three-body system with one nucleus and two electrons. Within the fixed-nucleus approximation and time-dependent close coupling (TDCC) approach, we developed software to solve the time-dependent Schrödinger equation (TDSE) accurately, implementing the finite-element discrete-variable representation (FE-DVR) scheme. The general idea of the method is to expand the wave functions in the eigenvectors of the angular momentum operator, which further transform the six-dimensional TDSE to a set of infinite two-dimensional coupled equations. Although there are infinitely many coupled equations, they can be truncated to a finite number of equations by applying selection rules and physical requirements, and solved with our current computational resources.

By numerically solving the TDSE in full dimensionality, we investigate the double photoionization of helium atoms in external fields. In co-planar emission geometry with and without the presence of a comparatively weak infrared (IR) laser pulse, we discuss the double ionization (DI) dynamics of helium atoms irradiated by ultrashort pulses of extreme ultraviolet (XUV) laser light.

We first investigate the degree of electronic correlation by correlated photoelectron angular distributions for two-photon double ionization (TPDI) of helium atoms in the sequential and non-sequential DI regime. We quantify sequential and non-sequential contributions to TPDI driven by an XUV pulse with central photon energy $\hbar\omega_{\text{XUV}}$ near the sequential DI threshold. If the spectral width of the XUV pulse is broad enough, both the sequential ($\hbar\omega_{\text{XUV}} > 54.4$ eV) and non-sequential ($\hbar\omega_{\text{XUV}} < 54.4$ eV) channels are open. Therefore,

the sequential and non-sequential DI mechanisms are difficult to distinguish. By tracking the DI asymmetry in joint photoelectron angular distributions, we introduce the forward-backward-emission asymmetry as a measure that allows the distinction of sequential and non-sequential contributions. Specifically, for $\hbar\omega_{\text{XUV}} = 50$ eV pulses with a sine-squared temporal profile, we find that the sequential DI contribution is the largest at a pulse length of 650 as (1 as = 10^{-18} s), due to competing temporal and spectral constraints. In addition, we validate a simple heuristic expression for the sequential DI contribution in comparison with *ab initio* calculations.

We then investigate the influence of the laser field on the DI of helium by a single XUV pulse. For IR-laser-assisted single-XUV-photon DI our joint angular distributions show that the IR-laser field enhances back-to-back electron emission and induces a characteristic splitting in the angular distribution for electrons that are emitted symmetrically relative to the identical linear polarization directions of the XUV and IR pulse. These IR-pulse-induced changes in photoelectron angular distributions are (i) imposed by different symmetry constraints for XUV-pulse-only and laser-assisted XUV-photon DI, (ii) robust over a large range of energy sharing between the emitted electrons, and (iii) consistent with the transfer of discrete IR-photon momenta to both photoelectrons from the assisting IR-laser field. While selection-rule forbidden at equal energy sharing, for increasingly unequal energy sharing we find back-to-back emission to become more likely and to compete with symmetric emission.

To obtain a high level of accuracy, accurate quantum-mechanical calculations of three Coulomb interacting particles exposed to an intense XUV and weak IR field are at the limit of current computational power. Any direct extension (such as strong laser-field intensity, elliptically-polarized field, and laser-induced DI) of our approach to more complicated systems appears to be currently out of reach. At the end of this thesis, we give suggestions on how to improve the efficiency of TDSE calculations for simulations of these complicated many-photon processes.

Table of Contents

Table of Contents	viii
List of Figures	xii
List of Tables	xix
Acknowledgements	xxi
Preface	xxii
Abbreviations	xxiii
1 Introduction	1
1.1 History of the Atom	1
1.1.1 Atomic Models	1
1.1.2 History of the Helium Atom	2
1.2 History of the Laser and other Light Sources	3
1.3 Double Photo-Ionization	4
1.3.1 History	4
1.3.2 Emission Patterns	6
1.4 Contents of this Thesis	8
2 Theory and Numerical Implementation	10
2.1 The Time-Dependent Schrödinger Equation	10
2.2 Finite-Element Discrete Variable Representation	12
2.2.1 Discrete Variable Representation	13
2.2.2 Finite-Element Discrete-Variable Representation	15
2.2.3 One-Dimensional Hamiltonian Expression in Finite-Element Discrete-Variable Representation	18
2.3 Single-Active-Electron Model	19
2.3.1 Partial Wave Expansion	20
2.3.2 Particle in External Field	20
2.4 Two-Active-Electron Model	22
2.4.1 General Form of the TDSE for the Helium Atom	22
2.4.2 Radial TDSE and Coefficients of Angular Momentum Coupling Functions	25
2.5 Continuum-State Wave Functions	26
2.6 Physical Variables	28

2.6.1	Total Energy	28
2.6.2	Momentum and Energy Distributions	29
2.6.3	Triple Differential Cross Sections	30
2.6.4	Joint Angular Distribution and Mutual Angular Distribution	31
2.6.5	Emission-Asymmetry Parameter	31
2.7	Symmetry in Joint Angular Distribution	32
2.8	Numerical Convergence Tests	32
3	Application to the Energy levels of Hydrogen Atoms and Helium Atoms with Single-Active Electron Model	34
3.1	Hydrogen Atoms	35
3.2	Helium Atoms with Single-Active-Electron Model	36
3.2.1	Energy Levels	36
4	Helium Photo-Double Ionization by XUV Pulses	42
4.1	Preparing an Initial State	42
4.1.1	Ground State	44
4.1.2	Excited States	45
4.2	Selecting Partial Waves	46
4.2.1	Selection Rules and Symmetries	46
4.3	Single-Photon Double Ionization	50
4.3.1	Triple Differential Cross Sections	51
4.3.2	Joint and Mutual Angular Distributions	53
4.3.3	Angular Distributions	57
4.4	Two-Photon Double Ionization	63
4.4.1	Momentum and Energy Distributions	63
4.4.2	Angular Distributions	65
4.4.3	Total Cross Sections for One- and Two-XUV-Photon Co-planar Emission	70
4.5	Three-Photon Double Ionization	71
4.6	Comparison of Helium XUV Double Ionization by One, Two, and Three Photons	72
4.6.1	Few-photon Double Ionization in a Single XUV Pulse	73
4.6.2	Energy Distributions	73
4.6.3	Angular Distributions	74
4.7	Conclusion of this Chapter	81
5	Distinction of Sequential and Non-Sequential Processes in Two-Photon Double Ionization	83
5.1	Discovery of Non-Sequential Double Ionization	83
5.2	Single-Photon Double Ionization	84
5.3	Sequential and Non-Sequential Two-Photon Double Ionization	84
5.4	Pulse-Duration Dependence of Two-Photon Double Ionization	88

5.5	Yield of Sequential Two-Photon Double Ionization	92
5.6	Heuristic Formula	92
5.7	Emission Asymmetry Parameter and Effective Sequential Double-Ionization Yield	93
5.8	Conclusions of this Chapter	94
6	Laser-Assisted Single-XUV-Photon Double Ionization	96
6.1	XUV Double Ionization in the Presence of an IR Laser Pulse	97
6.1.1	Energy Distributions	97
6.1.2	Angular Distributions for Even and Odd IR Photon Numbers	99
6.1.3	Angular Distributions for Specific Effective IR Photon Numbers	102
6.1.4	Summary of Section 6.1	104
6.2	Energy Sharing Dependence	105
6.2.1	Joint Angular Distributions	106
6.2.2	Mutual Angular Distributions	107
6.2.3	Conclusion of Section 6.2	112
6.3	Intensity Dependence	112
6.3.1	Conclusions of Section 6.3	114
7	Conclusions and Outlook	115
7.1	Summary and Conclusions	115
7.2	Challenges and Outlook	117
7.2.1	L -Shaped Grid	117
7.2.2	Further Reducing the Number of Partial Waves	118
	Bibliography	123
A	Symmetries in Joint Angular Distribution	136
B	First Derivative of the Gaussian-Lobatto Basis in the Finite-Element Discrete Variable Representation Method	138
B.1	Preliminary	138
B.2	Case (i)	139
B.3	Case (ii)	140
B.4	Conclusion	142
C	Numerical Convergence Test	143
C.1	Convergence with Respect to l_1 and l_2	143
C.2	Convergence with Respect to the Numerical Grid Size	145
C.3	Comparison of the “Poisson Equation” and “Direct Integration” Methods	146
C.4	Convergence in the Number of Included Total Angular Momenta L	147
C.5	Convergence in the Propagation Time	149

D	Copyright Clearance	152
D.1	Copyright Clearance for Fig. 4.3, 4.12, 4.13 and Fig. 4.14	152
D.2	Copyright Clearance for Fig. 4.6	154
D.3	Copyright Clearance for Fig. 4.11	155
E	Sources and Data Files Descriptions	156
E.1	How to Use this Software	156
E.2	Source Codes and Files	157
E.3	Examples of Input Files	159
E.3.1	Example of “parameter.inp”	160
E.3.2	Example of “tdse.inp”	160

List of Figures

1.1	(a) Schematics for four different types of photoelectron emission patterns in the double ionization of helium. From top to bottom: back-to-back emission, side-by-side emission, conic emission, and symmetric emission. (b) Schematics for the identification of the corresponding emission patterns (with matching line types and colors) in joint angular distributions (see text).	7
2.1	Schematic of DVR-basis functions with 3 finite elements. 3 sets of DVR-basis functions are equally mapping over $[0,6]$ by 3 elements. The element index i ranges from 1 to 3 on the top, the numbers over each elements within colored circles are served as indices of DVR-basis functions as well as indices of DVR nodes, they are the second index of a DVR-basis function $f_{i,m}(r)$. The 4 circled numbers on the top-left label the DVR-basis functions in element 1. The 4 circled numbers on the top-middle label the DVR-basis functions in element 2, and the 4 circled numbers on the top-right label the DVR-basis functions in element 3. The curves represent the DVR-basis functions, the black dashed lines display the ordinary functions, the blue dashed lines are the bridge functions. The red dashed-dotted lines are two DVR-basis functions to be dropped due to the boundary conditions.	16
2.2	Example of a 1-D Hamiltonian matrix in the FE-DVR scheme with 3 finite elements and 4 DVR functions in each element. See Fig. 2.1 for detail.	20
2.3	Two typical joint angular distributions as contour plots. Panel (a) is for single-photon DI and panel (b) is for three-photon DI at unequal energy sharing.	33
3.1	Numerical grid point mapping over the radial interval $[0,137.5]$ for the first and last 10 elements for $N_{gr} = 4$. The black squares are grid points, and the red solid circles indicate the finite-element mapping.	40
4.1	Schematic energetics for non-sequential double ionization of helium by two 45 eV or one 90 eV photon and sequential double ionization by three 30 eV photons. I_{p1} and I_{p2} designate the first and second ionization threshold, respectively. For the examples considered in this section, the combined excess energy of the emitted electrons is $E_{exc} = 11$ eV.	43
4.2	Probability densities of the radial wave function for the (a) 1^1S ($1s^2 \ ^1S_0^e$) ground state and (b) 2^1S first excited state of helium obtained by imaginary time propagation on a logarithm color/gray scale. The blue solid triangle in (b) indicates the node in the r_1 coordinate of the first excited state with $L=0$.	46

4.3	JAD for $\hbar\omega = 42$ eV [(a), (b)] and $\hbar\omega = 85$ eV [(c), (d)]. In (a) and (c), only the ss , pp , and ds final-state angular momentum components are included, while all angular momentum components [with restriction (L_{\max} , l_1^{\max} , l_2^{\max}) = (2, 7, 7)] are included in (b) and (d). Graphs were taken from Ref. [119].	48
4.4	Absolute TDCS in $beV^{-1}sr^{-2}$ for a fixed angles ($\theta_1 = 0^\circ$) and different energy sharing. (a) Equal energy sharing $E_1 = E_2 = 10$ eV at $\theta_1 = 0^\circ$, (b) unequal energy sharing $E_1 = 3$ eV at $\theta_1 = 0^\circ$, $\varepsilon = 0.15$. The black dots with error bar are experimental results from [6]. The red dashed lines are our calculated results. The XUV photon energy is 99 eV.	51
4.5	Demonstration of (a) symmetric and (b) anti-symmetric joint angular distributions: the angular factor.	54
4.6	Symmetric and anti-symmetric amplitudes (figures were adapted from Ref. [39], except for the top-right panel).	56
4.7	Symmetric (a) and anti-symmetric (b) joint angular distributions, in which the angular factors were multiplied by the amplitudes.	57
4.8	(a) Calculated normalized joint angular distribution for the double ionization of helium by one $\hbar\omega_{XUV} = 90$ eV XUV photon at equal energy sharing. The XUV pulse has a peak intensity of 10^{14} W/cm ² and a pulse lengths of 1 fs. (b) Conditional angular distribution for $\theta_1 = 60^\circ$. The red dashed line shows the calculated angular distribution for $\hbar\omega_{XUV} = 90$ eV and is scaled by the factor 0.55 relative to the distribution calculated for $\hbar\omega_{XUV} = 99$ eV (green dash-dotted line). The black dots with error bars show the distribution measured by Bräuning <i>et al.</i> [6] for $\hbar\omega_{XUV} = 99$ eV in units of b eV ⁻¹ sr ⁻² . Adapted from [6]. (c) Conditional angular distribution for $\theta_1 = -76^\circ$ and $\hbar\omega_{XUV} = 99$ eV. The green dashed-dotted line shows our result, while the solid black lines are the convergent close-coupling calculations for different gauges by Kheifets and Bray [38], and the black dotted line shows a calculation with screened final-state Coulomb wave functions by Pont and Shakeshaft [84]. The black dots with error bars show the measured relative cross sections of Schwarzkopf <i>et al.</i> [93]. Adapted from Ref. [38].	58
4.9	TDCSs in units of $beV^{-1}sr^{-2}$ for the double ionization of helium and fixed detection angles (a,b) $\theta_1 = 0^\circ$, (c) 60° , and (d) 30° , indicated by the black arrows. The central XUV-photon energy is 99 eV. The black dots with error bars are absolute experimental TDCSs from Ref. [6]. Our calculated results are shown as red dashed lines and normalized to the experimental data at (a) $\theta_2 = 110^\circ$, (b) 95° , (c) 295° , and (d) 275° . Panels (a,c): Equal energy sharing with $E_1 = E_2 = 10$ eV ($\varepsilon = 0.5$). (b,d) Unequal energy sharing with $E_1 = 3$ eV ($\varepsilon = 0.15$). The green dotted lines show theoretical results of (a) Huetz <i>et al.</i> [6, 29] Panels (b-d): Kheifets and Bray [6]. Panels (c,d): The solid blue lines show TDCC results of Palacios <i>et al.</i> [70].	60

4.10	Calculated normalized joint angular distribution for the double ionization of helium by one $\hbar\omega_{\text{XUV}} = 90$ eV XUV photon at (a) equal energy sharing $\varepsilon = 0.5$, (b) unequal energy sharing $\varepsilon = 0.1$ and (c) extremely unequal energy sharing $\varepsilon = 0.01$. Panel (d): Angular difference distributions extracted from (a-c). The XUV pulse has a peak intensity of 10^{14} W/cm ² and pulse length of 1 fs.	62
4.11	Momentum (left column) and energy (right column) distributions of the two escaping electrons. The laser pulse has a sine-squared envelope around the peak intensity of 5×10^{14} W/cm ² and a time duration of ten optical cycles. The central XUV photon energies are 42, 48, 54, and 57 eV, respectively. These graphs were adapted from our reference [27].	64
4.12	Calculated normalized angular distribution for the double ionization of helium by two $\hbar\omega_{\text{XUV}} = 42$ eV XUV photon for four different electron-energy sharing values: (a) $\varepsilon = 0.5$, (b) $\varepsilon = 0.3$, (c) $\varepsilon = 0.1$, and (d) $\varepsilon = 0.01$. These graphs were adapted from our reference [119].	66
4.13	Calculated normalized angular distribution for the double ionization of helium by two $\hbar\omega_{\text{XUV}} = 70$ eV XUV photon for four different electron-energy sharing values: (a) $\varepsilon = 0.5$, (b) $\varepsilon = 0.3$, (c) $\varepsilon = 0.1$, and (d) $\varepsilon = 0.01$. These graphs were adapted from our reference [119].	67
4.14	Calculated normalized angular distribution for TPD1 of helium by two $\hbar\omega_{\text{XUV}} = 45$ eV (a,d), 54 eV (b,e) and 70 eV (c,f) XUV photon, respectively. The energy sharing for the top panel is equal ($\varepsilon = 0.5$), for the bottom panel it is extremely unequal ($\varepsilon = 0.01$). The XUV pulse has a peak intensity of 10^{14} W/cm ² and pulse length of 1 fs. These graphs were adapted from our reference [119].	68
4.15	Calculated normalized joint angular distributions for the double ionization of helium by two $\hbar\omega_{\text{XUV}} = 30$ eV XUV photons with different FE-DVR parameters. (a) Used the Grid 3 defined in Sec. 4.3, the sizes of the FEs are non-uniform. (b) 64 FEs with 11 DVR functions in each FE. The FEs are 4 a.u. long [76].	71
4.16	Normalized joint photoelectron energy distributions for the double ionization of helium by (a) one 90 eV, (b) two 45 eV, and (c) three 30 eV photons of a 10^{14} W/cm ² peak intensity 1-fs long XUV pulse. (d) Corresponding normalized double-ionization yields, integrated over the XUV-pulse spectral profile, as a function of the energy sharing ε between the photoelectrons. . .	75
4.17	Calculated normalized joint angular distributions for the double ionization of helium at equal energy sharing by (a) single-photon DI by 90 eV XUV pulse, (b) two-photon DI by one 45 eV XUV pulse and (c) three-photon DI by 30 eV XUV pulse.	76

4.18	Calculated normalized joint angular distributions for the double ionization of helium at equal energy sharing by (a) two 45 eV photons and (b) three 30 eV photons in XUV pulses with a peak intensity of 10^{14} W/cm^2 and a pulse length of 1 fs. Panels (c) and (d): DI cross sections for individual total angular momentum (black solid and red dashed lines) that contribute to DI for two-photon DI (c) and three-photon DI (d) at fixed angle $\theta_1 = 0^\circ$. Cross sections (blue dotted lines) including (c): $L = 0$ and 2 and (d): $L = 1$ and 3.	78
4.19	Calculated normalized joint angular distribution for the double ionization of helium by two $\hbar\omega_{\text{XUV}} = 45$ eV XUV photons at (a) equal energy sharing $\varepsilon = 0.5$, (b) unequal energy sharing $\varepsilon = 0.1$, and (c) extremely unequal energy sharing $\varepsilon = 0.01$. (d) Mutual angular difference distributions extracted from (a-c). The XUV pulse has a peak intensity of 10^{14} W/cm^2 and a pulse length of 1 fs. JADs for two-photon DI at different energy sharing. For two-photon DI, the JAD is not sensitive to the energy sharing change. From equal energy sharing $\varepsilon = 0.5$ to extremely unequal energy sharing $\varepsilon = 0.01$, the JAD is almost independent to the energy sharing ε .	79
5.1	Calculated normalized (a,c) joint and (b,d) mutual angular distributions for two-photon double ionization of helium for energy sharing parameters $\varepsilon = 0.01, 0.1, \text{ and } 0.5$. The XUV photon energy is (a,b) 50 eV and (c,d) 70 eV. All other XUV pulse parameters are the same as in Fig. 4.8.	87
5.2	Conditional angular distributions with one electron emitted along the XUV linear polarization direction ($\theta_1 = 0^\circ$) for two-photon double ionization of helium in XUV pulses with a central photon energy of 50 eV and pulse lengths of (a) 160 as, (b) 500 as, and (c) 3 fs. Each panel shows results for equal ($\varepsilon = 0.5$) and extremely unequal ($\varepsilon = 0.01$) energy sharing. The full-range distributions (left panels) are normalized to their maxima. The right panels zoom in on the forward emission contributions.	90
5.3	Forward-backward-emission asymmetries $A(\theta_1 = 0; \varepsilon)$ for the conditional angular distributions in Fig. 5.2 and for $\varepsilon = 0.1$ and 0.3. The inset shows asymmetries for XUV pulses with a central photon energy of 70 eV and 1 fs pulse length, corresponding to the angular distributions in Figs. 5.1 (c,d). Markers represent ab initio calculations and are straight-line interpolated.	91
5.4	Effective sequential-double-ionization yield versus the total pulse duration. The yield is calculated by the heuristic formula Eqn. (5.3). The inset shows the spectrum of an $\hbar\omega_{\text{XUV}} = 50$ eV pulse with sine-squared temporal profile and a pulse length of 1 fs. The blue area indicates the overlap of the pulse spectrum and the spectral domain for sequential double ionization at $\hbar\omega > 54.4$ eV.	93

- 5.5 Comparison of *ab-initio* calculated forward-backward double-ionization asymmetries $A(\theta_1 = 0; \varepsilon = 0.01)$ (stars) with the heuristic formula [Eqn. (5.3)] for the sequential-double ionization contribution Y_{seq}^{heur} (solid blue line) as a function of the XUV-pulse length for a central pulse energy of 50 eV. The sequential double ionization yield is normalized to the maximum of A at 650 as. The inset displays the spectrum of an $\hbar\omega_{XUV} = 50$ eV pulse with sine-squared temporal profile and a pulse length of 1 fs. The blue area indicates the overlap of the pulse spectrum and the spectral domain for sequential double ionization at $\hbar\omega > 54.4$ eV. 94
- 6.1 Normalized joint photoelectron energy distributions for IR-laser-assisted single-photon double ionization of helium at equal energy sharing in a 10-cycle XUV pulse of peak intensity 10^{14} W/cm², central photon energy $\hbar\omega_{XUV} = 89$ eV, and pulse length 0.46 fs. The assisting single-cycle laser pulse has a peak intensity of 3×10^{12} W/cm², photon energy of $\hbar\omega_{IR} = 1.61$ eV, and a pulse length of 2.6 fs. (a) Even effective numbers of IR photons. (b) Odd effective numbers of IR photons. 98
- 6.2 Normalized joint angular distributions for IR-laser-assisted double ionization of helium at equal energy sharing in a 10-cycle XUV pulse of peak intensity 10^{14} W/cm² and central photon energies of $\hbar\omega_{XUV} = 89$ eV and 45 eV. The assisting IR pulse has a peak intensity of 3×10^{12} W/cm², central photon energy $\hbar\omega_{IR} = 1.61$ eV, and pulse lengths (a,c) 2.6 fs and (b,d) 10.3 fs. (a-d) Laser-assisted single-89 eV-photon double ionization for (a,b) odd and (c,d) even total effective numbers of XUV and IR photons. (e) Normalized single-89 eV-photon double ionization for symmetric emission with and without assisting IR-laser pulses of pulse lengths 2.6 fs and 10.3 fs for odd total effective numbers of XUV and IR photons. (f) Normalized single-89 eV-photon double ionization for symmetric emission with an assisting 2.6 fs or 10.3 fs IR-laser pulse for even total effective numbers of XUV and IR photons, compared with IR-laser-free two-45 eV-photon double ionization. Calculation with angular momentum limits $(L_{max}, l_1^{max}, l_2^{max}) = (4, 4, 4)$ in Eqn. (2.40). 100
- 6.3 Normalized joint angular distributions for IR-laser-assisted single-XUV-photon double ionization of helium in a 10-cycle XUV pulse of peak intensity 10^{14} W/cm² and central photon energy (a-f) $\hbar\omega_{XUV} = 90$ eV. The assisting IR laser pulse has a pulse length of 2.6 fs. All other parameters are the same as for Fig. 6.2. (a-c,g) Odd and (d-f,h) even total effective numbers of photons. The effective number of absorbed IR photons is (a) $N_{IR} = -2$, (b) 0, (c) 2, (d) -1, (e) 1, and (f) 3. Negative photon numbers indicate that more IR photons are emitted than absorbed. (g,h) Normalized yields for symmetric laser-assisted XUV double-ionization. (g) Odd total numbers of photons with $N_{IR} = -2, 0$, and 2. (g) Even total numbers of photons with $N_{IR} = -1, 1$, and 3. 103

6.4	Calculated normalized joint angular distributions for IR laser-assisted single-XUV-photon double ionization of helium by $10^{14}W/cm^2$ peak intensity $\hbar\omega_{XUV} = 89$ eV XUV pulses assisted by coincident $3 \times 10^{12} W/cm^2$ IR-laser pulses. Contribution to the double-ionization yield from (a)-(c) odd and (d)-(f) even total effective numbers of XUV plus IR photons. Results for (a,d) equal energy sharing ($\varepsilon = 0.5$), (b,e) unequal energy sharing ($\varepsilon = 0.1$), and (c,f) extremely unequal energy sharing ($\varepsilon = 0.01$).	106
6.5	Mutual angular distributions for IR-laser-assisted single-XUV-photon double ionization of helium for differnt energy sharings ε . (a) Contributions to the double-ionization yield from (a) odd and (b) even total effective numbers of XUV plus IR photons. The XUV and IR pulse parameters are the same as in Fig. 6.4. The insets zoom into the distributions near the mutual angles $\theta_{12} = 0^\circ$ and 180°	108
6.6	Schematics of laser controlled DI. (a) Shift to side by side emission; (b) shift to back-to-back emission, and (c) enabling the side-by-side emission. The green solid lines stand for the momentum without laser assistance. The red dashed lines stand for the extra momentum obtained from the laser field. The momenta are plotted in blue dotted dashed lines.	109
6.7	Contributions to the mutual angular distributions for IR-laser-assisted single-XUV-photon double ionization of helium for (a) equal energy sharing and (b) extremely unequal energy sharing with $\varepsilon = 0.01$. XUV- and IR-pulse parameters are the same as in Fig. 6.4. The black solid curves correspond to XUV-pulse-only results, blue dotted lines to odd parity, and green dash-dotted lines display even parity. The red dashed curves show coherent additions of odd and even parity contributions.	111
6.8	Intensity dependence of JEDs. Panel (a) is laser-free result for comparison. (a-d) are JEDs with odd parity, and (e-g) are JEDs with even parity, respectively.	113
7.1	L -shaped grid. Panel (a): 2×2 blocks. Panel (b): 4×4 blocks. The red blocks form the L -shaped grid, the blue blocks are truncated, because the two electron radial probability densities in these regions are negligible for single ionization process.	118
7.2	Histogram of the probability-density distribution of partial waves in 42 eV XUV photon TPDI. The x-axis lists partial waves configurations (L, l_1, l_2) and corresponding index numbers for each partial wave. Different L values are plotted in different color: $L=0$ in black, $L=1$ in red, $L=2$ in blue and $L=3$ in purple. The $(0, 0, 0)$ partial wave corresponds to the $ ss\rangle$ state, it approximates 1. XUV pulse parameters: $5 \times 10^{14} W/cm^2$, and 1-fs pulse duration.	120

7.3	The probability densities of 4 partial waves with $L = 0$ in TPDI by single 1-fs duration XUV pulse with 42 eV central energy. The color scales are different in each panel. The (0, 0, 0) partial wave is the most important component, it indicates that most electrons stay in ground state. With increasing l_1/l_2 , the probability densities decrease. These graphs agree with the results shown in Fig. 7.2.	121
C.1	Normalized joint angular distributions for IR-laser-assisted XUV double ionization of helium at equal energy sharing for maximal angular momentum quantum numbers (a, e) $(L, l_1, l_2)_{\max} \equiv (L_{\max}, l_1^{\max}, l_2^{\max}) = (3, 3, 3)$, (b, f) (4, 4, 4), (c, g) (5, 5, 5), and (d, h) (6, 6, 6). (a-d) Results for odd and (e-h) even photon numbers. The photon numbers correspond to one absorbed XUV plus the number of absorbed minus emitted IR photons.	148
C.2	Normalized joint angular distributions for IR-laser-assisted XUV-double ionization of helium at equal energy sharing for the different propagation times τ_{\max} past the end of the IR pulse. (a) $\tau_{\max} = 4$ a.u.; (b) $\tau_{\max} = 24$ a.u.; (c) $\tau_{\max} = 104$ a.u.. (d) Normalized double-ionization yields at $\theta_1 + \theta_2 = 360^\circ$. As the propagation time is increased, the side-by-side-emission yield at $\theta_1 = \theta_2 = 180^\circ$ disappears as physically expected.	149
E.1	A sample code of the file <code>helium_fedvr.f90</code> . The developing history of code is shown in comment lines.	159

List of Tables

2.1	The specified nodes of Gaussian-Lobatto quadrature rule for the 4-th order DVR basis. The x_i and ω_i are the coordinate and corresponding weight of the i -th Lobatto node point, respectively.	14
2.2	The specified nodes of Gaussian-Lobatto quadrature rule for the 10-th order DVR basis. The x_i and ω_i are the coordinate and corresponding weight of the i -th Lobatto node point, respectively.	14
3.1	Atomic parameters of Tong-Lin SAE potential model adapted from Ref. [106].	35
3.2	Energy levels of hydrogen atoms. Lobatto node number $N_{gr} = 4$. Up to $n=7$, the error between current value and accurate value is less than 1%.	35
3.3	Energy levels of the hydrogen atoms. Lobatto node number $N_{gr} = 10$. Up to $n=5$, our current FE-DVR eigenvalues and the accurate values are exactly the same, and up to $n=7$, the error between present value and accurate value is less than 1%.	36
3.4	The grid points in the first and last 10 elements, and each finite element is mapped by 4 Gaussian-Lobatto nodes.	37
3.5	The grids in the first and last 5 elements, and each finite element is mapped by 10 Gaussian-Lobatto nodes.	38
3.6	First 10 bound-state energy levels. The present results are calculated for singlet states by diagonalization of Hamiltonian matrix with 60 finite elements and 10 DVR nodes in each finite element mapping over radial coordinate. The experimental data were retrieved from NIST Atomic Spectra Database [67] on March 29, 2015.	39
4.1	Selection of partial waves for the helium singlet states under the constraint $(L_{\max}, l_1^{\max}, l_2^{\max}) = (2, 3, 3)$	49
C.1	The energies of the 1^1S ground state and the two lowest $L=0$ excited states (2^1S and 3^1S) of helium. The correlation matrix elements $r_{<}^l/r_{>}^{l+1}$ (cf. Appendix A) are computed by either Gaussian-Lobatto integration (“Direct-integration method”) or by solving Poisson’s equation (“Poisson’s Eqn.”). The FE-DVR imaginary time propagation calculations were performed for two different radial numerical grids covering $0 \leq r_1 \leq r_1^{\max} = 60$ a.u. and $0 \leq r_2 \leq r_2^{\max} = 60$ a.u.: “Grid 1” uses 50 elements with 4 grid points in each element, and “Grid 2” uses 20 elements with 10 grid points in each element. The last three rows show theoretical [97, 119] and experimental [53] energies from literature. All the energies are given in a.u.	144

E.1	This table lists and describes makefile, main program and subroutines. . . .	157
E.2	This table lists and describes the files for data analysis. The .x files are executable files obtained from compiling the source files in the same row. . .	158
E.3	This table lists and describes the input files.	158
E.4	This table lists and describes the output files.	158

Acknowledgments

First and foremost, I would like to express my sincerest gratitude to my advisor Prof. Uwe Thumm for the continuous support of my Ph.D study and research, for his patience, motivation, enthusiasm, and immense knowledge. His guidance helped me all the time, during my research and writing this thesis. I could not have imagined having a better advisor and mentor for my Ph.D study.

Besides my advisor, I would like to thank the rest of my thesis committee: Prof. Brett Esry, Prof. Carlos Trallero, Prof. Todd Cochrane, Prof. X. Jack Xin, and Prof. Liang-Wu Cai, for their encouragement, insightful comments, and critical and hard questions.

My sincere thanks must go to Dr. Xiaoxu Guan, for the helpful discussions on the FE-DVR derivations and implementations, paper and thesis writing along with proofreading.

My sincere thanks also goes to Dr. Yujun Wang and Dr. Wei Cao, for their helps in code-debugging, resolving physical problems, and paper writing.

I would like to thank the former group members, Dr. Chang-hua Zhang, Dr. Feng He, and Dr. Qing Liao and Dr. Maia Magrakvelidze. They helped me a lot in research, code-debugging, learning physical concepts, using numerical tools, and paper writing.

I thank my follow group members in James R. Macdonald (JRM) Laboratory theory group: Jianxiong Li (Jason Li), Alex Kramer. They helped me a lot in research, especially in proofreading of my journal papers and thesis.

Last but not the least, I would also like to thank my family for the support they provided me through my entire life. Especially, all the support they have provided me over the years was the greatest gift anyone has ever given me. In particular, I must acknowledge my wife, XIUPING GAO, and my kids, Phyllis and Alice, without whose love, encouragement and editing assistance, I would not have finished this thesis.

Preface

All of the work presented henceforth was conducted at the Department of Physics of the Kansas State University, Manhattan campus.

A version of Chapters 4, 6.1 and Appendix C has been published [A. Liu and U. Thumm. Laser-assisted XUV few-photon double ionization of helium: joint angular distributions. *Phys. Rev. A* **89**, 063423 (2014)]. I was the lead investigator, responsible for all major areas of concept formation, data collection and analysis, as well as manuscript composition. Dr. Uwe Thumm was the supervisory author on this project and was involved throughout the project in concept formation and manuscript composition.

A version of Chapters 4 and 6.2 has been published [A. Liu and U. Thumm. Laser-assisted XUV double ionization of helium: Energy-sharing dependence of joint angular distributions. *Phys. Rev. A* **91**, 043416 (2015)]. I was the lead investigator, responsible for all major areas of concept formation, data collection and analysis, as well as manuscript composition. Dr. Uwe Thumm was the supervisory author on this project and was involved throughout the project in concept formation and manuscript composition.

A version of Chapter 5 has been submitted to the Physical Review Letter [Aihua Liu and Uwe Thumm, A criterion for distinguishing sequential from non-sequential contributions to the double ionization of helium in ultrashort XUV pulses, submitted to *Phys. Rev. Lett.*]. I was the lead investigator, responsible for all major areas of concept formation, data collection and analysis, as well as the majority of manuscript composition. I was responsible for all major areas of concept formation, data collection and analysis, as well as the majority of manuscript composition. Dr. Uwe Thumm was the supervisory author on this project and was involved throughout the project in concept formation and manuscript composition.

Some figures in this thesis were taken or adapted from literatures, the copyright clearances for reusing these figures were obtained through Copyright Clearance Center (www.copyright.com) and are included in Appendix D.

Abbreviations

A list of the abbreviations used in this thesis is given below.

a.u.	–	atomic unit
as	–	<u>att</u> osecond
fs	–	<u>fem</u> tosecond
DC	–	<u>D</u> irect <u>C</u> urrent
FWHM	–	<u>F</u> ull- <u>W</u> idth at <u>H</u> alf- <u>M</u> aximum
DVR	–	<u>D</u> iscrete- <u>V</u> ariable <u>R</u> epresentation
FE-DVR	–	<u>F</u> inite- <u>E</u> lement <u>D</u> V <u>R</u>
TDSE	–	<u>T</u> ime- <u>D</u> ependent <u>S</u> chrödinger <u>E</u> quation
TISE	–	<u>T</u> ime- <u>I</u> ndependent <u>S</u> chrödinger <u>E</u> quation
JED	–	<u>J</u> oint <u>E</u> nergy <u>D</u> istribution
JAD	–	<u>J</u> oint <u>A</u> ngular <u>D</u> istribution
MAD	–	<u>M</u> utual <u>A</u> ngular <u>D</u> istribution
DI	–	<u>D</u> ouble <u>I</u> onization
SDI	–	<u>S</u> equential <u>D</u> ouble <u>I</u> onization
NSDI	–	<u>N</u> on- <u>S</u> equential <u>D</u> ouble <u>I</u> onization
SPDI	–	<u>S</u> ingle- <u>P</u> hoton <u>D</u> ouble <u>I</u> onization
TPDI	–	<u>T</u> wo- <u>P</u> hoton <u>D</u> ouble <u>I</u> onization
3PDI	–	<u>3</u> - <u>P</u> hoton <u>D</u> ouble <u>I</u> onization
UV	–	<u>U</u> ltraviolet
XUV	–	<u>E</u> xtremely <u>U</u> ltraviolet
IR	–	<u>I</u> nfrared
CCC	–	<u>C</u> onvergent <u>C</u> lose <u>C</u> oupling
TDCC	–	<u>T</u> ime- <u>D</u> ependent <u>C</u> lose <u>C</u> oupling
SAE	–	<u>S</u> ingle- <u>A</u> ctive <u>E</u> lectron
TAE	–	<u>T</u> wo- <u>A</u> ctive <u>E</u> lectron
CPU	–	<u>C</u> entral- <u>P</u> rocessing <u>U</u> nit
GPU	–	<u>G</u> raphics- <u>P</u> rocessing <u>U</u> nit

Chapter 1

Introduction

The investigation of the interaction of atoms and molecules with intense laser fields is one of the most interesting areas of the current research in atomic and molecular physics. The general motivation for studying molecules in laser fields lies in the possibility of gaining fundamental understanding of the dynamics and the intermediate processes involved in various physical, chemical, and biological reactions.

1.1 History of the Atom

1.1.1 Atomic Models

Natural philosophy, or the philosophy of nature, was the philosophical study of nature and the physical universe that was dominant before the development of modern science. It is considered to be the precursor of natural sciences such as physics. A Chinese philosopher *Mozi* (ca. 470 BC - ca. 391 BC) believed there are indivisible small units for every material. At the same time, the ancient Greek philosophers *Democritus* (ca. 460 BC - ca. 370 BC) also believed that every material is made from small units, he called these small units as “*ατομος*” (atomos), which means “*uncuttable, or indivisible, something that cannot be divided further*” in Greek. However, the scientific concept of the atom was first used by Robert Boyle in his book *The Sceptical Chymist* published in 1661 [74]. In this book, he claimed that matter is made from different “particles” or atoms.

During 1802-1803, John Dalton developed the basis of modern atomic and molecular theory [74]. The main points of Dalton's atomic theory include: (1) Elements are made of extremely small particles called atoms. (2) Atoms of a given element are identical in size, mass, and other properties; atoms of different elements differ in size, mass, and other properties. (3) Atoms cannot be subdivided, created, or destroyed. (4) Atoms of different elements combine in simple whole-number ratios to form chemical compounds. (5) In chemical reactions, atoms are combined, separated, or rearranged.

Dalton's atomic theory describes a structureless particle. However, in 1897, J. J. Thomson and coworkers discovered the first subatomic particle - the electron [74]. In the 1910's, experiments by Ernest Rutherford and coworkers established the structure of an atom as a dense nucleus of positive charge surrounded by lower-mass electrons [74]. The proton was identified as the nucleus of the hydrogen atom [112], and the neutron was introduced to explain isotopes, whose nuclei have different masses in spite of identical atomic numbers. In 1932, the neutron was discovered by J. Chadwick [68].

Modern atomic theory developed alongside quantum mechanics. N. Bohr used a shell model to successfully explain the energy levels in hydrogen [114]. In the 1920's, E. Schrödinger and W. Heisenberg and others developed modern quantum mechanics [51, 112, 114]. Nowadays, the probabilistic Copenhagen interpretation of quantum mechanics is widely accepted in atomic and molecular physics [112, 114].

1.1.2 History of the Helium Atom

Although helium is found on the Earth, it was first discovered in the solar corona on the Sun [99, 112], and named after the Greek word Helios, the Sun [99]. The first evidence of helium was observed in 1868 as a bright yellow line with a wavelength of 587.49 nm in the spectrum of the chromosphere of the Sun. In 1882, Italian physicist Luigi Palmieri detected helium on the Earth, through its D3 spectral line, when he analyzed the lava of Mount Vesuvius [102]. In 1907, E. Rutherford and T. Royds demonstrated that alpha particles are

helium nuclei [74].

Helium is the second lightest element, and the second simplest atom to model, following the hydrogen atom. Unlike hydrogen, which mostly exists in nature in the molecular form of H_2 , helium exists in the form of isolated atoms. The helium atoms are therefore the best and simplest object for investigating correlation in a many-electron system. Although it is rare on Earth, helium is the second most abundant element in the known Universe (after hydrogen), constituting 23% of the Universe’s baryonic mass [15].

1.2 History of the Laser and other Light Sources

In 1917, Albert Einstein established the theoretical foundations for the laser and the maser in the paper *Zur Quantentheorie der Strahlung (On the Quantum Theory of Radiation) via a re-derivation of Max Planck’s law of radiation* [99], conceptually based upon probability coefficients (Einstein coefficients) for the absorption, spontaneous emission, and stimulated emission of electromagnetic radiation. In 1928, Rudolf W. Ladenburg confirmed the existences of the phenomena of stimulated emission and negative absorption [99]. In 1939, V. A. Fabrikant predicted the use of stimulated emission to amplify “short” waves [99]. In 1947, Willis E. Lamb and R. C. Retherford found apparent stimulated emission in hydrogen spectra and effected the first demonstration of stimulated emission [99]. In 1950, Alfred Kastler proposed the method of optical pumping [99], experimentally realized, two years latter, by Brossel, Kastler, and Winter [68, 99].

In 1959, the term “LASER” was first used in the paper *The LASER, Light Amplification by Stimulated Emission of Radiation* [24, 99]. After the invention of the laser, it has been applied to many areas of modern society, including science, consumer electronics (such as the PC, and smartphones), information technology, medicine, industry, law enforcement, entertainment, and the military. In the 1980’s, the discovery of high-order harmonic generation by intense laser-atom interactions started to provides a new method to generate coherent, ultrashort-pulse, x-ray emission [9]. The term “Free-electron laser (FEL)” was

first coined by John Madey in 1976 at Stanford University [61]. The mechanism of the FEL is quite different from the traditional laser; there is no “stimulated emission”; it has the widest frequency range of any laser type, and can be widely tunable [13], from microwaves, through terahertz and infrared radiations, to the visible spectrum, ultraviolet, and X-ray regimes [64].

With the emergence of attosecond ($1 \text{ as}=10^{-18} \text{ s}$) optics in the twenty-first century, available attosecond pulses open the possibility of probing electron dynamics in matter [9], and therefore electron correlation, on its own timescale. The simplest electron-electron correlation system is the helium atom. Using attosecond pulses, it is possible to not only observe, but also actively induce and control correlation effects [19]. The helium atom double ionization (DI) is the best candidate for such investigation.

1.3 Double Photo-Ionization

1.3.1 History

Atomic double photoionization (DPI) is a process of formation of doubly-charged ions when laser radiation is exerted on atoms [87, 110]. DI is usually less probable than single ionization (SI). Two different processes are distinguished in the DI of helium: sequential DI (SDI) and non-sequential DI (NSDI). SDI is a process of formation of doubly-charged ions consisting of two separate single-electron ionization events: the first electron is removed from an atom followed by detachment of the second electron from the ion. NSDI is a process whose mechanism differs from the sequential one. For example, both the electrons leave the nuclei simultaneously and the second electron’s liberation is assisted by the first electron.

The phenomenon of NSDI was experimentally discovered by Suran and Zapesochny for alkaline earth atoms in 1975 [103]. Despite extensive studies, the details of double ionization in alkaline earth atoms remain unknown. For noble gas atoms, NSDI was first observed by L’Huillier [42, 43]. The interest in the phenomenon grew rapidly after it was rediscovered [110] in higher intensity infrared fields.

At the same time, the DI of helium in intense extremely ultraviolet (XUV) pulses has also been a subject for both theorists and experimentalists. In the 1990's, Huetz *et al.* applied the Wannier theory for the Coulomb break-up of three-particle system [17, 109] to the DPI of helium and predicted the angular correlation between two escaping photoelectrons [29]. Then, Briggs and coworkers [54–57] derived selection rules for helium DI. Many experiments on single-photon DI (SPDI) of helium with XUV pulses were done in the 1990's [6, 93–96, 104, 105]. The first experimental result for the triple differential cross section (TDCS) of NSDI of helium was reported by Schwarzkopf *et al.* [93] who discussed only equal energy sharing of the photoelectrons. Later, experimental results for unequal energy sharing were reported [95, 96]. Bräuning *et al.* later reported measurements that cover the full ranges of energy sharing and emission angles of the two photoelectrons [6]. In the meantime, many theoretical studies have been done [6, 32, 38, 40, 58, 70–73, 77, 80–83, 88].

Due to their extremely small values, the measurement of a two-photon DI (TPDI) cross section has remained a challenge to experimentalists in the laboratory. To the best of our knowledge, the first measured two-photon DI cross sections of helium were published in 2005 by Hasegawa *et al.* [30]. In this experiment, intense higher harmonics in the soft X-ray spectral domain were used, and the two-photon DI cross section for XUV pulses with a photon energy of 42 eV were estimated as $4 \cdot 10^{-53} \text{ cm}^4\text{s}$.

Following the 2005 experiment of Hasegawa *et al.* [30], two-photon DI of helium has been the subject of many theoretical studies [4, 21, 27, 32, 37, 40, 70–73, 77, 79, 98, 100, 101, 119]. In particular, Guan *et al.* [26, 27] presented the joint energy distribution of two photoelectrons in both sequential and non-sequential regimes, and discussed the TDCSs of 42 eV XUV TPDI; Zhang *et al.* [119] calculated joint angular distributions (JADs) for two-photon DI by XUV pulses in both the non-sequential ($39.5 \text{ eV} < \hbar\omega_{\text{XUV}} < 54.4 \text{ eV}$) and the sequential regimes ($\hbar\omega_{\text{XUV}} > 54.4 \text{ eV}$) for different energy sharing of the emitted electron. Kheifets and Ivanov have discussed the TPDI angular distribution by convergent close-coupling (CCC) theory [39, 40]. Guan *et al.* studied the dynamics of TPDI of helium in

short intense XUV pulses by an *ab initio* method based on a time-dependent close-coupling (TDCC) approach [27]. Palacios *et al.* [71–73] and Peng *et al.* [79] worked on investigations of two delayed XUV pulses; while Zhang *et al.* [119] focused on the joint angular distributions (JADs) of the emitted electrons with different excess energy and energy sharing for TPDI by XUV pulses in both the non-sequential ($39.5 \text{ eV} < \hbar\omega_{XUV} < 54.4 \text{ eV}$) and the sequential regimes ($\hbar\omega_{XUV} > 54.4 \text{ eV}$). Ni *et al.* [65] applied selection rules to few-XUV-photon DI by solving the TDSE for a simplified helium model and revealed the oscillation between the forbidden and non-forbidden of back-to-back electron emission due to the absorption of odd and even photon numbers in a monochrome XUV pulse. Jiang *et al.* have discussed the difference in SPDI and TPDI in the difference of emission angles of two photoelectrons [37]. None of these investigations address the influence of an IR laser. The role of an assisting IR-laser pulse was studied by Hu in 2013 as a step towards the coherent control of chemical reactions [34]. The author’s *ab initio* calculations for the DI of helium by an attosecond XUV pulse showed that the delay of the assisting few-cycle IR laser very sensitively influences the photoelectron energy distribution and can be tuned to significantly enhance the emission of fast photoelectrons.

1.3.2 Emission Patterns

Helium DI is a convoluted process where photon-electron, electron-nucleus, and electronic interactions compete. Accordingly, the detailed scrutiny of measured and calculated DI data and the most rewarding comparison of experimental and theoretical data requires highly differential emission probabilities (or cross sections) from which effects due to different emission pathways can be best distinguished. We therefore focus in this work on a specific value of the energy sharing between the two emitted electrons, equal energy sharing, and investigate highly differential JADs for equal energy sharing. JADs for the helium DI exhibit four different typical electron emission patterns (Fig. 1.1), which we will refer to repeatedly throughout this thesis. For coplanar emission, each pattern can be related to a given range

of the electron-emission angles θ_1 and θ_2 relative to the linear polarization direction of the XUV and/or IR electric field \mathbf{E} , which will serve as the quantization (z) axis in our calculations below. The red solid arrow in Fig. 1.1(a) indicates the XUV or IR electric field direction \mathbf{E} , the black solid arrows denote the z -axis, and the remaining arrows represent asymptotic photoelectron momenta. Different colors and line styles correspond to different emission patterns in the JADs, as schematically depicted in Fig. 1.1(b):

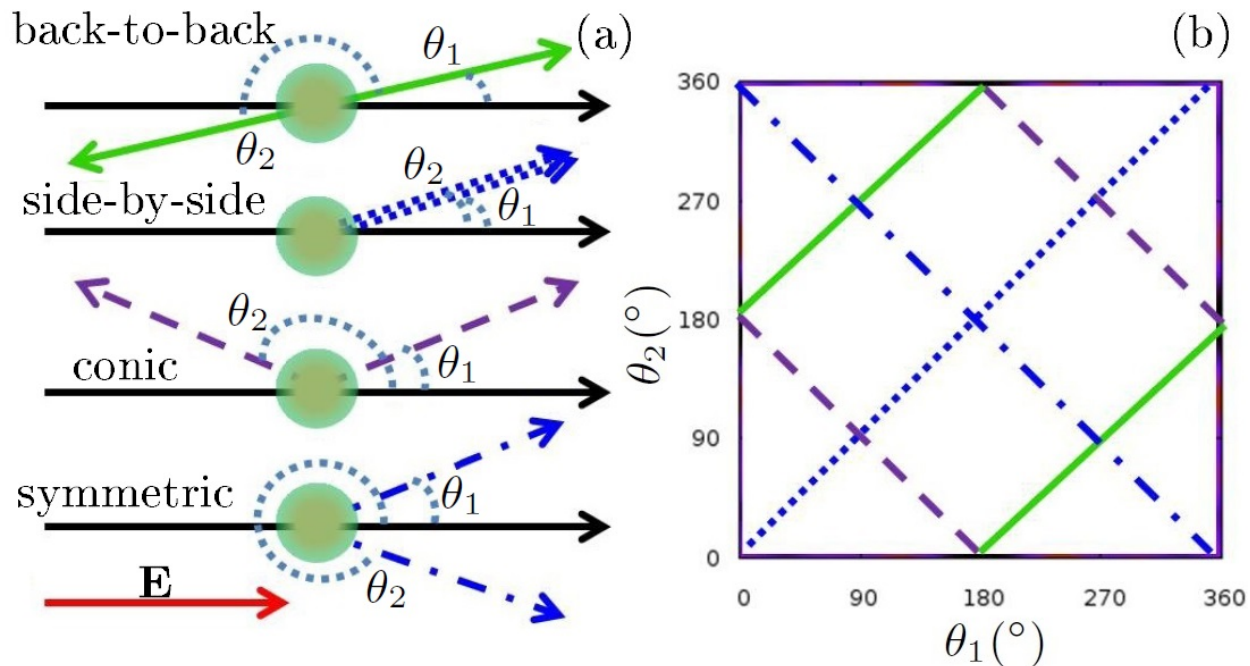


Figure 1.1: (a) Schematics for four different types of photoelectron emission patterns in the double ionization of helium. From top to bottom: back-to-back emission, side-by-side emission, conic emission, and symmetric emission. (b) Schematics for the identification of the corresponding emission patterns (with matching line types and colors) in joint angular distributions (see text).

- “back-to-back emission” (green solid arrows in Fig. 1.1(a) and green solid lines with slope 45° in Fig. 1.1(b) with $\theta_{12} = |\theta_1 - \theta_2| = 180^\circ$),
- “side-by-side emission” (blue dotted arrows in Fig. 1.1(a) and blue dotted lines in Fig. 1.1(b) with $\theta_1 = \theta_2$),

- “conic emission” (purple dashed arrows in Fig. 1.1(a) and purple dashed line with slope -45° and $\theta_1 + \theta_2 = 360^\circ \pm 180^\circ$), and
- “symmetrical emission” (blue dotted-dashed arrows in Fig. 1.1(a) and dotted-dashed line along $\theta_1 + \theta_2 = 360^\circ$ in Fig. 1.1(b)).

1.4 Contents of this Thesis

We have investigated few-photon DI of helium atoms without and in the presence of an assisting IR-laser field by numerically solving the TDSE in full dimensionality [46, 48]. We consider the absorption of one ($\hbar\omega_{XUV}=89 - 99$ eV) or two ($\hbar\omega_{XUV}=45$ eV) XUV photons and compare the XUV-pulse-induced DI of helium without and with the assistance of an IR pulse. We discuss numerical examples for which the electrons are emitted from the ground state of helium with excess energies between 10 and 20 eV and find that the presence of the IR field alters photoelectron angular distributions in a characteristic way due to the transfer of photon momenta from the assisting IR pulse.

In this thesis, the theoretical tools are presented first. In Chap. 2, we present the finite-element discrete-variable representation (FE-DVR) implementation, solve the TDSE with Arnodi-Lanczos method, and formulate the physical observables used in later discussions.

In Chap. 3, we apply the FE-DVR scheme to hydrogen atoms and to helium atoms with single-active-electron (SAE) model. Some numerical details, such as grid sizes (finite-element size and DVR order) and propagation time step Δt , will be discussed in this chapter.

In the following three chapters, the FE-DVR scheme is applied to the studies of helium photo-DI by a single XUV pulse (Chap. 4 and 5) and to single-XUV-photon DI within the presence of a laser field (Chap. 6). In Chap. 4, few-photon DI by XUV pulse is discussed. And we discuss and compare characteristics of few-photon DI. In Chap. 5, we study sequential and non-sequential contributions to the TPDI of helium exposed to the electric field of an ultrashort XUV pulse. The concepts of sequential and non-sequential DI are clarified in short and long pulses, respectively.

In Chap. 6, we applied an IR field to the single-XUV-photon DI. This study predicts the enabling of back-to-back emission at equal energy sharing, and the enhancement of side-by-side emission at unequal energy sharing [49].

The last Chapter, Chap. 7, summarizes the results presented in this dissertation, followed by six appendices containing a list of abbreviations used in the dissertation, a derivation of symmetries of JADs, a short derivation of Lobatto basis functions in the DVR theory, numerical convergence tests, source-code descriptions, and copyright clearances for reusing figures from literatures.

Atomic units (a.u.) are used throughout this thesis, unless specified otherwise.

Chapter 2

Theory and Numerical Implementation

In the chapter, the quantum mechanics theory of helium atoms will be presented first. Next we discuss the discretion scheme on numerical grids. At the end of this chapter, we discuss how to extract physical observables from wave functions we obtained by solving the TDSE.

2.1 The Time-Dependent Schrödinger Equation

The Schrödinger equation is the basic equation, just like Newton's second law in classical mechanics. It was introduced to quantum mechanics by Erwin Schrödinger in 1926 [112]. The solution of a Schrödinger equation is called as wave function. In the Copenhagen interpretation, the square of wave function is interpreted as a probability amplitude.

The Schrödinger equation has two forms: time-independent and time-dependent. The time-independent Schrödinger equation (TISE) is used to describe a time-independent system, such as the harmonic oscillator. To investigate the dynamics of a system, we need to use the TDSE, which gives a description of how a system evolves in time.

The form of the non-relativistic Schrödinger equation depends on the physical situation. In atomic units, it can generally be written as

$$i\frac{\partial\Psi}{\partial t} = \hat{H}\Psi, \quad (2.1)$$

where Ψ is the wave function of the the quantum system of interest, and \hat{H} is the Hamiltonian

operator which characterizes the total energy of any given wave function and takes different forms depending on the situation. In position space, the one-particle TDSE can be written as:

$$i\frac{\partial\Psi(\mathbf{r};t)}{\partial t} = \hat{H}\Psi(\mathbf{r};t), \quad (2.2)$$

and the two-particle TDSE is expressed as:

$$i\frac{\partial\Psi(\mathbf{r}_1, \mathbf{r}_2; t)}{\partial t} = \hat{H}\Psi(\mathbf{r}_1, \mathbf{r}_2; t). \quad (2.3)$$

Equation (2.1) can be formally solved as [51]:

$$\Psi(t) = \hat{\mathcal{T}} \exp\left(-i \int_{t_0}^t \hat{H}(t') dt'\right) \Psi(t_0), \quad (2.4)$$

where the time-ordering operator $\hat{\mathcal{T}}$ is introduced [51]. The time-ordering operator acts on a group of time-dependent operators, $\hat{\mathcal{T}}[\hat{H}(t_1)\hat{H}(t_2)\hat{H}(t_3)]$, and is just an instruction to arrange the operators with the earliest times to the right (the earlier time operator acts on wave function first). For example,

$$\hat{\mathcal{T}}[\hat{H}(t_1)\hat{H}(t_2)\hat{H}(t_3)] = \hat{H}(t_3)\hat{H}(t_1)\hat{H}(t_2), \quad \text{if } t_3 > t_1 > t_2. \quad (2.5)$$

If a potential is time-independent, i.e. $d\hat{V}(t)/dt = 0$, or the potential changes slowly, it can be treated as a time-independent operator in a short time step. Therefore, we have $\hat{V}(t) \approx \hat{V}(t_0 + \Delta t)$ for small $\Delta t = t - t_0$, and the time-ordering can be dropped. The time-dependent wave function can now be approximated as

$$\Psi(t) \approx \exp\left(-i \int_{t_0}^t \hat{H}(t') dt'\right) \Psi(t_0). \quad (2.6)$$

The wave function $\Psi(t)$ can be calculated by iteratively propagating by a small time step Δt until $t = N\Delta t$. For each time step,

$$\Psi(t + \Delta t) \approx \exp\{-i\hat{H}(t + \Delta t/2)\Delta t\}\Psi(t). \quad (2.7)$$

2.2 Finite-Element Discrete Variable Representation

In the previous section, we derived the formal solution of the TDSE. In the following sections, we want to numerically solve it. After trying different schemes, we finally selected the finite-element discrete-variable representation (FE-DVR) scheme for the implementation on a numerical grid. By adopting this scheme, we can have at least three advantages:

1. High accuracy. By using the Gaussian quadrature rule, we need fewer grid points than uniform grids to achieve the same accuracy.

2. Variable grids. By using finite elements, we can use more grids in the region near the nucleus, and less grid points in the outer region, without doing any transformation. This is very efficient for the Coulomb potential, especially for the low- n energy levels.

3. High efficiency and parallelizability. The FE-DVR method is efficient in distributed memory (a multiple-processor computer system in which each processor has its own private memory) parallel computing. Each computing node on most supercomputers is equipped with two processors. For example, Edison at NERSC has 24 cores per node [63]. The shared-memory-only computing is still very limited for large scale calculations due to the high demanded RAM memory requirement. Depending on the laser parameters, the sizes of the physical problems can increase dramatically, either through the number of angular partial waves, or the number of spatial grid points (or both). Therefore we have to parallelize our code through distributed-memory programming. To parallelize the problem, the numerical grid is divided into many small blocks, each block almost propagates independently, except for the exchanges of data on the boundary with neighboring blocks. For a regular scheme, such as finite difference, the ghost points (that are located outside interval of the local grid) are dependent on the order of finite difference. To get a better accuracy, five-point, or even nine-point stencil finite-difference schemes are often adopted. The wave functions at the ghost points are communicated via network, which is much slower than RAM reading. In the FE-DVR method, no matter what the order of the DVR basis is, we only have one ghost point, and the data exchange is therefore minimized.

2.2.1 Discrete Variable Representation

Before its application to atomic physics, the DVR scheme was widely used [44, 45, 78, 88]. Different from the traditional numerical scheme, a DVR scheme uses a set of the basis functions defined at grid points to describe a wave function.

Gaussian quadrature rule

The Gaussian quadrature rule states that an integral of a polynomial function can be expanded as a weighted sum of function values at specified grid points within the domain of integration. For convenience, taking the domain of integration in $[-1, 1]$, an n -point Gaussian-Legendre quadrature rule is expressed as

$$\int_{-1}^1 f(x)dx = \sum_{i=1}^n \omega_i f(x_i), \quad (2.8)$$

where x_i and ω_i are the coordinate and corresponding weight of the i -th specified point, respectively. We choose the zeros of a Legendre polynomial as our specified points, and denote them as quadrature nodes. Depending on whether including end points (-1 and 1) or not, there are three kinds of typical quadrature rules. The first kind is the Gaussian-Legendre rule, which does not include neither -1 nor 1 as the grid nodes of DVR basis. The second one is the Gaussian-Radau rule, which includes only one end (-1 or 1). The last one is the Gaussian-Lobatto rule, which includes both -1 and 1 as the grid nodes of DVR basis. Depending on the physical problem we engaged, we can choose one or two types of these grids (Legendre, Radau, Lobatto). In Tab. 2.1 and 2.2, we show examples of the grid points and weights for the Gaussian-Lobatto quadratures of 4-th and 10-th orders, respectively.

DVR Functions

Following the suggestion of Light *et al.* [44, 45], Rescigno *et al.* [58, 88] and Schneider *et al.* [90–92], we can construct polynomial functions on these quadrature nodes:

$$f_m(x) = \begin{cases} \prod_{j \neq m} \frac{x-x_j}{x_m-x_j}, & -1 \leq x \leq +1, \\ 0, & \text{else,} \end{cases} \quad (2.9)$$

Table 2.1: The specified nodes of Gaussian-Lobatto quadrature rule for the 4-th order DVR basis. The x_i and ω_i are the coordinate and corresponding weight of the i -th Lobatto node point, respectively.

x_i	ω_i
-1.0000000000000000	0.1666666666666667
-0.4472135954999579	0.8333333333333333
0.4472135954999579	0.8333333333333333
1.0000000000000000	0.1666666666666667

Table 2.2: The specified nodes of Gaussian-Lobatto quadrature rule for the 10-th order DVR basis. The x_i and ω_i are the coordinate and corresponding weight of the i -th Lobatto node point, respectively.

x_i	ω_i
-1.0000000000000000	0.0222222222222222
-0.9195339081664588	0.13330599085107
-0.7387738651055051	0.22488934206313
-0.4779249498104445	0.29204268367968
-0.1652789576663870	0.32753976118390
0.1652789576663870	0.32753976118390
0.4779249498104445	0.29204268367968
0.7387738651055051	0.22488934206313
0.9195339081664588	0.13330599085107
1.0000000000000000	0.0222222222222222

where m is the index of DVR basis and j is the index for the grid points. Both m and j run from 1 to n , the order of the DVR basis.

Properties of DVR functions

For DVR-basis functions, there is an important and useful relation between function and node

$$f_m(x_j) = \delta_{mj}, \quad (2.10)$$

where, x_j is the coordinate position of the j -th node. This relation means that only when the index of the node equals the index of the DVR-basis function, the function value equals 1; when they are different, the function value is zero. Here we need to notice that this relation is only valid for node points. When the coordinate position x is located between these DVR

nodes, the function value is neither 1 nor 0. Our numerical calculation is performed with these fixed DVR nodes.

2.2.2 Finite-Element Discrete-Variable Representation

In the previous subsection, we have discussed the DVR basis functions in the region $[-1,1]$. However, a physical problem typically spans an arbitrary region, for example, $[0,100]$. To apply the DVR theory, we can simply transform the physical space $[0,100]$ into the model space spanned over $[-1,1]$, or divide $[0,100]$ into many small elements, and transform all the finite elements in physical space into the model space spanned over $[-1,1]$. The first option is simple but not efficient, because it will generate a dense Hamiltonian matrix whose elements are mostly nonzero (in contrast to sparse matrix in which most of the elements are zero). It is difficult to save and slower to diagonalize a dense matrix than to solve a sparse matrix if the matrix order is large [33]. Therefore, we have chosen the latter option, which is called as the Finite-Element Discrete-Variable Representation, short for FE-DVR [88].

Bridge Function [88]

In Fig. 2.1, we display the numerical mapping over 0 to 6 a.u. with 3 elements and 4 DVR-basis functions in each element. Here we can notice that there is overlap between the neighboring elements: they use the same grid points as their DVR nodes, e.g., the last DVR node of element 1 is the first DVR node of the element 2.

The DVR function is non-zero only inside its definition interval; outside of this interval, it is always zero. In this sense, an electron moving in interval 1, for example, can move and only move in this region. It cannot go across the boundary and moves to the interval 2. To overcome this difficulty, we have to consider the overlapping nodes when constructing the Hamiltonian matrix. The “bridge function” is introduced here as a “bridge” to the neighboring regions (elements) as

$$\chi_{i1} = f_{i,n}(x) + f_{i+1,1}(x). \quad (2.11)$$

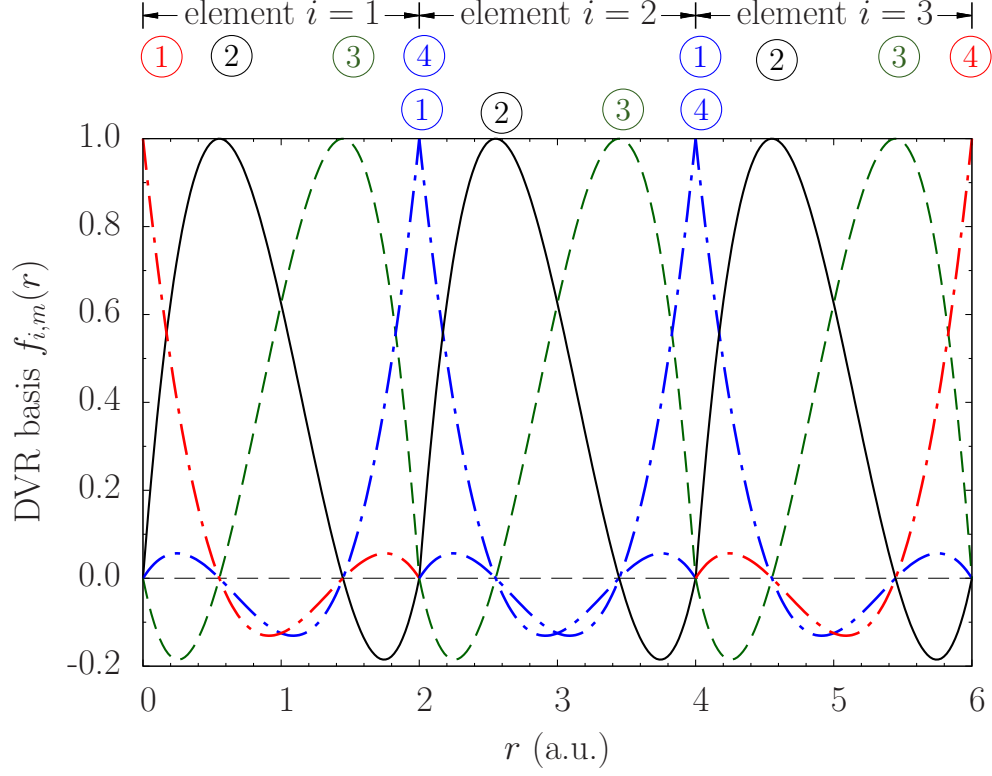


Figure 2.1: Schematic of DVR-basis functions with 3 finite elements. 3 sets of DVR-basis functions are equally mapping over $[0,6]$ by 3 elements. The element index i ranges from 1 to 3 on the top, the numbers over each elements within colored circles are served as indices of DVR-basis functions as well as indices of DVR nodes, they are the second index of a DVR-basis function $f_{i,m}(r)$. The 4 circled numbers on the top-left label the DVR-basis functions in element 1. The 4 circled numbers on the top-middle label the DVR-basis functions in element 2, and the 4 circled numbers on the top-right label the DVR-basis functions in element 3. The curves represent the DVR-basis functions, the black dashed lines display the ordinary functions, the blue dashed lines are the bridge functions. The red dashed-dotted lines are two DVR-basis functions to be dropped due to the boundary conditions.

It consists of the last DVR-basis function in i -th finite element and the first DVR-basis function in the $(i + 1)$ -th finite element. We use the first index i for a given finite element and keep the DVR-basis function index n as in Eqn. 2.9. See the blue dashed-dotted lines in Fig. 2.1 for example. It is obvious that the bridge function is continuous at the adjacent grid points, but its first derivative is not.

The new basis functions are now rewritten as

$$\chi_{i1} = f_{i,n}(x) + f_{i+1,1}(x), \quad (2.12)$$

$$\chi_{im} = f_{i,m}(x), \quad m = 2, \dots, n - 1. \quad (2.13)$$

These functions are not normalized, but can be simply normalized by

$$\chi_{i1} = \frac{f_{i,n}(x) + f_{i+1,1}(x)}{\sqrt{\omega_n^i + \omega_1^{i+1}}}, \quad (2.14)$$

$$\chi_{im} = \frac{f_{i,m}(x)}{\sqrt{\omega_m^i}}, \quad m = 2, \dots, n - 1. \quad (2.15)$$

Properties of FE-DVR Functions

Similar to the DVR-basis functions, the FE-DVR-basis functions now follow the relation:

$$f_{im}(x_j^{i'}) = \delta_{mj} \delta_{ii'}, \quad (2.16)$$

where i and i' are the index of elements. $\delta_{ii'}$ indicates the property of non-overlap between DVR basis functions of different finite elements.

We can approximate an integral into summation in the sense of the Gaussian-Lobatto quadrature

$$\int_0^\infty f_{im}(x) f_{i'm'}(x) dx \approx \delta_{ii'} \delta_{mm'} \omega_m^i, \quad (2.17)$$

and any local operator has a diagonal representation:

$$\int_0^\infty f_{im}(x) V(x) f_{i'm'}(x) dx \approx \delta_{ii'} \delta_{mm'} V(x_m^i) \omega_m^i. \quad (2.18)$$

2.2.3 One-Dimensional Hamiltonian Expression in Finite-Element Discrete-Variable Representation

Here we consider the simplest case of a one-dimensional wave function that is expanded as [88]

$$\psi(x) = \sum_{im} c_{im} \chi_{im}(x). \quad (2.19)$$

Considering a function $\psi(x)$ whose derivative is discontinuous at the connecting point x_0 , its first and second derivatives are given by

$$\frac{d\psi(x)}{dx} = f(x)\theta(x - x_0) + g(x)\theta(x_0 - x), \quad (2.20)$$

and

$$\frac{d^2\psi(x)}{dx^2} = f'(x)\theta(x - x_0) + g'(x)\theta(x_0 - x) + [f(x) - g(x)]\delta(x - x_0), \quad (2.21)$$

respectively, where $f(x)$ and $g(x)$ are two continuous differentiable functions, and

$$\theta(x) = \begin{cases} 0, & x < 0, \\ 1, & x > 0, \end{cases} \quad (2.22)$$

is the step function.

The expectation value of the radial kinetic energy can be calculated in symmetrical form as

$$\begin{aligned} -\frac{1}{2} \int_0^\infty dx \psi(x) \frac{d^2}{dx^2} \psi(x) &= -\frac{1}{2} \lim_{\epsilon \rightarrow 0} \sum_i \int_{x_i+\epsilon}^{x_{i+1}-\epsilon} dx \psi(x) \sum_m c_{im} \chi_{im}''(x) \\ &\quad -\frac{1}{2} \int_0^\infty dx \psi(x) \sum_{im} c_{im} \delta(x - x_i) [\chi'_{im}(x_i + 0) - \chi'_{im}(x_i - 0)] \\ &= \frac{1}{2} \sum_i \int_{x_i}^{x_{i+1}} dx \left(\frac{d\psi}{dx} \right)^2. \end{aligned} \quad (2.23)$$

Here ϵ is an arbitrary finite value. It therefore allows us to segregate the finite terms in Eqn. (2.23) from the δ -function terms. Thus, the matrix elements of the kinetic-energy operator in the FE-DVR frame can be calculated by

$$T_{mm'}^{ii'} = \frac{1}{2} (\delta_{ii'} + \delta_{ii'\pm 1}) \int_0^\infty dx \frac{d}{dx} \chi_{im}(x) \frac{d}{dx} \chi_{i'm'}(x). \quad (2.24)$$

The δ -functions in Eqn. (2.24) reflect the fact that a bridge function only covers two neighboring finite elements, and there is no overlap between DVR-basis functions beyond adjacent finite elements.

The first derivative in Eqn. (2.24) can be calculated by [88]

$$f'_{im}(x_{m'}^i) = \begin{cases} \frac{1}{x_m^i - x_{m'}^i} \prod_{k \neq m, m'} \frac{x_{m'}^i - x_k^i}{x_m^i - x_k^i}, & m \neq m', \\ \frac{1}{2\omega_m^i} (\delta_{m,n} - \delta_{m,1}), & m = m'. \end{cases} \quad (2.25)$$

The second line represents the derivatives in each end of each interval: $m = 1$ for the left end, and $m = n$ for the right end. The derivation is presented in Appendix B.

The kinetic-energy matrix elements shows block structure where each block is a dense matrix corresponding to a finite element. Adjacent blocks have an overlapping element, which is related to the connecting grid point between finite elements. In Fig. 2.2 we show an example matrix with 3 finite elements and 4 DVR functions each. Since the potential matrix is diagonal, it does not change the block structure.

2.3 Single-Active-Electron Model

For hydrogen or hydrogen-like atoms (He^+ , Li^{++} , etc), we can apply the one-particle TDSE [Eqn. (2.26)] to describe it. For a multi-electron system (He, Ar, etc), in principle, we have to adopt the multi-electron TDSE. However, if we only discuss SI, with the help of the single-active-electron (SAE) model [106], the multi-electron atoms can be approximately described by the single-particle TDSE.

The TDSE of the SAE can be written as:

$$i \frac{\partial \Psi(\mathbf{r}; t)}{\partial t} = \hat{H} \Psi(\mathbf{r}; t) = [\hat{T} + \hat{V}(\mathbf{r}, t)] \Psi(\mathbf{r}; t), \quad (2.26)$$

where the Hamiltonian is divided into the kinetic energy \hat{T} and potential energy \hat{V} operator of the system.

$$\begin{pmatrix}
H_{11} & H_{12} & H_{13} & 0 & 0 & 0 & 0 & 0 \\
H_{21} & H_{22} & H_{23} & 0 & 0 & 0 & 0 & 0 \\
H_{31} & H_{32} & H_{33} & H_{34} & H_{35} & H_{36} & 0 & 0 \\
0 & 0 & H_{43} & H_{44} & H_{45} & H_{46} & 0 & 0 \\
0 & 0 & H_{53} & H_{54} & H_{55} & H_{56} & 0 & 0 \\
0 & 0 & H_{63} & H_{64} & H_{65} & H_{66} & H_{67} & H_{68} \\
0 & 0 & 0 & 0 & 0 & H_{76} & H_{77} & H_{78} \\
0 & 0 & 0 & 0 & 0 & H_{86} & H_{87} & H_{88}
\end{pmatrix}$$

Figure 2.2: Example of a 1-D Hamiltonian matrix in the FE-DVR scheme with 3 finite elements and 4 DVR functions in each element. See Fig. 2.1 for detail.

2.3.1 Partial Wave Expansion

We expand the single-electron wave function in partial wave functions as:

$$\Psi(\mathbf{r}, t) = \sum_{l,m} \frac{\psi_{lm}(r, t)}{r} Y_{lm}(\hat{r}), \quad (2.27)$$

so the field-free Schrödinger equation now can be rewritten as

$$i \frac{\partial}{\partial t} \psi_{lm} = H_0 \psi_{lm}. \quad (2.28)$$

2.3.2 Particle in External Field

When a single particle system is exposed to an external electromagnetic field, its Hamiltonian needs to include an interacting term H_I . In the length gauge of the laser-atom interaction, it can be written as

$$H_I = \mathbf{E} \cdot \mathbf{r}, \quad (2.29)$$

where \mathbf{E} is the electric field component of the laser. Some investigations showed that it might be more economical to use the velocity gauge [121, 123], but some tests also showed indistinguishable results when using the same angular configuration in the velocity and length gauges [122]. Therefore, in this thesis, we only discuss results with length gauge. In most cases, we assume the external electric fields (XUV and IR) to be linearly polarized with sine-squared temporal profiles and write their electric-field vectors as

$$\mathbf{E}_a(t) = \begin{cases} \mathbf{E}_{0a} \sin^2\left(\frac{\pi t}{\tau_a}\right) \cos(\omega_a t + \varphi_a), & \text{if } 0 < t < \tau_a, \\ 0, & \text{else,} \end{cases} \quad (2.30)$$

where the index “ a ” stands for “XUV” or “IR”. Their common polarization direction defines our quantization axis which coincides with the z -axis of our coordinate system. $|\mathbf{E}_{0a}|$, τ_a , φ_a and ω_a denote electric-field amplitude, pulse length, carrier-envelope phase, and frequency, respectively. In this thesis we assume that the two pulses coincide and set $\varphi_{XUV} = \varphi_{IR} = 0$. We note that, in general, sine-squared pulses do not satisfy Maxwell’s equations, due to a non-vanishing DC component. For the pulses used in thesis, we found the DC component to be small and not induce noticeable changes in any of the observables we discuss.

For a linearly polarized laser, assuming the laser is polarized along the z direction, the interaction can be expressed as

$$H_I = E(t)z = E(t)r \cos \theta = E(t)r \sqrt{\frac{3\pi}{4}} Y_1^0(\theta, \phi), \quad (2.31)$$

where $E(t)$ is electric field and Y_1^0 is the $l = 1$, $m = 0$ spherical harmonic function. Due to the linear polarization of the laser field, the magnetic quantum number m remains unchanged, and Eqn. (2.28) can be simply written as

$$i \frac{d}{dt} \psi_l = H_0 \psi_l. \quad (2.32)$$

Since m will not change for linearly polarized laser (and the ground state with $l = 0$, $m = 0$ for H and He singlet state), we have the Schrödinger equation driven by linearly polarized laser

$$i \frac{d}{dt} \psi_l = H_0 \psi_l + \sum_{l'} E(t)r F(l, l') \psi_{l'}, \quad (2.33)$$

where

$$F(l, l') = \int Y_{lm}^* Y_{10} Y_{l'm'} d\Omega = \sqrt{\frac{3}{4\pi}} (2l+1)(2l'+1) \begin{pmatrix} l & 1 & l' \\ 0 & 0 & 0 \end{pmatrix} \begin{pmatrix} l & 1 & l' \\ m & 0 & m' \end{pmatrix}, \quad (2.34)$$

where $\begin{pmatrix} l & l_1 & l_2 \\ m & m_1 & m_2 \end{pmatrix}$ is a Wigner 3j-symbol which is related to the Clebsch-Gordan coefficients [113].

2.4 Two-Active-Electron Model

To study the behavior of a two-electron correlated system with many electrons, the most direct idea is to extend the SAE model to a many-electron system; this is called the two-active-electron (TAE) model. In the TAE model, only two electrons are active, all the rest electron(s) act as a short range potential in the potential curve of our target system. For the helium atom, there are only two electrons, so this short range potential term is 0.

2.4.1 General Form of the TDSE for the Helium Atom

The general form of the Schrödinger equation for a two-electron system in the two-active-electron model can be written as:

$$i \frac{\partial \Phi(\mathbf{r}_1, \mathbf{r}_2; t)}{\partial t} = H \Phi(\mathbf{r}_1, \mathbf{r}_2; t), \quad (2.35)$$

with the Hamiltonian

$$H = H_0 + V_{int}, \quad (2.36)$$

where

$$H_0 = -\frac{1}{2}[\nabla_1^2 + \nabla_2^2] - \frac{2}{r_1} - \frac{2}{r_2}. \quad (2.37)$$

The interaction potential

$$V_{int} = \frac{1}{|\mathbf{r}_1 - \mathbf{r}_2|} + [\mathbf{E}_{XUV}(t) + \mathbf{E}_{IR}(t)] \cdot (\mathbf{r}_1 + \mathbf{r}_2) \quad (2.38)$$

includes the electronic correlation and interactions between the electrons and external XUV and IR electric fields in the dipole length gauge. The electric fields are given in Eqn. (2.30).

We solve Eqn. (2.35) by expanding the time-dependent two-electron wave function in bipolar spherical harmonics [34, 81],

$$\mathcal{Y}_{l_1 l_2}^{LM}(\Omega_1, \Omega_2) = \sum_{m_1 m_2} C_{l_1 m_1 l_2 m_2}^{LM} Y_{l_1 m_1}(\Omega_1) Y_{l_2 m_2}(\Omega_2), \quad (2.39)$$

according to

$$\Phi(\mathbf{r}_1, \mathbf{r}_2; t) = \sum_{LM} \sum_{l_1, l_2} \frac{\psi_{l_1 l_2}^{(LM)}(r_1, r_2; t)}{r_1 r_2} \mathcal{Y}_{l_1 l_2}^{L, M}(\Omega_1, \Omega_2). \quad (2.40)$$

The functions $Y_{l_i m_i}(\Omega_i)$ are ordinary spherical harmonics in the solid angles $\Omega_i = (\theta_i, \phi_i)$ of the two electrons ($i = 1, 2$). The coupling of the two electrons' individual angular momenta with quantum numbers (l_1, m_1) and (l_2, m_2) to the total angular momentum of the two-electron system with quantum numbers (L, M) is written in terms of the Clebsch-Gordan coefficients $C_{l_1 m_1 l_2 m_2}^{LM}$. Assuming the helium atoms are initially in the singlet-spin 1S_0 ground state with $L = M = 0$, angular momentum conservation implies that the atom remains in $M = 0$ states during their interaction with the XUV and IR electric fields. Starting with helium atoms in the 1S_0 state further implies that the radial parts of the atomic wave function are symmetric upon electron exchange, i.e. $\Phi(\mathbf{r}_1, \mathbf{r}_2) = \Phi(\mathbf{r}_2, \mathbf{r}_1)$, such that for our case ($M = 0$) only terms with even $L - l_1 - l_2$ contribute to the expansion Eqn. (2.39).

In order to determine the radial wave functions $\psi_{l_1 l_2}^L(r_1, r_2)$ in Eqn. (2.40), we adopt the FE-DVR implementation and numerically propagate the radial TDSE for $M = 0$ [33, 119],

$$i \frac{\partial}{\partial t} \psi_{l_1 l_2}^{L0}(r_1, r_2; t) = \sum_{L' l'_1 l'_2} \langle l_1, l_2, L, 0 | H | l'_1, l'_2, L', 0 \rangle \psi_{l'_1 l'_2}^{L'0}(r_1, r_2; t), \quad (2.41)$$

on a two-dimensional numerical grid for the radii r_1 and r_2 . In order to simplify the notation we will drop the superscript M throughout the remainder of this thesis. Details of the partial-wave analysis and angular-momentum-coupling constraints are given in the next sub-section. Because we will discuss the case that the two electrons are initially in a singlet spin state (and since we employ LS coupling), $\Psi(\mathbf{r}_1, \mathbf{r}_2; t) = \Psi(\mathbf{r}_2, \mathbf{r}_1; t)$, and the radial part of the wave function must satisfy the relation

$$\psi_{l_1 l_2}^L(r_1, r_2; t) = (-1)^{l_1 + l_2 - L} \psi_{l_2 l_1}^L(r_2, r_1; t). \quad (2.42)$$

In our numerical simulations, we therefore only include those partial waves with angular momenta $l_1 + l_2 - L = \text{even}$.

We apply the DVR method based on the Gauss-Lobatto quadrature rule. This method is known as an efficient procedure for obtaining highly accurate results with relatively small numbers of radial grid points. Subdivision of the numerical intervals for the radial coordinates r_1 and r_2 into smaller “finite” elements translates the Hamiltonian Eqn. (2.36) into a large sparse matrix that can be efficiently diagonalized. The FE-DVR method is well established for solving the radial two-electron TDSE and more details of its implementation can be found in the literature [33, 58, 92, 119].

We solve Eqn. (2.41) by numerical wave-function propagation on the (r_1, r_2) grid points, repeatedly applying the split time-evolution operator [66] over equally spaced small time steps Δt ,

$$\psi(t + \Delta t) = e^{-i\hat{H}_0 \frac{\Delta t}{2}} e^{-i\hat{V}_{int}\Delta t} e^{-i\hat{H}_0 \frac{\Delta t}{2}} \psi(t) + O(\Delta t^3). \quad (2.43)$$

Here we need to mention that to obtain the accuracy $O(\Delta t^3)$, the Hamiltonian \hat{H} should be evaluated at the middle point $t + \Delta t/2$ of t and $t + \Delta t$.

In order to propagate Eqn. (2.41) in time, we employ the Lanczos method [26, 78]. At each numerical grid point (r_1, r_2) the Hamiltonian H_0 and the interaction potential V_{int} are represented as $N \times N$ matrices \hat{H}_0 and \hat{V}_{int} , respectively, in the channel indices and must be diagonalized. N is the total number of channels (partial waves we adopted in the TDSE), and each channel is defined by the set of quantum numbers (L, l_1, l_2) . We will discuss how to choose the partial waves in Chap. 4.

Since the FE-DVR scheme is based on the Gauss-Lobatto quadrature rule [1], it requires the integrand to be a polynomial function for highly accurate results. However, part of our numerical effort consists in calculating the matrix elements $\langle \psi_{l_1 l_2}^{L'}(r_1, r_2) | 1 / (|\mathbf{r}_1 - \mathbf{r}_2|) | \psi_{l_1 l_2}^L(r_1, r_2) \rangle$ of the electronic interaction for which the Gauss-Lobatto scheme is not appropriate. To diagonalize the potential matrix without loss of accuracy, we instead calculate this integral by solving Poisson’s equation [120], following the work of McCurdy *et al.* [58]

in 2004.

2.4.2 Radial TDSE and Coefficients of Angular Momentum Coupling Functions

The radial TDSE [Eqn. (2.41)] can be written as

$$i\frac{\partial}{\partial t}\psi_{l_1 l_2}^L(r_1, r_2; t) = [\hat{T} + \hat{V}_c]\psi_{l_1 l_2}^L(r_1, r_2; t) + \sum_{L' l'_1 l'_2} \hat{V}_{F_0}(\lambda, \lambda')\psi_{l'_1 l'_2}^{L'}(r_1, r_2; t) + \sum_{L' l'_1 l'_2} \hat{V}_{F_{12}}(\lambda, \lambda')\psi_{l'_1 l'_2}^{L'}(r_1, r_2; t), \quad (2.44)$$

where the collective angular momentum quantum numbers are defined as $\lambda = \{L, l_1, l_2\}$ and $\lambda' = \{L', l'_1, l'_2\}$, and

$$\hat{T} = -\frac{1}{2}\frac{\partial^2}{\partial r_1^2} - \frac{1}{2}\frac{\partial^2}{\partial r_2^2} \quad (2.45)$$

is the total kinetic energy operator for the two electrons, and

$$\hat{V}_c = -\frac{2}{r_1} + \frac{l_1(l_1 + 1)}{2r_1^2} - \frac{2}{r_2} + \frac{l_2(l_2 + 1)}{2r_2^2} \quad (2.46)$$

includes the Coulomb interactions with the nucleus and the centrifugal potentials. The angular-momentum coupling matrix elements are

$$\hat{V}_{F_0}(\lambda, \lambda') = \sum_{l=0}^{\infty} \frac{4\pi(-1)^l}{\sqrt{2l+1}} \frac{r_{<}^l}{r_{>}^{l+1}} F_0(\lambda, \lambda') \quad (2.47)$$

for the electronic interaction, where $r_{<} = \min\{r_1, r_2\}$, $r_{>} = \max\{r_1, r_2\}$; and

$$\hat{V}_{F_{12}}(\lambda, \lambda') = \frac{4\pi}{\sqrt{3}} E(t) [r_1 F_1(\lambda, \lambda') + r_2 F_2(\lambda, \lambda')] \quad (2.48)$$

for the interaction with the external electric field $E(t) = E_{XUV} + E_{IR}$. Following Refs. [33, 80–83], the angular-momentum coupling matrix elements can be written as

$$F_0 = \sqrt{(2l+1)^2(2l'_1+1)(2l'_2+1)(2L'+1)/(4\pi)^2} \\ \times C_{10l'_1 0}^{l_1 0} C_{10l'_2 0}^{l_2 0} C_{00L' 0}^{L 0} \times \begin{Bmatrix} l & l'_1 & l_1 \\ l & l'_2 & l_2 \\ 0 & L' & L \end{Bmatrix}, \quad (2.49)$$

$$F_1 = \sqrt{9(2l'_1+1)(2l'_2+1)(2L'+1)/(4\pi)^2} \\ \times C_{10l'_1 0}^{l_1 0} C_{00l'_2 0}^{l_2 0} C_{10L' 0}^{L 0} \times \begin{Bmatrix} 1 & l'_1 & l_1 \\ 0 & l'_2 & l_2 \\ 1 & L' & L \end{Bmatrix}, \quad (2.50)$$

and

$$F_2 = \sqrt{9(2l'_1+1)(2l'_2+1)(2L'+1)/(4\pi)^2} \\ \times C_{00l'_1 0}^{l_1 0} C_{10l'_2 0}^{l_2 0} C_{10L' 0}^{L 0} \times \begin{Bmatrix} 0 & l'_1 & l_1 \\ 1 & l'_2 & l_2 \\ 1 & L & L' \end{Bmatrix}, \quad (2.51)$$

where Clebsch-Gordan coefficients and $9j$ symbols [35] are denoted as C_{\dots} and $\{\dots\}$, respectively.

In terms of the collective quantum numbers λ and λ' , Eqn. (2.44) can be cast in the more compact form [33]

$$i \frac{\partial}{\partial t} \psi_{\lambda}(r_1, r_2; t) = [\hat{T} + \hat{V}_c] \psi_{\lambda}(r_1, r_2; t) + \sum_{\lambda'} [\hat{V}_{F_0}(\lambda, \lambda') + \hat{V}_{F_{12}}(\lambda, \lambda')] \psi_{\lambda'}(r_1, r_2; t). \quad (2.52)$$

2.5 Continuum-State Wave Functions

To extract the physical information from the final-state wave function, we often need to project the final state onto the asymptotic correlated two-electron wave functions. Since no accurate closed-form expressions of such asymptotic correlated two-electron wave functions are known for the three-body Coulomb problem [27, 50], we freely propagate our wave function for a sufficiently long time (e.g., 40 a.u.) after the action of external field to reduce the effect of final-state correlation. We proceed by neglecting the excited states and the final-state interaction between the emitted electrons, leaving the inclusion of electronic

correlation in the final state [7] to future investigations. This allows us to approximately compute DI probabilities by subtracting the overlap with the 1S_0 ground state wave function from $\Phi(\mathbf{r}_1, \mathbf{r}_2; t_f)$ before projecting this difference onto the uncorrelated double Coulomb continuum states [46]. These uncorrelated double Coulomb continuum states are eigenstates of the uncorrelated Hamiltonian which neglects the electron-electron interaction term $\hat{\mathbf{H}}_{12} = |\mathbf{r}_1 - \mathbf{r}_2|^{-1}$.

The uncorrelated Hamiltonian reads

$$H_0 = \frac{p_1^2}{2} + \frac{p_2^2}{2} - \frac{Z}{r_1} - \frac{Z}{r_2} = H_1 + H_2. \quad (2.53)$$

This is a separable Hamiltonian. Z is the charge number of particle, it equals 2 for helium atoms. It is the sum of two independent one-particle Hamiltonians (H_1 and H_2 as indicated above). The one-particle Hamiltonian can be written as

$$H = \frac{p^2}{2} - \frac{Z}{r}. \quad (2.54)$$

Its eigenstates can be separated into a radial and an angular parts:

$$\Phi_{klm}(\mathbf{r}) = \frac{\phi_{kl}(r)}{r} Y_m^l(\Omega), \quad (2.55)$$

where the angular part is expressed by the spherical harmonics function $Y_m^l(\Omega)$. The radial part, $\phi(r)$, has different forms for *bound states* and *unbound states*. The regular solution for the unbound states is given by the regular radial Coulomb function $F_l(\eta, \kappa r)$ [5, 27, 46]

$$F_l(\eta, \kappa r) = 2^l e^{-\frac{1}{2}\pi\eta} \frac{|\Gamma(l+1+i\eta)|}{(2l+1)!} e^{-i\kappa r} (\kappa r)^{l+1} F(l+1-i\eta, 2l+2; 2i\kappa r), \quad (2.56)$$

and

$$\phi_{kl}(r) = \sqrt{\frac{2}{\pi}} F_l(\eta, \kappa r). \quad (2.57)$$

The confluent hypergeometric series $F(a, b; z)$ is given by

$$F(a, b; z) = \sum_{n=0}^{\infty} \frac{\Gamma(a+n)}{\Gamma(a)} \frac{\Gamma(b)}{\Gamma(b+n)} \frac{z^n}{n!}. \quad (2.58)$$

The asymptotic limit of $F_l(\eta, \kappa r)$ at $r \rightarrow \infty$ has sinusoid-like form

$$F_l(\eta, \kappa r) \rightarrow \sin\left(kr - \eta \ln 2kr - \frac{l\pi}{2} + \sigma_l\right). \quad (2.59)$$

Here, the Coulomb parameter η is defined by

$$\eta = -\frac{Z}{k}, \quad (2.60)$$

with $Z=2$ for helium. The Coulomb phase σ_l is

$$\sigma_l = \arg[\Gamma(l + 1 + i\eta)]. \quad (2.61)$$

The radial continuum-state wave function satisfies

$$\int_0^{+\infty} \phi_{kl}(r) \phi_{k'l}(r) dr = \delta(k - k'). \quad (2.62)$$

Thus, the continuum states are normalized in momentum space. The singlet two-electron Coulomb continuum wave function satisfying the incoming boundary condition (-) is given by [27, 48]

$$\psi_{\mathbf{k}_1, \mathbf{k}_1}^{(-)} = \frac{1}{\sqrt{2}} [\psi_{\mathbf{k}_1}^{(-)}(\mathbf{r}_1) \psi_{\mathbf{k}_2}^{(-)}(\mathbf{r}_2) + \psi_{\mathbf{k}_2}^{(-)}(\mathbf{r}_1) \psi_{\mathbf{k}_1}^{(-)}(\mathbf{r}_2)], \quad (2.63)$$

which is the product of incoming-wave Coulomb continuum wave functions $\psi_{\mathbf{k}_i}^{(-)}(\mathbf{r}_i)$ ($i = 1, 2$) with emitted electron momenta \mathbf{k}_1 and \mathbf{k}_2 [5, 27].

2.6 Physical Variables

2.6.1 Total Energy

The total energy of a quantum system is defined by the expectation value of \hat{H} ,

$$E_{tot} = \langle \hat{H} \rangle = \langle \Psi | \hat{H} | \Psi \rangle \quad (2.64)$$

$$= \sum_{\lambda, \lambda'} \int dr_1 dr_2 \psi_{\lambda\lambda'}^\dagger(r_1, r_2) H^{\lambda\lambda'}(r_1, r_2) \psi_{\lambda\lambda'}(r_1, r_2) \quad (2.65)$$

$$\approx \sum_{i, j; \lambda, \lambda'} \omega_i \omega_j \psi_{\lambda\lambda', ij}^\dagger H_{ij}^{\lambda\lambda'} \psi_{\lambda\lambda', ij} \quad (2.66)$$

where i, j are numerical grid indices, λ and λ' are indices of partial waves, ω_i and ω_j are the weights of the FE-DVR grids at the grid points r_i and r_j , and the $H_{ij}^{\lambda\lambda'}$ are Hamiltonian matrix elements.

2.6.2 Momentum and Energy Distributions

In order to obtain energy and angle-dependent double-ionization probabilities, we need to analyze the final state of the doubly-ionized atom with regard to the asymptotic momentum vectors of both emitted electrons. In principle, quantum mechanics demands this to be done by projecting the wave function of the system, $\Phi(\mathbf{r}_1, \mathbf{r}_2; t_f)$, at a sufficiently long time t_f after the action of the IR and XUV pulses onto asymptotic two-electron continuum wave functions. Since no accurate closed-form expressions of such asymptotic correlated two-electron wave functions are known for the three-body Coulomb problem [27], we proceed by neglecting the final-state interaction, leaving the inclusion of electronic correlation in the final state [7] to future investigations.

In order to remove spurious contributions to the DI probability amplitude that are due to the non-orthogonality of this approximate asymptotic wave function and the initial state Φ_{1S_0} , we subtract the overlap with $\Phi_{1S_0}(\mathbf{r}_1, \mathbf{r}_2)$ from $\Phi(\mathbf{r}_1, \mathbf{r}_2; t_f)$ to yield

$$\tilde{\Phi}(\mathbf{r}_1, \mathbf{r}_2; t) = \Phi(\mathbf{r}_1, \mathbf{r}_2; t) - \langle \Phi_{1S_0} | \Phi(t) \rangle \Phi_{1S_0}(\mathbf{r}_1, \mathbf{r}_2). \quad (2.67)$$

Numerical propagation of $\Phi(\mathbf{r}_1, \mathbf{r}_2; t)$ allows us to compute the DI probability

$$P(\mathbf{k}_1, \mathbf{k}_2) = |\langle \psi_{\mathbf{k}_1, \mathbf{k}_2}^{(-)} | \tilde{\Phi}(\mathbf{r}_1, \mathbf{r}_2; t_f) \rangle|^2 \quad (2.68)$$

for detecting photoelectrons with momenta \mathbf{k}_1 and \mathbf{k}_2 [27, 46] as a six-dimensional distribution in the momentum magnitudes k_1 and k_2 and corresponding momentum directions $\Omega_i = \hat{\mathbf{k}}_i = (\theta_i, \phi_i)$, $i=1, 2$.

This momentum distribution is calculated by

$$P(\mathbf{k}_1, \mathbf{k}_2) = \frac{1}{4\pi^2 k_1^2 k_2^2} \left| \sum_{L l_1 l_2} (-1)^{l_1+l_2} e^{i(\sigma_{l_1} + \sigma_{l_2})} \mathcal{Y}_{L0}^{l_1 l_2}(\Omega_1, \Omega_2) M_{l_1 l_2}^L(k_1, k_2) \right|^2, \quad (2.69)$$

where

$$M_{l_1 l_2}^L(k_1, k_2) = \int dr_1 \int dr_2 r_1 r_2 \phi_{k_1 l_1}(r_1) \phi_{k_2 l_2}(r_2) \tilde{\psi}(r_1, r_2, t_f) \quad (2.70)$$

is the partial-wave amplitude in momentum space.

Integration over all angles results in the correlated energy distribution

$$P(E_1, E_2) = \frac{1}{k_1 k_2} \iint d\Omega_1 d\Omega_2 P(\mathbf{k}_1, \mathbf{k}_2), \quad (2.71)$$

where $E_1 = k_1^2/2$ and $E_2 = k_2^2/2$ are the final (asymptotic) energies of the emitted electrons.

2.6.3 Triple Differential Cross Sections

Integration of (2.68) over k_2 (or k_1) leads to the triple differential cross section (TDCS) [27, 119]

$$\frac{d^3\sigma}{dE_1 d\Omega_1 d\Omega_2} = \left(\frac{\omega}{I_0}\right)^2 \frac{k_1}{T_{\text{eff}}} \int dk_2 k_2^2 P(\mathbf{k}_1, \mathbf{k}_2). \quad (2.72)$$

The TDCS is defined in terms of the effective interaction time

$$T_{\text{eff}} = \int dt \left(\frac{I(t)}{I_0}\right)^{N_{\text{XUV}}} \quad (2.73)$$

for a given number N_{XUV} of absorbed XUV photons and XUV intensity profile $I(t)$. For the limiting case of a rectangular temporal pulse profile, T_{eff} becomes identical to the total XUV pulse duration τ for $N_{\text{XUV}} = 1$ and equal to τ for arbitrary N_{XUV} . For a sine-squared pulse shape of duration τ , the effective time for SPDI is

$$T_{\text{eff}}^{(1)} = \frac{3}{8}\tau. \quad (2.74)$$

For TPDI it is [27, 119]

$$T_{\text{eff}}^{(2)} = \frac{35}{128}\tau. \quad (2.75)$$

The single differential cross section (SDCS) can then be obtained by integrating Eqn. (2.72) over $\hat{\mathbf{k}}_1$ and $\hat{\mathbf{k}}_2$,

$$\frac{d\sigma}{dE_1} = \frac{1}{4\pi^2 k_1} \left(\frac{\omega}{I_0}\right)^2 \frac{1}{T_{\text{eff}}} \int dk_2 \sum_{L, l_1, l_2} |M_{l_1 l_2}^L(k_1, k_2)|^2, \quad (2.76)$$

to give the energy spectrum of one ionized electron.

2.6.4 Joint Angular Distribution and Mutual Angular Distribution

We evaluate JADs for co-planar DI at vanishing azimuthal angles ($\phi_1 = \phi_2 = 0$) and for fixed energy sharing, integrating over the emitted electron speeds,

$$P(\theta_1, \theta_2) = \int dk_1 dk_2 k_1^2 k_2^2 \delta(k_1 - k_2) P(\mathbf{k}_1, \mathbf{k}_2). \quad (2.77)$$

We define the angle difference between two emitted photoelectrons as the mutual angle θ_{12} , which is constant along the 45° direction in JAD:

$$\theta_{12} = \begin{cases} \theta_2 - \theta_1, & \text{if } \theta_1 < \theta_2, \\ \theta_2 - \theta_1 + 2\pi, & \text{if } \theta_1 > \theta_2. \end{cases} \quad (2.78)$$

Integration of the Eqn. (2.77) over θ_1 (or θ_2) at fixed mutual angles θ_{12} defines the mutual angular distribution (MAD)

$$P(\theta_{12}; \varepsilon) = \int d\theta_1 P(\theta_1, \theta_1 + \theta_{12}, \varepsilon). \quad (2.79)$$

We define the dominant angular difference Θ_{12} as the angle where

$$\left. \frac{\partial P(\theta_{12}; \varepsilon)}{\partial \theta_{12}} \right|_{\theta_{12}=\Theta_{12}} = 0 \quad \text{and} \quad \left. \frac{\partial^2 P(\theta_{12}; \varepsilon)}{\partial \theta_{12}^2} \right|_{\theta_{12}=\Theta_{12}} < 0. \quad (2.80)$$

2.6.5 Emission-Asymmetry Parameter

To quantitatively describe the asymmetrical emission pattern in helium DI, we define the asymmetry parameter

$$A(\theta_1; \varepsilon) = \frac{\left(\int_{-\pi/2}^{\pi/2} - \int_{\pi/2}^{3\pi/2} \right) P(\theta_1, \theta; \varepsilon) d\theta}{\left(\int_{-\pi/2}^{\pi/2} + \int_{\pi/2}^{3\pi/2} \right) P(\theta_1, \theta; \varepsilon) d\theta}. \quad (2.81)$$

When A is close to 1, the two photoelectrons mostly go in the same direction (into the same hemisphere); for instance in side-by-side emission. If A is close to -1, the two photoelectrons mostly go in opposite directions (into two different hemispheres), for instance in back-to-back emission. This asymmetry parameter is an indicator of the electronic correlation in double photoionization. $A \approx -1$ is related to strong electronic correlation between

photoelectrons in the DI process. In our discussion, mostly we set the $\theta_1 = 0$, which means that the electron is emitted along the laser and/or XUV polarization directions.

2.7 Symmetry in Joint Angular Distribution

Figure 2.3 displays two typical JAD, both linear color scale, for (a) single-photon DI and (b) three-photon DI at unequal energy sharing. Both plots display the symmetries about two diagonal lines.

The symmetry about the second diagonal line (45° slope) is caused by the indistinguishability of two identical electrons. It is given by

$$P(\theta_2, \theta_1) = P(\theta_1, \theta_2). \quad (2.82)$$

The symmetry about the main diagonal line ($\theta_1 + \theta_2 = 360^\circ$) is expressed as

$$P(\theta_1, \theta_2) = P(2\pi - \theta_1, 2\pi - \theta_2). \quad (2.83)$$

The detailed derivation for Eqn. (2.83) can be found in Appendix A.

The periodicity is given by

$$P(\theta_1, \theta_2) = P(2\pi + \theta_1, 2\pi + \theta_2), \quad (2.84)$$

and the symmetry about the center (π, π) by

$$P(\theta_1, \theta_2) = P(2\pi - \theta_1, 2\pi - \theta_2). \quad (2.85)$$

2.8 Numerical Convergence Tests

We have carried out extensive tests using our new FE-DVR code to assess the accuracy of our numerical results relative to the numerical effort (in terms of computing time and random access memory) and published data. For example, the accurate helium ground-state energy is [97]

$$E_g^{He} = -2.903\,724\,4 \text{ a.u.} \quad (2.86)$$

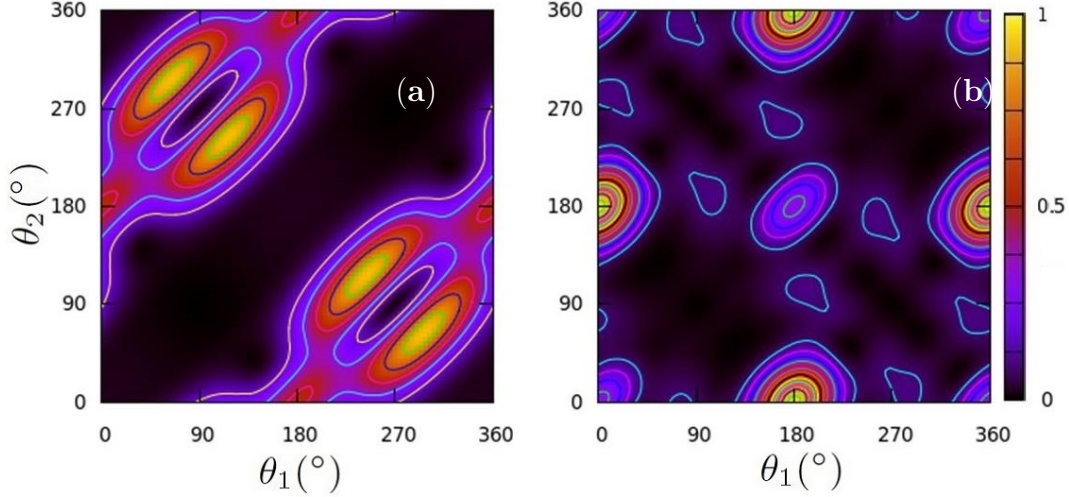


Figure 2.3: Two typical joint angular distributions as contour plots. Panel (a) is for single-photon DI and panel (b) is for three-photon DI at unequal energy sharing.

and the experimental result is

$$E_g^{He} = -2.903\,561\,2\,a.u. \quad (2.87)$$

We use 50 finite elements and 6 grid points in each element, with the outer boundary $r_{\max}=76$ a.u., and angular momenta l_1 and l_2 are up to 5. We obtain the current helium ground state energy

$$E_{FE-DVR}^{He} = -2.903\,700\,2\,a.u. \quad (2.88)$$

This result is in excellent agreement with both theory and experiment results. In Appendix (C), we discuss in detail the convergence tests on angular momenta (L , l_1 , l_2), propagation time, time step, and numerical grid size.

Chapter 3

Application to the Energy levels of Hydrogen Atoms and Helium Atoms with Single-Active Electron Model

The one-electron atom is the simplest atomic system. For many-electron atomic system, there is no analytical solution. However, if we only discuss single ionization, we can use the the SAE model, which reduces the complex many-electron system to a hydrogen-like system. In this chapter, we will apply the FE-DVR scheme to solve the SAE model, including hydrogen atoms and helium atoms.

For atoms with more than one electron, due to the charge screening effect [112], the effective nuclear charge is not exactly equal to the nuclear charge number. The SAE model was developed to describe the potential behaviors of many-electron atoms. There are many different models [106, 118], such as the GSZ potential model by Green, Sellin, and Zachor [23, 25] and Muller potential model [62] but we only list the parameters of the Tong-Lin SAE potential model [106], which is used in this chapter.

The effective potential in the Tong-Lin SAE model is given by

$$V(r) = -\frac{Z_c + a_1e^{-a_2r} + a_3re^{-a_4r} + a_5e^{-a_6r}}{r}. \quad (3.1)$$

Here, Z_c is the asymptotic charge that can be seen by the active electron, which is always 1 for SAE. The a_i 's are fitting parameters. For the H atom, there is only one electron, so Z_c is equal to 1, and all the other parameters are zero. In Tab. 3.1, we give the parameters in

the Tong-Lin SAE model for noble gas atoms.

Table 3.1: Atomic parameters of Tong-Lin SAE potential model adapted from Ref. [106].

Atom	Z_c	a_1	a_2	a_3	a_4	a_5	a_6
H	1.0	0.000	0.000	0.000	0.000	0.000	0.000
He	1.0	1.231	0.662	-1.325	1.236	-0.231	0.480
Ne	1.0	8.069	2.148	-3.570	1.986	0.931	0.602
Ar	1.0	16.039	2.007	-25.543	4.525	0.961	0.443
Xe	1.0	51.356	2.112	-99.927	3.737	1.644	0.431

3.1 Hydrogen Atoms

The hydrogen atom is the only atomic system we can solve analytically. So it is good to use H atoms as our first test of the SAE model and FE-DVR scheme. In this section, we compare our numerical results of energy levels with the analytical results for the hydrogen atom. In Tab. 3.2 and Tab. 3.3, we list analytical energy levels and compare them with our numerical results with $N_{fe} = 60$ finite elements and $N_{gr} = 4$ and $N_{gr} = 10$ grid points in each finite element, respectively. In each table, the grid is mapped over the radial interval $[0,137.5]$. For detailed mapping information, see Tabs. 3.4, 3.5 and Fig. 3.1.

Table 3.2: Energy levels of hydrogen atoms. Lobatto node number $N_{gr} = 4$. Up to $n=7$, the error between current value and accurate value is less than 1%.

energy level	present value	accurate value	error (%)
1	-0.499 845 064 6	-0.500 000 000 0	0.030 987 08
2	-0.124 993 427 4	-0.125 000 000 0	0.005 258 09
3	-0.055 554 213 2	-0.055 555 555 6	0.002 416 20
4	-0.031 249 520 7	-0.031 250 000 0	0.001 533 88
5	-0.019 999 775 0	-0.020 000 000 0	0.001 124 83
6	-0.013 888 756 2	-0.013 888 888 9	0.000 955 06
7	-0.010 198 186 7	-0.010 204 081 6	0.057 770 15
8	-0.007 591 876 3	-0.007 812 500 0	2.823 983 49
9	-0.004 796 407 3	-0.006 172 839 5	22.298 201 82
10	-0.001 255 376 9	-0.005 000 000 0	74.892 461 05

Table 3.3: Energy levels of the hydrogen atoms. Lobatto node number $N_{gr} = 10$. Up to $n=5$, our current FE-DVR eigenvalues and the accurate values are exactly the same, and up to $n=7$, the error between present value and accurate value is less than 1%.

energy level	present value	accurate value	error (%)
1	-0.500 000 000 0	-0.500 000 000 0	0.000 000 00
2	-0.125 000 000 0	-0.125 000 000 0	0.000 000 00
3	-0.055 555 555 6	-0.055 555 555 6	0.000 000 00
4	-0.031 250 000 0	-0.031 250 000 0	0.000 000 00
5	-0.020 000 000 0	-0.020 000 000 0	0.000 000 00
6	-0.013 888 880 0	-0.013 888 888 9	0.000 063 93
7	-0.010 198 263 0	-0.010 204 081 6	0.057 023 03
8	-0.007 591 939 8	-0.007 812 500 0	2.823 170 18
9	-0.004 796 485 1	-0.006 172 839 5	22.296 940 88
10	-0.001 255 470 0	-0.005 000 000 0	74.890 599 91

In Fig. 3.1, we display the finite-element mapping over $[0,137.5]$. For near-core mapping, the element size is small, the first element size is 1. The element sizes increase exponentially and the last element size is 4.37.

3.2 Helium Atoms with Single-Active-Electron Model

In this section, we apply the SAE model to the helium atom. We compare our calculated energy levels of helium atoms with experimental results.

3.2.1 Energy Levels

In Tab. 3.6, we display the first 10 energy levels of neutral He (singlet states with $S=0$) with total angular momentum $L = 0$. In tests for the hydrogen atom with the same grid point setting, we found the calculated energy levels in very highly accurate agreement with analytical values for $n < 8$. In this section, we can see that the numerical results of the SAE model obtained in the FE-DVR method agree well with experimental values. Column 1 shows the present results, obtained by diagonalizing the Hamiltonian of the helium atom in SAE model. We map our grid over $[0, 137.5]$ with 60 elements and 10 nodes in each element. The first element size is 1 a.u., and the last one is 4.37 a.u. Column 2 lists the

Table 3.4: The grid points in the first and last 10 elements, and each finite element is mapped by 4 Gaussian-Lobatto nodes.

element index	grid points			
1	0.000000	0.276393	0.723607	1.000000
2	1.000000	1.283390	1.741925	2.025315
3	2.025315	2.315879	2.786022	3.076586
4	3.076586	3.374506	3.856551	4.154470
5	4.154470	4.459932	4.954180	5.259641
6	5.259641	5.572836	6.079595	6.392790
7	6.392790	6.713913	7.233501	7.554624
8	7.554624	7.883876	8.416618	8.745870
9	8.745870	9.083458	9.629686	9.967273
10	9.967273	10.313406	10.873462	11.219596
⋮	⋮	⋮	⋮	⋮
51	98.373735	99.338442	100.899371	101.864078
52	101.864078	102.853207	104.453651	105.442779
53	105.442779	106.456948	108.097907	109.112076
54	109.112076	110.151918	111.834419	112.874261
55	112.874261	113.940428	115.665521	116.731687
56	116.731687	117.824843	119.593607	120.686764
57	120.686764	121.807593	123.621134	124.741964
58	124.741964	125.891167	127.750618	128.899821
59	128.899821	130.078117	131.984640	133.162936
60	133.162936	134.371061	136.325847	137.533972

Table 3.5: The grids in the first and last 5 elements, and each finite element is mapped by 10 Gaussian-Lobatto nodes.

element index	grid points				
1	0.000000	0.040233	0.130613	0.261038	0.417361
	0.582639	0.738962	0.869387	0.959767	1.000000
2	1.000000	1.041252	1.133920	1.267646	1.427926
	1.597389	1.757669	1.891396	1.984064	2.025315
3	2.025315	2.067611	2.162625	2.299736	2.464074
	2.637827	2.802165	2.939276	3.034290	3.076586
4	3.076586	3.119953	3.217372	3.357954	3.526453
	3.704604	3.873102	4.013685	4.111104	4.154470
5	4.154470	4.198935	4.298820	4.442961	4.615725
	4.798387	4.971150	5.115292	5.215177	5.259641
⋮	⋮	⋮	⋮	⋮	⋮
56	116.731687	116.890812	117.248272	117.764110	118.382380
	119.036071	119.654340	120.170179	120.527639	120.686764
57	120.686764	120.849917	121.216426	121.745323	122.379244
	123.049483	123.683404	124.212301	124.578811	124.741964
58	124.741964	124.909247	125.285034	125.827321	126.477289
	127.164496	127.814465	128.356751	128.732538	128.899821
59	128.899821	129.071340	129.456640	130.012654	130.679077
	131.383680	132.050103	132.606117	132.991418	133.162936
60	133.162936	133.338796	133.733850	134.303940	134.987234
	135.709674	136.392967	136.963057	137.358112	137.533972

Table 3.6: First 10 bound-state energy levels. The present results are calculated for singlet states by diagonalization of Hamiltonian matrix with 60 finite elements and 10 DVR nodes in each finite element mapping over radial coordinate. The experimental data were retrieved from NIST Atomic Spectra Database [67] on March 29, 2015.

Because there is no corresponding singlet and triplet states in SAE model, we compare the SAE results with the averages of experimental energy levels of singlet and triplet states.

n	current value	experimental value	average	error (%)
1	-0.903 800 996 6	-0.903 67	-	0.014 38
2	-0.160 010 729 9	-0.175 23 (3S) -0.145 97 (1S)	-0.160 60	0.366 93
3	-0.064 816 780 0	-0.068 69 (3S) -0.061 27 (1S)	-0.064 98	0.251 18
4	-0.035 008 343 0	-0.036 51 (3S) -0.033 58 (1S)	-0.035 045	0.104 72
5	-0.021 883 741 2	-0.022 617 (3S) -0.021 175 (1S)	-0.021 896	0.055 992
6	-0.014 964 455 4	-0.015 376 (3S) -0.014 562 (1S)	-0.014 969	0.030 360
7	-0.010 873 318 5	-0.011 129 (3S) -0.010 625 (1S)	-0.010 877	0.033 847
8	-0.008 137 989 6	-0.008 426 (3S) -0.008 093 (1S)	-0.008 2595	1.471 159
9	-0.005 469 545 4	-0.006 601 (3S) -0.006 369 (1S)	-	-
10	-0.002 094 663 3	-0.005 310 (3S) -0.005 143 (1S)	-	-

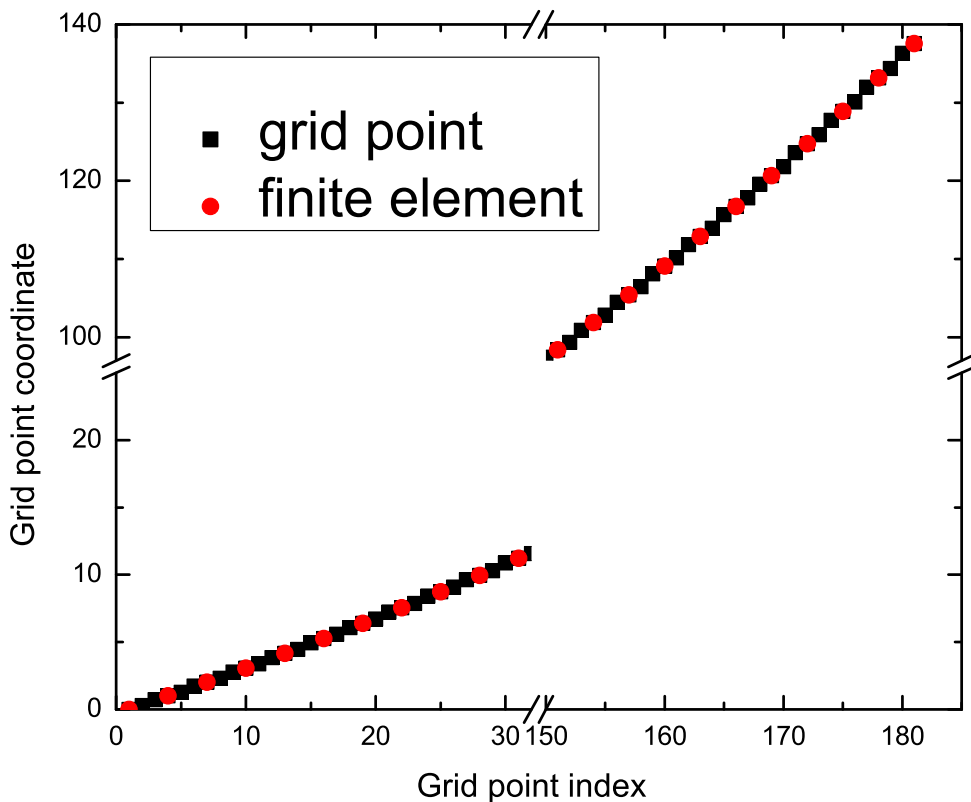


Figure 3.1: Numerical grid point mapping over the radial interval $[0,137.5]$ for the first and last 10 elements for $N_{gr} = 4$. The black squares are grid points, and the red solid circles indicate the finite-element mapping.

experimental values of $\text{He}(L = 0)$ energy levels. Because there are singlet and triplet states, but the SAE model has not corresponding singlet and triplet states, in column 3, we display the average of singlet and triplet energies for fixed principle quantum number n . In the last column, we calculate the percent error of average experimental value: $|E_{theory} - E_{ave}|/E_{ave}$.

For excited states, although the theoretical values are not very close to either single energy levels, or the triplet energy levels, these values are in good agreement with the average values of singlet and triplet energy levels. For principal quantum numbers $n < 8$, the error is much smaller than 1%. Even for n up to 8, the error is only about 1.5%.

When $n=9$, the current numerical energy value is $-0.005\,470$, closer to the 10th experimental energy level $[-0.005\,310(^3S), 0.005\,143(^1S)]$, rather than the 9th experimental energy levels $[-0.006\,601(^3S), 0.006\,369(^1S)]$. This means that the numerical result misses the real 9th and some higher energy levels of helium atom. In our investigation, these high n states (Rydberg states) can be neglected.

Chapter 4

Helium Photo-Double Ionization by XUV Pulses

In this chapter, few-XUV-photon DI will be discussed. In section 4.1, we discuss how to prepare an initial state, while in section 4.2 we present the selection of partial waves for our TDSE simulation. Next, in sections 4.3-4.5, we will discuss few-photon DI with up to three XUV photons. We use N_{XUV} to denote the number of XUV photons. $N_{\text{XUV}} = 1$ stands for single-photon DI, $N_{\text{XUV}} = 2$ stands for two-photon DI, and so on. In section 4.6, we will discuss the similarity and difference of few-photon DI with N_{XUV} up to 3.

In Fig. 4.1, we display a schematic representation of helium energy levels involved in the few-XUV-photon DI for a total excess energy of 11 eV. We present three different photon energies, and three different processes, respectively.

4.1 Preparing an Initial State

As in experiments, we need to prepare the initial atomic state for a numerical simulation. In this section, we discuss how to prepare the initial state for our simulations of helium atoms.

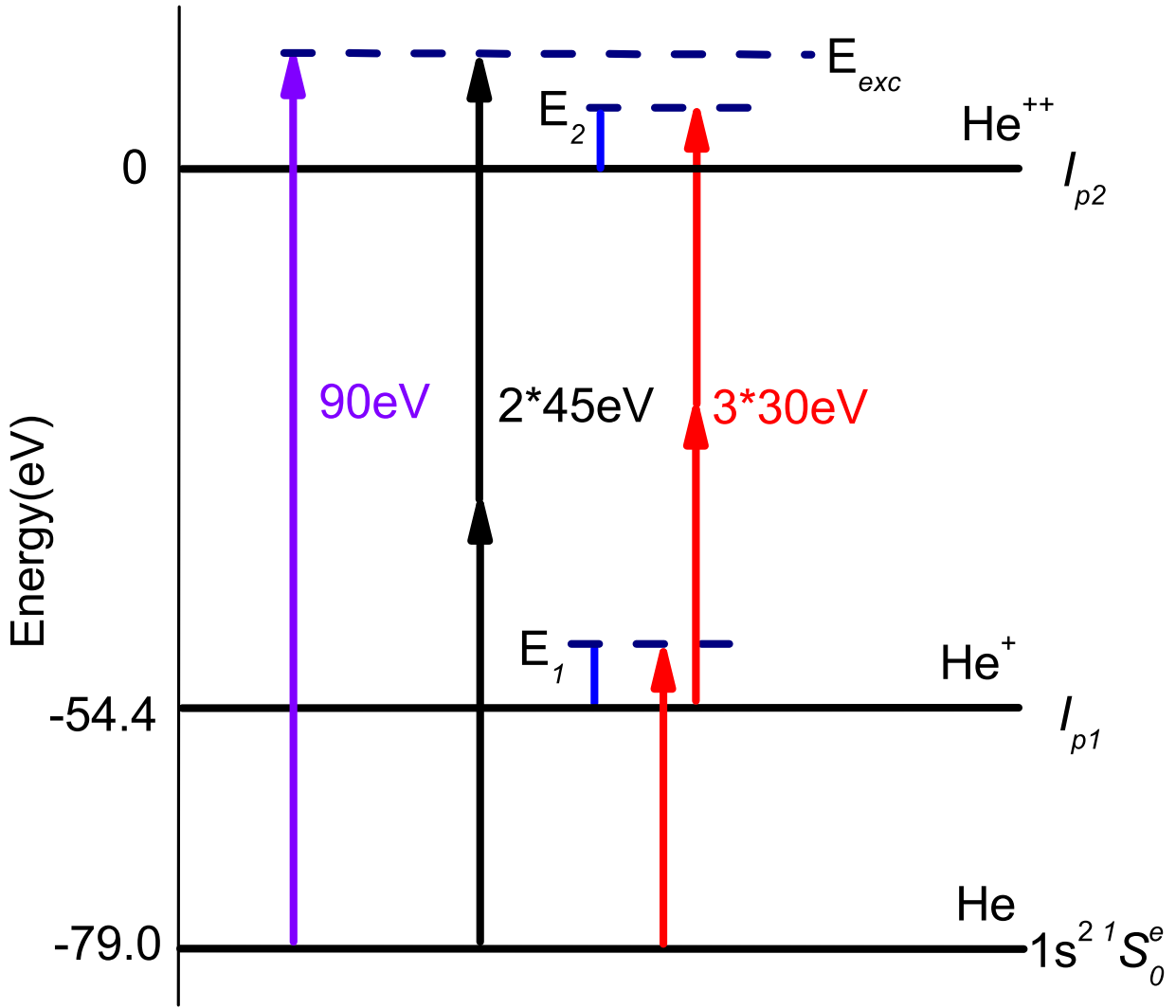


Figure 4.1: Schematic energetics for non-sequential double ionization of helium by two 45 eV or one 90 eV photon and sequential double ionization by three 30 eV photons. I_{p1} and I_{p2} designate the first and second ionization threshold, respectively. For the examples considered in this section, the combined excess energy of the emitted electrons is $E_{exc} = 11$ eV.

4.1.1 Ground State

In many cases, the initial state is also the ground state. The unperturbed ground state is one of the eigenstates of the field-free Hamiltonian

$$H_0 = -\frac{1}{2} \frac{\partial^2}{\partial r_1^2} - \frac{1}{2} \frac{\partial^2}{\partial r_2^2} - \frac{2}{r_1} - \frac{2}{r_2} + \frac{1}{|\mathbf{r}_1 - \mathbf{r}_2|}. \quad (4.1)$$

So, in principle, it can be obtained by diagonalizing the two-active-electron Hamiltonian matrix. Although the diagonalization is numerically easy to perform for a Hamiltonian matrix within the SAE model, it is difficult, even impossible, to perform simulations with very huge grids of the TAE Hamiltonian matrix on our current computational resources.

In fact, if we only need a few lowest states, the imaginary time propagation method is an economic way to obtain the initial states we need. In the imaginary time propagation method, the real time t in the TDSE is replaced by the imaginary time τ [46, 66]. Under the transformation $\tau = it$, the imaginary unit i is canceled by the i in the TDSE. Therefore the unitary of the Schrödinger equation is lost. This requires that we have to re-normalize the wave function at every couple of time steps in the imaginary propagation. Starting from an arbitrary trial state, after propagating a sufficient long time with small enough time step, the wave function will converge to the lowest state of a system controlled by a given potential.

For helium atoms in our case, like most studies by other groups [27, 33, 71, 119], we choose the singlet ground state as our initial state, which has total spin $S = 0$. The starting trial wave function for imaginary time propagation method is arbitrary, so we could start from a double Gaussian wave packet, which can be written as

$$\psi(r_1, r_2) = C e^{-(r_1-r_0)^2} e^{-(r_2-r_0)^2}, \quad (4.2)$$

where C is a normalization factor, r_0 is an arbitrary real number, which we set as 10 a.u. The size of the propagation time step is related to the accuracy and convergence of the ground energy and ground-state wave function. After many tests, 0.01 and 0.004 1 a.u.

are selected in our simulations. If we use the time step of 0.004 1 a.u., the convergence is very quick for the ground state. After ~ 0.5 fs of numerical propagation, the wave function converges to a relative energy change less than 10^{-8} per iteration.

4.1.2 Excited States

In Fig. 4.2, we display the probability densities of the radial wave functions for the (a) ground state and (b) first excited state with $L=0$. Both panels are plotted in a logarithm color/gray scale.

To obtain an excited state, we can also apply the imaginary time propagation method. For singly excited states, such as the $|1snSnS\rangle$ states, the process is very similar to the process of generating the ground state, except we subtract the overlap of the desired state with lower energy states every few propagation steps to force convergence into the higher-lying states.

For the case of doubly-excited states, the procedure is more complicated than for the ground state [14, 20, 97], since the doubly excited states are mixed with the singly ionized continuum states. The famous Fano profile describes the resonance between doubly excited states and singly ionized continuum states [16]. To obtain the doubly excited states, the idea is to transform the Hamiltonian Eqn. 4.1 to include absorption at the outer edge of each radial grid or make complex rotation [97]. The Hamiltonian Eqn. 2.36 becomes non-Hermitian, i.e., it has complex eigenvalues $E - i\Gamma/2$, where E is the energy eigenvalue and Γ is the width. When we diagonalize this non-Hermitian Hamiltonian, the states above the ionization threshold (the continuum with embedded resonances) split into two sets: the “bare” continuum and the resonance continuum states. The “bare” continuum states lie more or less on straight lines in the complex plane, and the resonance continuum states (such as doubly excited states) are shown as isolated points, whose real parts are energies E , while the imaginary parts are $\Gamma/2$ and related to the lifetimes ($\Gamma = 1/\tau$).

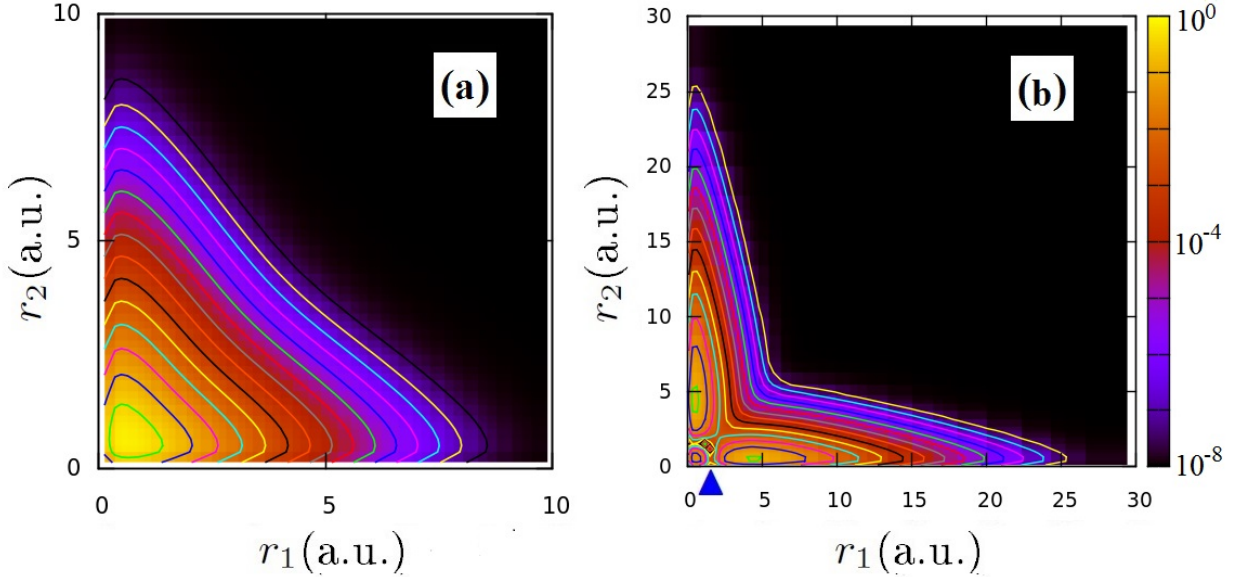


Figure 4.2: Probability densities of the radial wave function for the (a) 1^1S ($1s^2 1S_0^e$) ground state and (b) 2^1S first excited state of helium obtained by imaginary time propagation on a logarithm color/gray scale. The blue solid triangle in (b) indicates the node in the r_1 coordinate of the first excited state with $L=0$.

4.2 Selecting Partial Waves

As discussed in Chap. 2, we expand our wave function by partial waves [Eqn. (2.41)]. In principle, we need to include all partial waves to fully describe the physics. But this is impossible numerically because there are infinitely many partial waves in the Hilbert space. Depending on our real physical problem, we have to truncate the number of partial waves. We select partial waves by looking at the selection rules and convergence patterns for a particular process, if a partial wave does not contribute to the process, we will not include it.

4.2.1 Selection Rules and Symmetries

There are infinitely many partial waves, but our real physical process cannot actually reach all of them. We want to set some restrictions on the angular momenta. For example, if we consider single-photon DI, the total angular momentum can only change by 1. Therefore we

can restrict L to a very small scale, for instance, $L = 0$ and 1 , since $L=0$ in the initial state. In our actual calculation, due to the initial-state and intermediate-state interaction [119], we include $L = 0, 1, 2$, and 3 for single-photon DI. In Fig. 4.3, the initial-state correlation effect is displayed.

The restrictions for each momentum are

$$L \leq L_{\max}, \quad (4.3)$$

$$\max(l_1, l_2) \leq l_{>}^{\max}, \quad (4.4)$$

$$\min(l_1, l_2) \leq l_{<}^{\max}. \quad (4.5)$$

While L_{\max} gives the maximum value for the total angular momentum L , $l_{>}^{\max}$ gives the maximum value for the larger angular momentum of l_i ($i=1, 2$), and $l_{<}^{\max}$ gives the maximum value for the smaller momentum of l_i ($i=1, 2$). Mostly, we set $l_{>}^{\max} = l_{<}^{\max}$. Besides these restrictions, angular momenta need to satisfy the conditions [112, 113, 119]

$$|l_1 - l_2| \leq L \leq l_1 + l_2, \quad (4.6)$$

$$l_1 + l_2 - L = \text{even}. \quad (4.7)$$

The second condition Eqn. (4.7) is due to the fact that our initial state is a singlet state $S = 0$, and our linear polarized field does not change M .

In Tab. 4.1, we illustrate selecting and excluding the partial waves with the angular configuration $(L_{\max}, l_1^{\max}, l_2^{\max}) = (2, 3, 3)$. Any combination that does not satisfy the triangle relation Eqn. (4.6) is not listed in the table.

For SPDI and TPDI, after convergence testing [Appendix (C)] of the cross sections, energy, and angular distributions, the configuration $(L_{\max}, l_1^{\max}, l_2^{\max}) = (3, 3, 3)$ is sufficient. We have 23 partial waves in total for $(L_{\max}, l_1^{\max}, l_2^{\max}) = (3, 3, 3)$ [27, 46, 48]. When we increase the photon number to 3, we have to increase the number of partial waves [e.g., to $(L_{\max}, l_1^{\max}, l_2^{\max}) = (5, 5, 5)$ with 69 partial waves in most calculations in Chap. 6]. The convergence tests on L_{\max} and $l_{1,2}^{\max}$ are discussed in the Appendix (C).

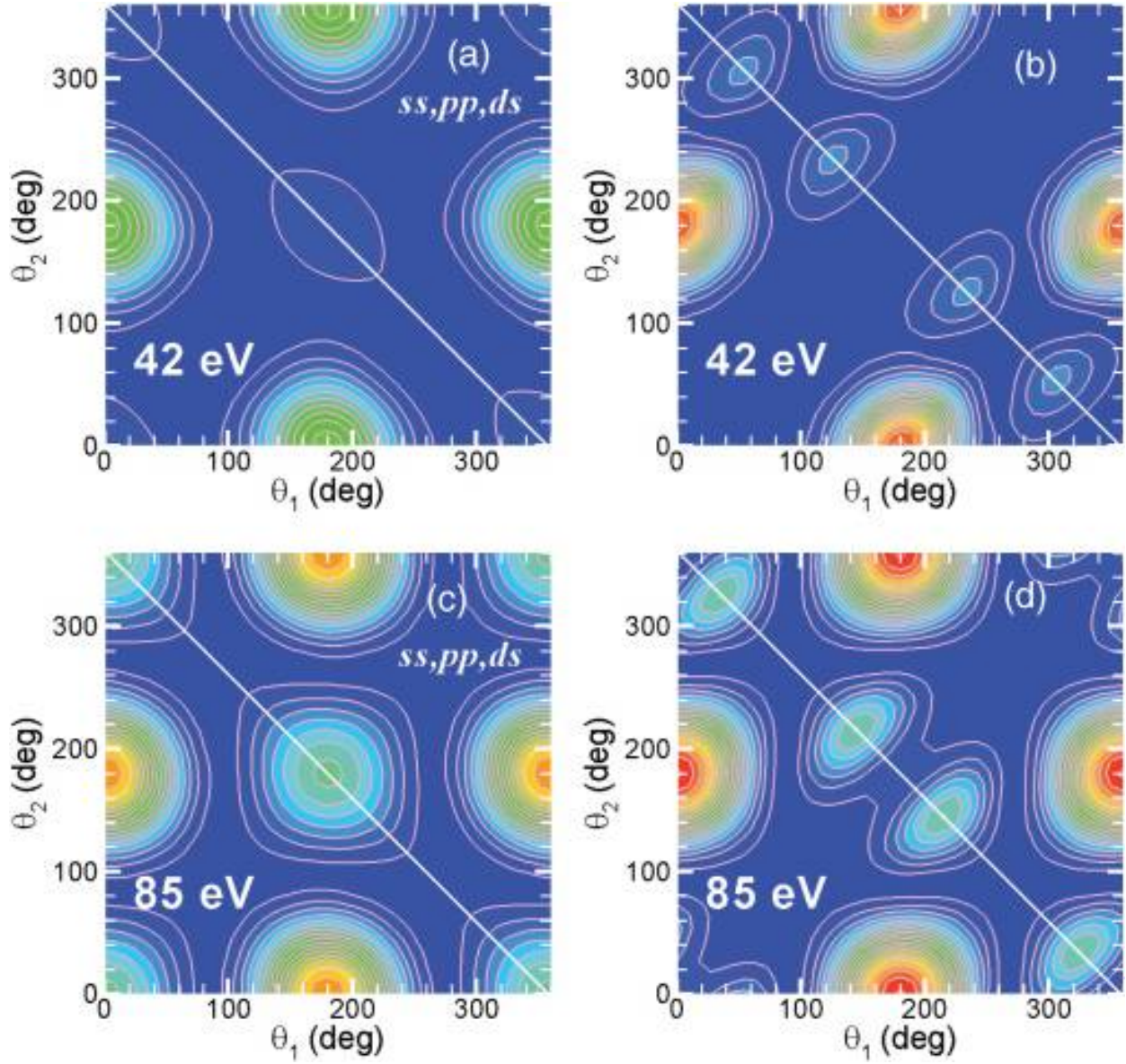


Figure 4.3: JAD for $\hbar\omega = 42$ eV [(a), (b)] and $\hbar\omega = 85$ eV [(c), (d)]. In (a) and (c), only the ss , pp , and ds final-state angular momentum components are included, while all angular momentum components [with restriction $(L_{\max}, l_1^{\max}, l_2^{\max}) = (2, 7, 7)$] are included in (b) and (d). Graphs were taken from Ref. [119].

Table 4.1: Selection of partial waves for the helium singlet states under the constraint $(L_{\max}, l_1^{\max}, l_2^{\max}) = (2, 3, 3)$.

No.	L	l_1	l_2	parity	index of partial wave	decision
1	0	0	0	e	1	✓
2	0	1	1	e	2	✓
3	0	2	2	e	3	✓
4	0	3	3	e	4	✓
5	1	0	1	o	5	✓
6	1	1	0	o	6	✓
7	1	1	1	e	-	parity forbidden
8	1	1	2	o	7	✓
9	1	2	1	o	8	✓
10	1	2	2	e	-	parity forbidden
11	1	2	3	o	9	✓
12	1	3	2	o	10	✓
13	1	3	3	e	-	parity forbidden
14	2	0	2	e	11	✓
15	2	2	0	e	12	✓
16	2	1	1	e	13	✓
17	2	1	2	o	-	parity forbidden
18	2	2	1	o	-	parity forbidden
19	2	1	3	o	14	✓
20	2	3	1	o	15	✓
21	2	2	2	e	16	✓
22	2	2	3	o	-	parity forbidden
23	2	3	2	o	-	parity forbidden
24	2	3	3	e	17	✓

4.3 Single-Photon Double Ionization

In this section, we will briefly discuss the main features of single-photon DI. Most of them can be found in the literature. We present the most relevant results to our discussion in the sections below.

All calculations in this section are carried out using a numerical grid with radial distances $0 \leq r_1 \leq r_1^{\max} = 277$ and $0 \leq r_2 \leq r_2^{\max} = 277$, including 151 FEs and 4 DVR basis functions in each FE, in combination with the Poisson-equation method (cf. Appendix C). This grid will be referred as “Grid 3” throughout this thesis, “Grid 1” consisting of 50 elements with 4 grid points in each FE and “Grid 2” containing 20 elements with 10 grid points in each FE are smaller grids used for numerical test in Appendix C. All joint energy and angular distributions in this section are evaluated by propagating the field-free TDSE for the time $\tau_{\max} = 40$ a.u. past the end of the XUV pulse. In agreement with Zhang *et al.* [119] we find this time scale to be long enough to yield converged distributions for SPDI and TPDI.

SPDI has been well established in the 1990’s [29, 38]. Its angular distribution includes two parts: a symmetrical part and an anti-symmetrical part. Both symmetrical and anti-symmetrical parts can be written as products of an angular factor and a correlation factor. The equal energy sharing result, demonstrating the selection rules [29, 54, 55], is a dipole structure distribution. The Wannier theory on DI gives the angular factor as $|\cos \theta_1 + \cos \theta_2|^2$, and electron correlation factor part [29]:

$$G(\pi - \theta_{12}) = e^{-4 \ln 2 \left[\frac{(\theta_{12} - \pi)^2}{(\theta_{1/2})^2} \right]}, \quad (4.8)$$

where θ_{12} is the absolute angular difference between two electrons and $\theta_{1/2}$ is a fitting parameter related to the correlation strength of two electrons. For unequal energy sharing, the anti-symmetry factor, which vanishes at equal energy, will increase. With increasing energy asymmetry, the anti-symmetric distribution $|\cos \theta_1 - \cos \theta_2|^2$ emerges on the JAD gradually, which manifests as the overlap of back-to-back emission and conic emission.

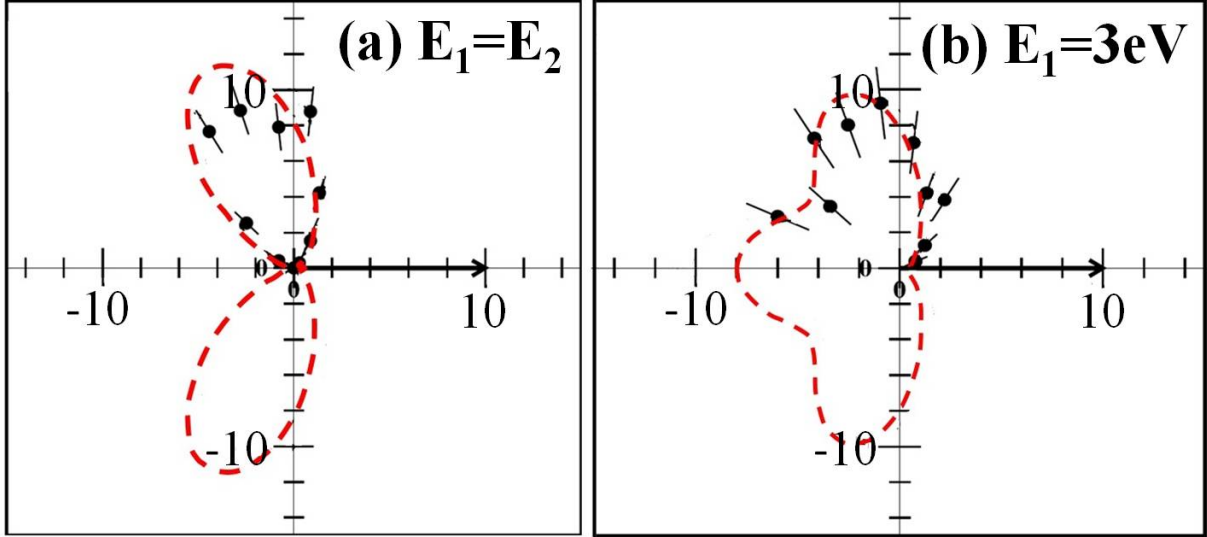


Figure 4.4: Absolute TDCS in $beV^{-1}sr^{-2}$ for a fixed angles ($\theta_1 = 0^\circ$) and different energy sharing. (a) Equal energy sharing $E_1 = E_2 = 10 eV$ at $\theta_1 = 0^\circ$, (b) unequal energy sharing $E_1 = 3 eV$ at $\theta_1 = 0^\circ$, $\varepsilon = 0.15$. The black dots with error bar are experimental results from [6]. The red dashed lines are our calculated results. The XUV photon energy is 99 eV.

4.3.1 Triple Differential Cross Sections

Figure 4.4 shows the TDCSs according to Eqn. 2.72 for $\hbar\omega_{XUV} = 99 eV$ and for emission of one electron along the XUV polarization direction at angle $\theta_1 = 0^\circ$ as a function of the other electron's emission angle θ_2 . Our calculated conditional TDCSs for co-planar emission are symmetrical about the XUV polarization direction and in good agreement with measured absolute conditional angular distributions [6, 93].

For equal energy sharing, $E_1 = E_2 = 10 eV$, the dominant angular difference between the two photoelectrons is $\Theta_{12} \approx 130^\circ$ [Fig. 4.4 (a)]. In compliance with the known selection rules for DI at equal energy sharing [8, 56], side-by-side and back-to-back emission are prohibited. We numerically verified that $\Theta_{12} \approx 130^\circ$ and that neither back-to-back nor side-by-side emission occur for arbitrary emission angles θ_1 , not just for the special case $\theta_1 = 0^\circ$. The dominant relative emission angle Θ_{12} thus characterizes the DI process regardless of any conditions imposed on θ_1 .

The conditional TDCS at fixed $\theta_1 = 0^\circ$ for non-equal energy sharing in Fig. 4.4 (b) reveals preferred angular differences Θ_{12} equal to $\approx 130^\circ$ and 180° . Due to the non-equal energy sharing which is mapped as the energy ratio

$$\varepsilon = \min\left\{\frac{E_1}{E_1 + E_2}, \frac{E_2}{E_1 + E_2}\right\} = 0.15, \quad (4.9)$$

with $E_1 = 3$ eV and $E_2 = 17$ eV, back-to-back emission occurs while side-by-side emission remains prohibited as for the case of equal energy sharing [8, 56]. The comparison of the conditional TDCSs at different energy sharings shown in Figs. 4.4 (a) and 4.4 (b) suggests the interpretation of Θ_{12} as a measure for the relevance of electronic correlation for DI, larger values of Θ_{12} indicating a more prominent role of electronic correlation.

In this comparison, we take the XUV energy to be the same 99 eV as in experiments [6, 93]. In Fig. 4.4, we display the absolute TDCS for different fixed angles and energy (sharing) for 99 eV XUV single-photon DI in both theory and experimental results. Figure 4.4(a) is for a fixed energy $E_1 = E_2 = 10$ eV, $\theta_1 = 0^\circ$. Figure 4.4(b) shows the TDCS for a fixed energy $E_1 = 3$ eV, $\theta_1 = 0^\circ$. Our present results are in good agreement with the experimental data [6].

In Fig. 4.4(a), for equal energies ($E_1 = E_2$), when electron 1 is fixed at 0° , the second electron is symmetrically distributed, and the dominant angular difference between two electrons is approximately 130° . For the other fixed emission angles of electron 1, as discussed in [46], when electron 1 is fixed at 60° , the second electron is asymmetrically distributed, and the dominant angular differences between the two electrons are also approximately 130° . We can define the dominant angular difference between two photoelectrons as Θ_{12} . It is the dominant difference of the emission angle of electron 1 and the emission angle of electron 2 at the peak(s) of the TDCS. Its mathematical definition is given in Eqn. (2.80). For arbitrary emission angles, back-to-back and side-by-side emissions always disappear, and the dominant angular difference between two photoelectrons Θ_{12} is always approximately 130° . This variable is related to the correlation strength, the larger the Θ_{12} , the stronger is the correlation during DI. Θ_{12} can thus be used to measure the electron correlation.

In Fig. 4.4(b), for fixed $\theta_1 = 0^\circ$, one electron takes the energy $E_1 = 3$ eV, the other electron takes $E_2 = 17$ eV. In this case, with the energy sharing of $\varepsilon = 0.15$, the TDCS displays three peaks. The angular difference has two peaks at 130° , as the equal energy sharing case, and one equal to 180° . The asymmetry in energy makes the back-to-back emission happen.

4.3.2 Joint and Mutual Angular Distributions

If we display TDCS in a contour plot as a function of angles (θ_1, θ_2) , we can have an overview of the angular distribution of both emitted photoelectrons. The TDCS is a function of energy (E_1) and angles (Ω_1, Ω_2) . In many cases, we interested in the energy ratio of E_1 and E_2 , rather than in a specific energy. Due to the indistinguishability of the two photoelectrons, the ionization probability of the electron pair with energies $(E_0, E_{\text{exc}} - E_0)$ is the same as the electron pair carrying energies $(E_{\text{exc}} - E_0, E_0)$, and they have the same energy ratio.

For very short pulses, the energy spectrum are very broad. When we fix E_1 at a given value, e.g., 5 eV, the energy for the second electron might vary in a broad range: from 5 eV to 20 eV. The distribution for $E_2 = 5$ eV is very different from the distribution for $E_2 = 25$ eV, but they are coherently added up to the TDCS and therefore cannot be distinguished. However if we compare the angular distribution at different energy ratios, these differences can be identified. The JAD [Eqn. (2.77)] is introduced for this purpose.

Joint Angular Distributions

Based on the DI probability distribution in Eqn. (2.68), the JAD in Eqn. (2.77) for DI in co-planar geometry as a function of the energy sharing ε between the emitted electrons and emission angles relative to the laser polarization can be rewritten as [119]

$$P(\theta_1, \theta_2; \varepsilon) = \sum_{i=1}^2 \int dk_1 dk_2 \frac{k_1^2 k_2^2}{2} \delta(\varepsilon - \frac{E_i}{E_1 + E_2}) P(\mathbf{k}_1, \mathbf{k}_2). \quad (4.10)$$

For equal energy sharing and sufficiently long XUV pulses, the TDCS Eqn. (2.72) is proportional to this JAD.

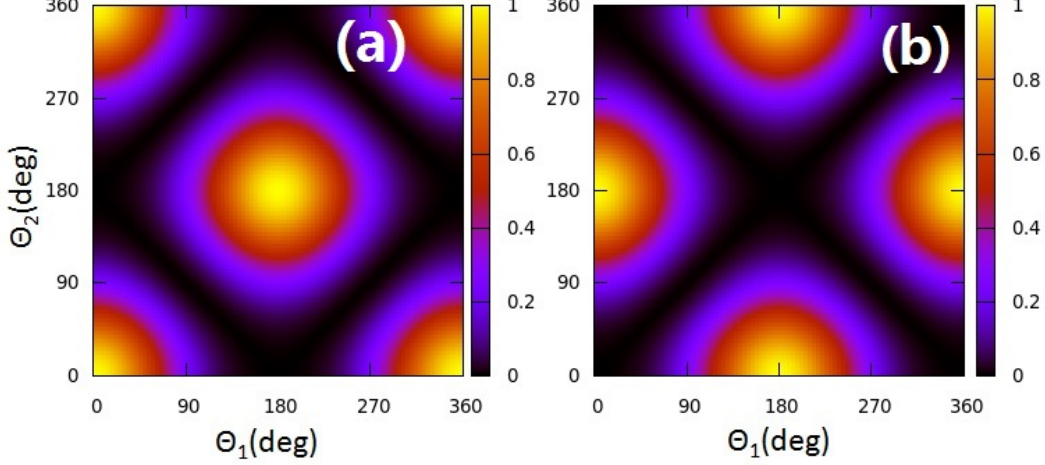


Figure 4.5: Demonstration of (a) symmetric and (b) anti-symmetric joint angular distributions: the angular factor.

Based on angular momentum algebra, Huetz *et al.* [3, 29] showed that the DI probability [c.f. Eqn. (2.68)] can be written as the square of the sum of two terms, where each term is the product of an angular factor and a complex-valued amplitude,

$$\begin{aligned}
 P(\mathbf{k}_1, \mathbf{k}_2) &\sim |A_g(E_1, E_2, \theta_{12})[\cos \theta_1 + \cos \theta_2] \\
 &\quad + A_u(E_1, E_2, \theta_{12})[\cos \theta_1 - \cos \theta_2]|^2.
 \end{aligned}
 \tag{4.11}$$

The amplitudes A_g and A_u are symmetric and antisymmetric under the exchange of E_1 and E_2 , respectively, and depend on the difference angle θ_{12} (Eqn. 2.78). These symmetric and antisymmetric distributions are shown in Fig. 4.5. The symmetric distribution is presented as an overlap of symmetric emission ($\theta_1 + \theta_2 = 360^\circ$) and side-by-side emission ($\theta_1 = \theta_2$). On the other hand, the antisymmetric distribution displays overlapping of back-to-back emission ($|\theta_1 - \theta_2| = 180^\circ$) and conic emission ($\theta_1 + \theta_2 = 360^\circ \pm 180^\circ$).

The coefficients A_g and A_u satisfy the permutation rules:

$$A_g(E_1, E_2) = A_g(E_2, E_1), \tag{4.12}$$

$$A_u(E_1, E_2) = -A_u(E_2, E_1). \tag{4.13}$$

From Eqn. (4.13), we know that, for the special case of equal energy sharing ($E_1 = E_2$), the

anti-symmetric term vanishes. Therefore the DI probability consists of a coherent sum of dipole distributions in θ_1 and θ_2 that is modified by the correlation factor $|A_g|^2$. Inspired by the Wannier theory for near-threshold DI, we write this factor as a Gaussian function with an angle-independent scaling factor $b(E)$ [17],

$$|A_g|^2 = b_g(E) \exp \left\{ -2 \ln 2 \left[\frac{\theta_{12} - \pi}{\theta_{1/2}} \right]^2 \right\}, \quad (4.14)$$

and

$$|A_u|^2 = b_u(E) \exp \left\{ -2 \ln 2 \left[\frac{\theta_{12} - \pi}{\theta_{1/2}} \right]^2 \right\}. \quad (4.15)$$

Then, adjusting a single parameter $\theta_{1/2}$ provides a good fit to measured angular distributions, even at the photon energies far beyond the near-threshold region [29]. The width of the angular distribution $\theta_{1/2}$ is a measure for the importance of electronic correlation, which shows an analogy to the dominant angle Θ_{12} identified in the TDCS discussed in the preceding subsection.

The symmetric amplitudes A_g are shown in Fig. 4.6, the symmetric amplitudes A_g is almost independent of the energy sharing, while the anti-symmetric amplitudes A_u increase with increasingly unequal energy sharing. Therefore, for increasingly unequal energy sharing, the anti-symmetric contribution in Eqn. (4.11) increases, allowing for back-to-back emission.

Figure 4.7 displays the combination of Fig. 4.5 and Fig. 4.6. The symmetric distribution in Fig. 4.7(a) now presents four peaks on the diagonal line. Both back-to-back emission and side-by-side emissions are not allowed. The anti-symmetric distribution shrinks the overlap between back-to-back emission and conic emission.

For equal energy sharing, due to the vanishing anti-symmetric distributions at $E_1 = E_2$, the JAD looks similar to Fig. 4.7 (a). For unequal energy sharing, the JAD has peaks from both Fig. 4.7 (a) and Fig. 4.7 (b). We next examine some calculated JADs for the helium DI by solving the TDSE.

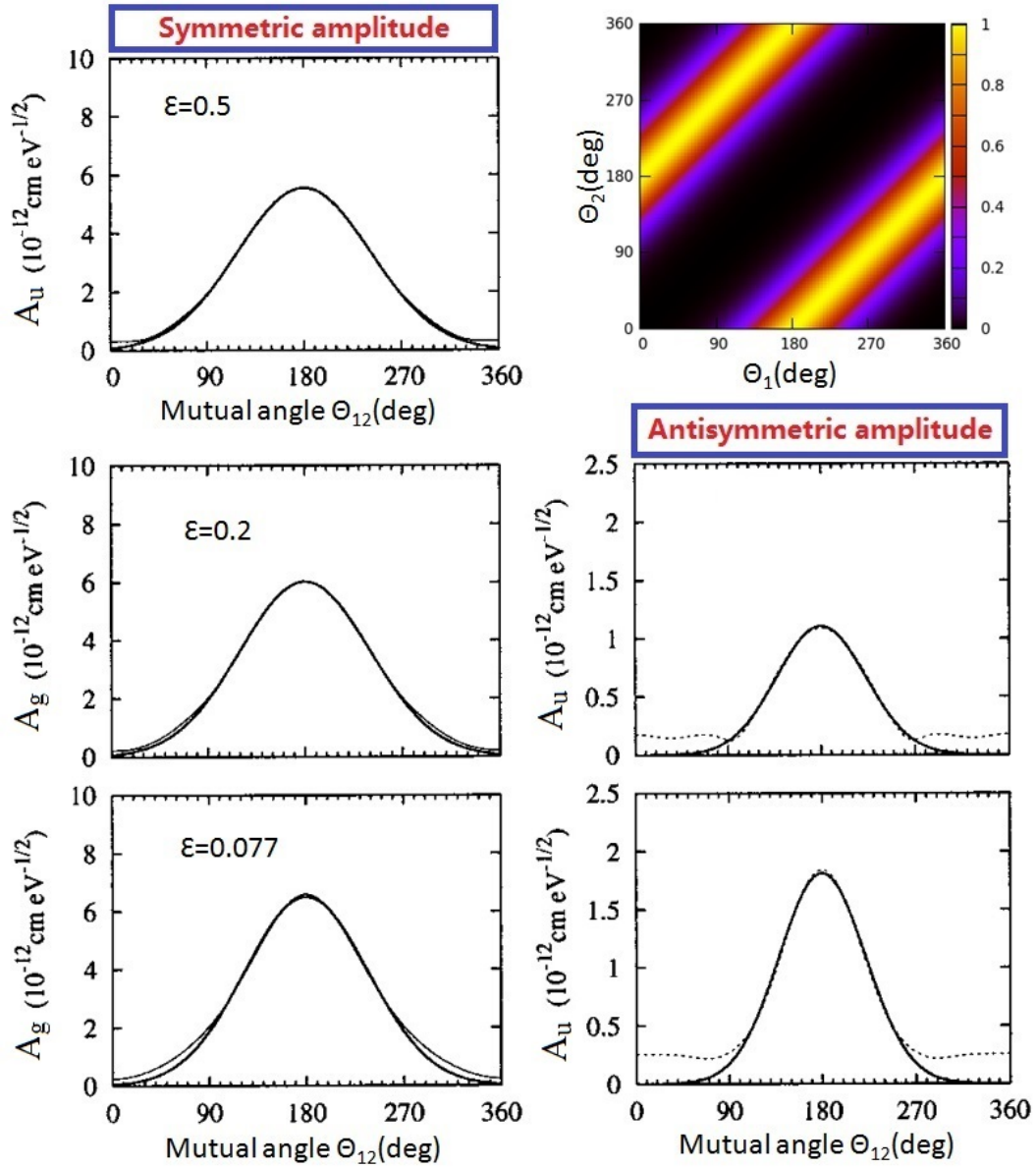


Figure 4.6: Symmetric and anti-symmetric amplitudes (figures were adapted from Ref. [39], except for the top-right panel).

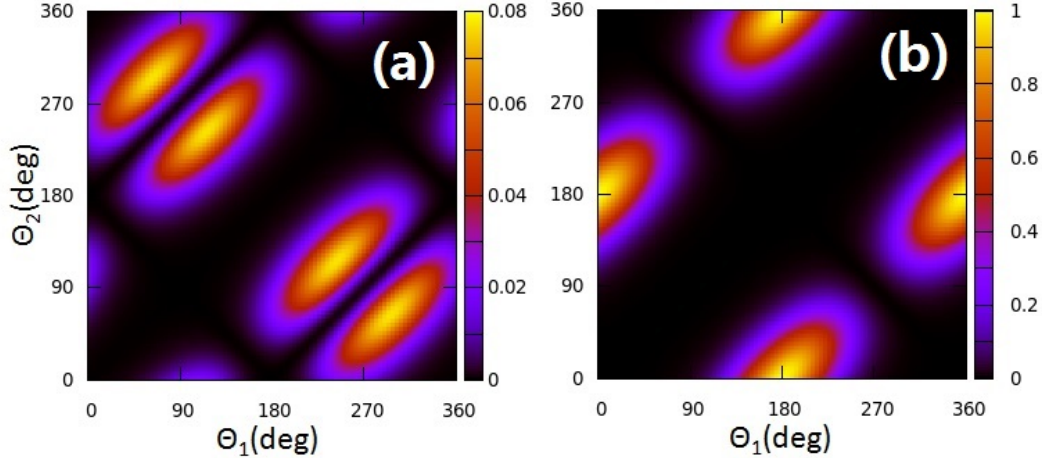


Figure 4.7: Symmetric (a) and anti-symmetric (b) joint angular distributions, in which the angular factors were multiplied by the amplitudes.

4.3.3 Angular Distributions

Equal Energy Sharing

Here we focus on XUV DI of helium at equal energy sharing where correlation effects are expected to be strongest. For equal energy sharing, the TDCS is proportional to the JAD with a constant factor [48]. We can compare the JAD with TDCS experimental results [6, 48]. Our calculated JAD at equal energy sharing is shown in Fig. 4.8 (a) for 90 eV photon energy. It is dominated by four peaks on the axis of $\theta_1 + \theta_2 = 360^\circ$ axis that corresponds to the symmetric emission (cf. Fig. 1.1). It excludes the back-to-back, conic, and side-by-side emissions, in agreement with the selection rules B2 and F discussed by Maulbetsch and Briggs [56] and Briggs and Schmidt [8]. The absence of back-to-back emission agrees with the selection rule B2 which challenges the intuitive expectation that strong electronic correlation during non-sequential DI enforces back-to-back emission. However, since this would violate parity conservation, emission occurs instead at an angle of 130° between the emission directions of the electrons, rather than 180° . Side-by-side emission is forbidden because of the electronic Coulomb repulsion, and is also excluded by the selection rule B2.

Figure 4.8 displays the calculated JAD and TDCSs for the helium DI. In Fig. 4.8(a),

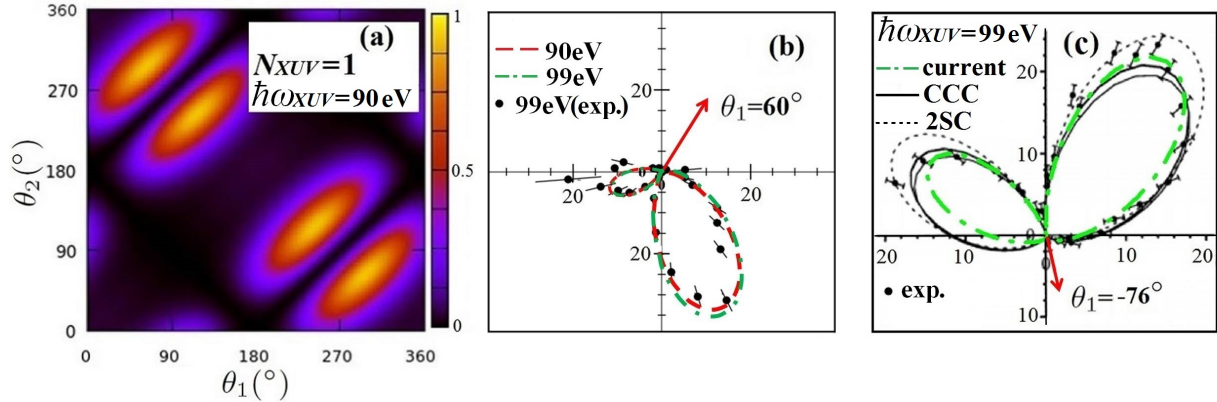


Figure 4.8: (a) Calculated normalized joint angular distribution for the double ionization of helium by one $\hbar\omega_{\text{XUV}} = 90$ eV XUV photon at equal energy sharing. The XUV pulse has a peak intensity of 10^{14} W/cm² and a pulse lengths of 1 fs. (b) Conditional angular distribution for $\theta_1 = 60^\circ$. The red dashed line shows the calculated angular distribution for $\hbar\omega_{\text{XUV}} = 90$ eV and is scaled by the factor 0.55 relative to the distribution calculated for $\hbar\omega_{\text{XUV}} = 99$ eV (green dash-dotted line). The black dots with error bars show the distribution measured by Bräuning *et al.* [6] for $\hbar\omega_{\text{XUV}} = 99$ eV in units of b eV⁻¹ sr⁻². Adapted from [6]. (c) Conditional angular distribution for $\theta_1 = -76^\circ$ and $\hbar\omega_{\text{XUV}} = 99$ eV. The green dashed-dotted line shows our result, while the solid black lines are the convergent close-coupling calculations for different gauges by Kheifets and Bray [38], and the black dotted line shows a calculation with screened final-state Coulomb wave functions by Pont and Shakeshaft [84]. The black dots with error bars show the measured relative cross sections of Schwarzkopf *et al.* [93]. Adapted from Ref. [38].

we present the calculated normalized joint angular distribution for the double ionization of helium by one $\hbar\omega_{\text{XUV}} = 90$ eV photon at equal energy sharing. Figure 4.8(b) compares our calculated conditional angular distributions for single-photon DI for XUV photon energies of 90 eV and 99 eV with the experimental data of Bräuning *et al.* [6], taken at 99 eV (20 eV excess energy). In this polar plot the emission direction of one electron is held fixed at $\theta_1 = 60^\circ$. For this figure only we added results for 99 eV in order to facilitate the comparison with the experimental data. The experimental distribution (black dots with error bars) is normalized to the absolute total DI cross section (8.76 kb) of Samson *et al.* [89]. Our calculated angular distributions for 90 eV and 99 eV are very similar; however, the magnitude of the calculated 90 eV distribution is scaled by the factor 0.55 relative to our calculated 99 eV distribution. Our 99 eV distribution is adjusted to the measured distribution at $\theta_2 = 330^\circ$ and agrees well with the experimental distribution.

A comparison of conditional angular distributions for $\theta_1 = -76^\circ$ and $\hbar\omega_{\text{XUV}} = 99$ eV is shown in Fig. 4.8(c). We adjusted our calculated angular distribution to the distribution measured by Schwarzkopf *et al.* [93] at $\theta_2 = 45^\circ$. The green dashed-dotted line shows our result, while the solid black lines are from the convergent close-coupling calculations (CCC) for different gauges by Kheifets and Bray [38], and the black dotted line shows a calculation with screened final-state Coulomb wave functions by Pont and Shakeshaft [84]. The three gauges used in the CCC calculations yield similar distributions, with almost indistinguishable results for the velocity and acceleration gauges.

Energy Sharing Dependencies

Figure 4.9 displays the energy sharing dependence of TDCSs of the helium SPDI. For $\theta_1 = 0^\circ$ and equal energy sharing with $E_1 = E_2 = 10$ eV, the dominant angular difference $|\theta_2 - \theta_1|$ between the two electrons is $\Theta_{12} \approx 130^\circ$ [Fig. 4.9 (a)]. In compliance with the known selection rules for DI at equal energy sharing [8, 56], side-by-side and back-to-back emissions are prohibited. This graph also shows good agreement between our calculations and the theoretical results of Huetz *et al.* [6, 29]

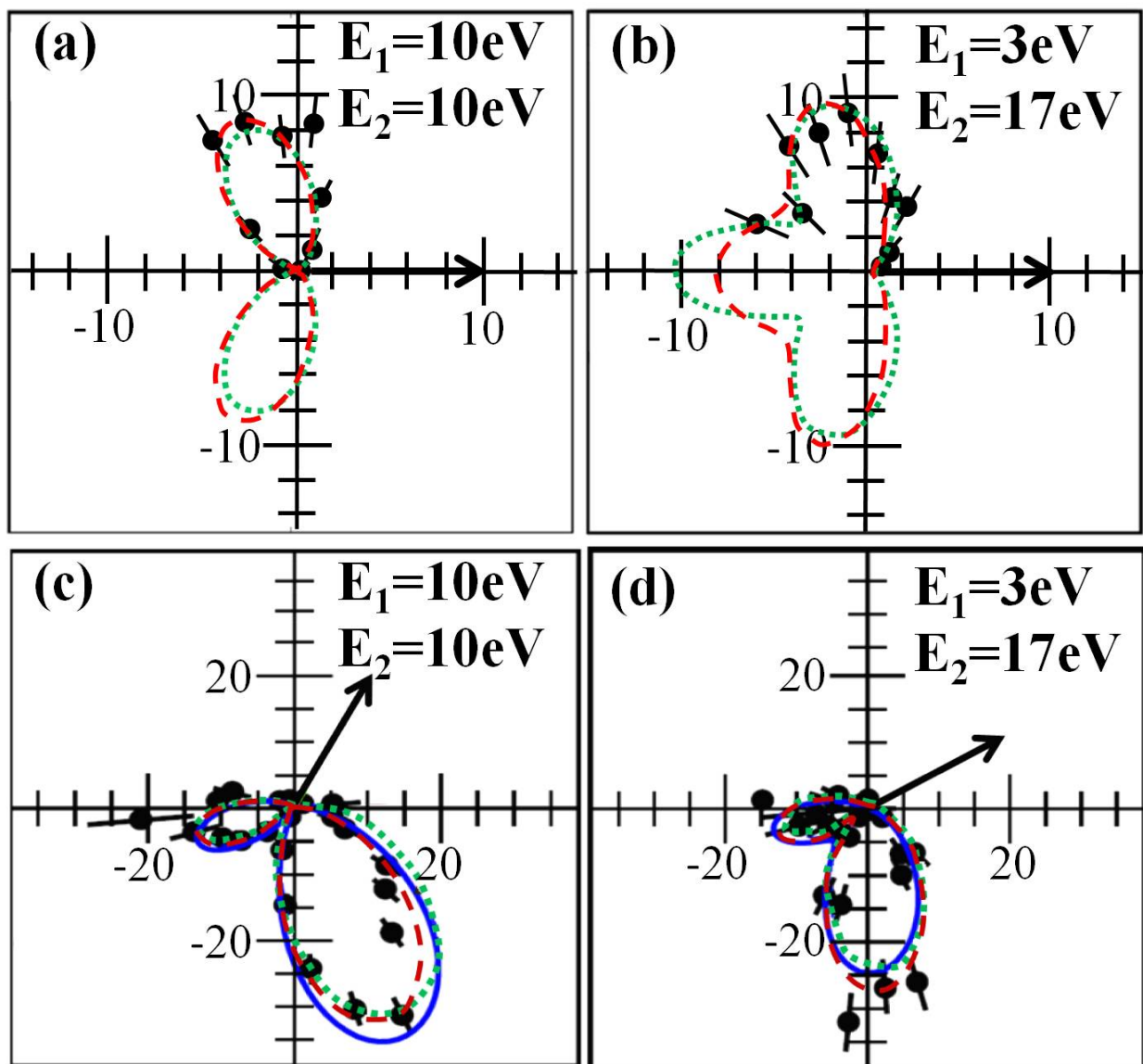


Figure 4.9: TDCSs in units of $beV^{-1}sr^{-2}$ for the double ionization of helium and fixed detection angles (a,b) $\theta_1 = 0^\circ$, (c) 60° , and (d) 30° , indicated by the black arrows. The central XUV-photon energy is 99 eV. The black dots with error bars are absolute experimental TDCSs from Ref. [6]. Our calculated results are shown as red dashed lines and normalized to the experimental data at (a) $\theta_2 = 110^\circ$, (b) 95° , (c) 295° , and (d) 275° . Panels (a,c): Equal energy sharing with $E_1 = E_2 = 10 eV$ ($\varepsilon = 0.5$). (b,d) Unequal energy sharing with $E_1 = 3 eV$ ($\varepsilon = 0.15$). The green dotted lines show theoretical results of (a) Huetz *et al.* [6, 29] Panels (b-d): Kheifets and Bray [6]. Panels (c,d): The solid blue lines show TDCC results of Palacios *et al.* [70].

The conditional TDCSs at fixed $\theta_1 = 0^\circ$ in Fig. 4.4 (b) for non-equal energy sharing with $E_1 = 3 \text{ eV}$ and $E_2 = 17 \text{ eV}$, corresponding to the energy-sharing parameter $\varepsilon = 0.15$, reveal preferred dominant angular differences Θ_{12} at $\approx 130^\circ$ and 180° . Back-to-back emission now occurs, while side-by-side emission remains prohibited as for the case of equal energy sharing [8, 56]. Here we also includes a comparison with the theoretical CCC results of Kheifets and Bray [6].

Figures 4.9 (c, d) compare the absolute measured TDCSs of Bräuning *et al.* [6] with the CCC results of Kheifets and Bray [6], TDCC calculations by Palacios *et al.* [70], and our calculations for equal [Fig. 4.9 (c)] and non-equal energy sharing with $\varepsilon = 0.15$ [Fig. 4.9 (d)] with fixed emission angles $\theta_1 = 60^\circ$ and 30° , respectively.

As for Figs. 4.9 (a, b), the dominant angular difference Θ_{12} in Figs. 4.9 (c, d) is about 130° . The comparison of the conditional TDCSs at different energy sharing shown in Figs. 4.9 (a-d) suggests the interpretation of Θ_{12} as a measure for the relevance of electronic correlation for DI, larger values of Θ_{12} indicating a more prominent role of electronic correlation. We numerically verified that $\Theta_{12} \approx 130^\circ$ for arbitrary emission angles θ_1 , not just for the special cases of $\theta_1 = 0^\circ$ and 60° . For the excess energy of 20 eV we consider in this section, our results for Θ_{12} agree with the theoretical prediction of Jiang *et al.* [37]. The dominant relative emission angle Θ_{12} thus characterizes the DI process regardless of any conditions imposed on θ_1 .

Figures 4.10 (a-c) show the calculated JADs for single-photon DI at a central XUV photon energy of 90 eV. All JADs in Figs. 4.10 (a-c) and 4.12 (a-d) are normalized to their maxima and their yields are plotted on a linear scale. Going from equal energy sharing in Fig. 4.10 (a) to unequal energy sharing with $\varepsilon = 0.1$ [Fig. 4.10 (b)] and extremely unequal energy sharing with $\varepsilon = 0.01$ [Fig. 4.10 (c)], symmetric emission remains dominant, while back-to-back emission is fading in to compete with symmetric emission for $\varepsilon = 0.01$, as suggested by Eqn. (4.14).

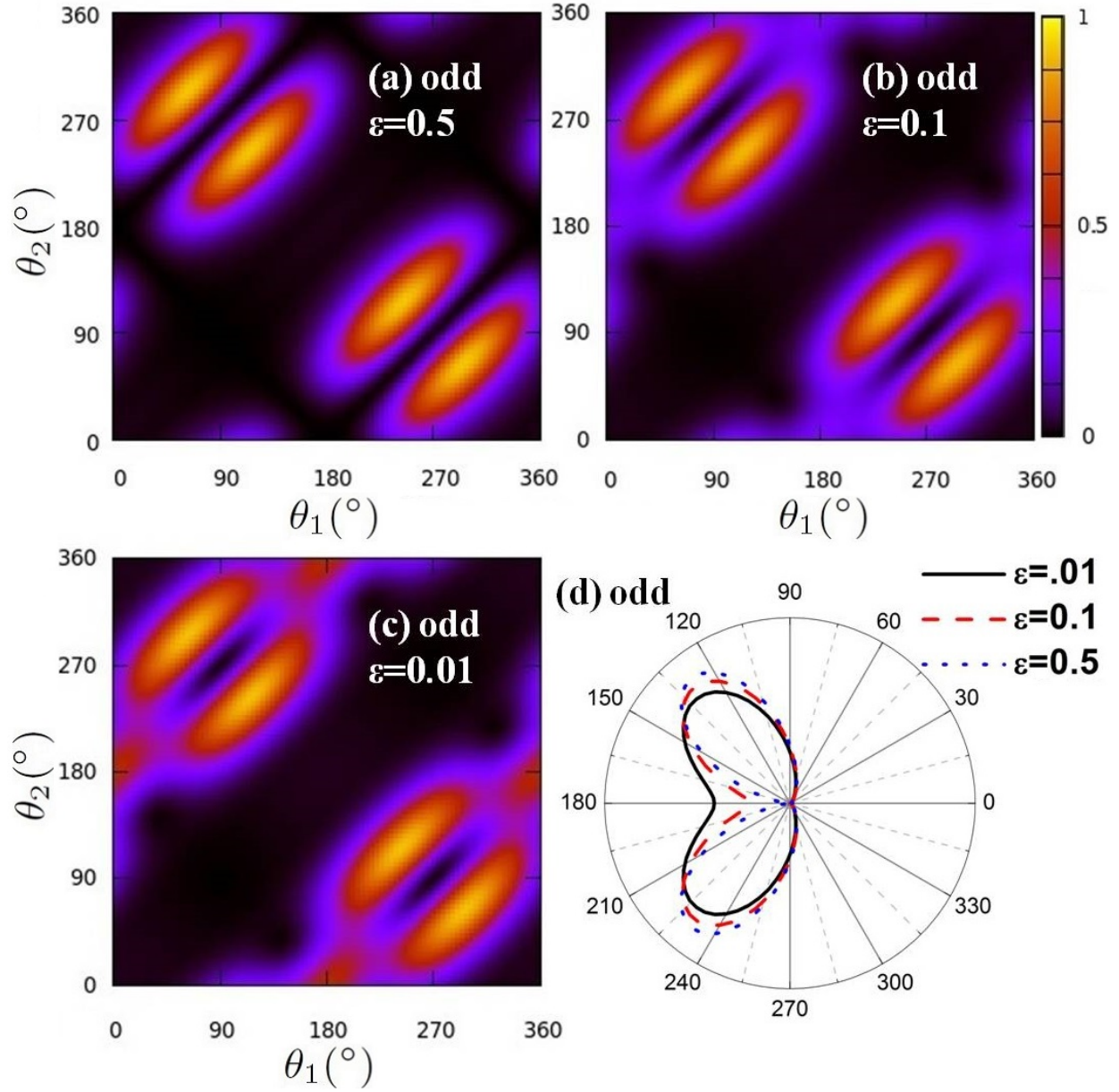


Figure 4.10: Calculated normalized joint angular distribution for the double ionization of helium by one $\hbar\omega_{\text{XUV}} = 90$ eV XUV photon at (a) equal energy sharing $\epsilon = 0.5$, (b) unequal energy sharing $\epsilon = 0.1$ and (c) extremely unequal energy sharing $\epsilon = 0.01$. Panel (d): Angular difference distributions extracted from (a-c). The XUV pulse has a peak intensity of 10^{14} W/cm^2 and pulse length of 1 fs.

4.4 Two-Photon Double Ionization

4.4.1 Momentum and Energy Distributions

In 2008, Guan, Bartschat, and Schneider first discussed in detail TPDI of helium by applying an *ab initio* non-perturbative time-dependent approach to the problem of a helium atom driven by an intense XUV laser pulse [27]. In 2011, Zhang *et al.* systematically discussed the JADs of TPDI in both non-sequential and sequential regimes. In this and the next subsections, we follow Guan's and Zhang's discussions, and briefly show the interesting properties of helium TPDI.

In Fig. 4.11, we display the energy distributions for TPDI with different photon energies, covering both sequential and non-sequential regimes (42 - 57 eV). The pulse durations are dependent on the photon energies, each pulse includes 10 optical cycles. At the lowest 42 eV photon energy, we see an essentially flat distribution of the momenta and, correspondingly, the energies of the two photoelectrons. With increasing photon energy, but still below the threshold for sequential ionization ($I_{p_2} = 54.4$ eV), the probability that one of the two electrons takes essentially all the excess energy while the other takes none is strongly increasing, i.e., asymmetric energy sharing begins to dominate. At 57.0 eV, on the other hand, we see a clear signature of the sequential ionization mechanism. The excess energy of 35.1 eV is likely distributed in the way that one of the electrons takes 33 eV, while the other takes 2.1 eV. This corresponds to using the first photon to kick out one electron with a final energy of 57.0 eV - 24.6 eV = 32.4 eV, and the second photon to ionize $\text{He}^+(1s)$, yielding a free electron of energy of 57.0 eV - 54.4 eV = 2.6 eV. Nevertheless, some probability for other scenarios (e.g., two step 2, known as TS2) remains [12, 27], indicating that the NSDI mechanism is still competing [27]. It is not clear yet how to identify the NSDI and SDI in TPDI with relative short XUV pulses. In section 5.1, we will discuss how to quantitatively measure the SDI contribution in TPDI by short XUV pulse.

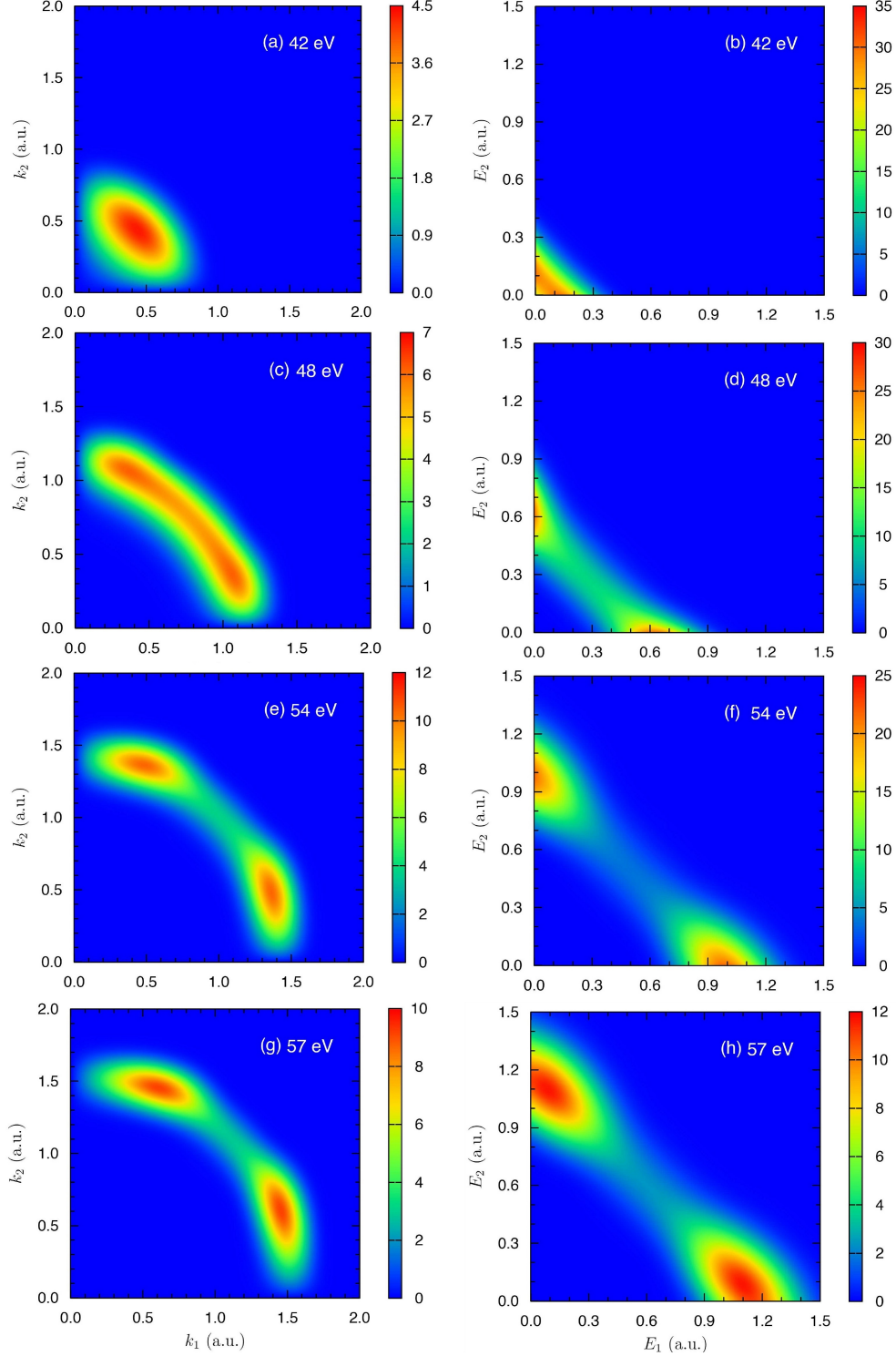


Figure 4.11: Momentum (left column) and energy (right column) distributions of the two escaping electrons. The laser pulse has a sine-squared envelope around the peak intensity of $5 \times 10^{14} \text{ W/cm}^2$ and a time duration of ten optical cycles. The central XUV photon energies are 42, 48, 54, and 57 eV, respectively. These graphs were adapted from our reference [27].

4.4.2 Angular Distributions

The angular distribution for TPDI is highly dependent on the photon energy. Although JADs for NSDI and SDI are similar at equal energy sharing, they are very different when the energy sharing varies from equal to unequal. The most important change is that the side-by-side emission emerges and becomes dominant. These variations of JADs were systematically studied by Zhang *et al.* in reference [119]. In this subsection, we will not repeat the discussion in Ref. [119], but mainly discuss two typical energies in non-sequential (42 eV) and sequential (70 eV) regimes, respectively.

Normalized calculated JADs for the helium DI by two $\hbar\omega_{\text{XUV}} = 42$ eV XUV photons are shown in Fig. 4.12 (a-c). The central XUV-photon energy and almost the entire spectral profile of the 1-fs XUV pulse are in the photon energy range for non-sequential DI, $39.5 \text{ eV} < \hbar\omega_{\text{XUV}} < 54.4 \text{ eV}$, excluding contributions due to sequential DI. After the absorption of two electrons, the final state of the three-particle system has even parity with the total angular momentum L being equal to either 0 or 2. In contrast to single-photon DI, where the odd final-state parity prohibits back-to-back emission, both equal and unequal energy sharing are subject to the same selection rules [54]. Back-to-back emission is now allowed for any energy sharing of the photoelectrons. As a result of the double electron-emission process depending on electronic correlation and the lack of censorship imposed by selection rules, unhindered electronic repulsion shapes the JADs. Accordingly, our JADs for equal energy sharing in Fig. 4.12 (a), unequal energy sharing with $\varepsilon = 0.3$ and 0.1 [Fig. 4.12(b,c)], and extremely unequal energy sharing with $\varepsilon = 0.01$ [Fig. 4.12 (d)] are insensitive to the energy sharing and dominated by back-to-back emission.

The striking robustness of the two-photon JAD against changes in energy sharing, implies that regardless of the value of ε the same “knock-out” (also known as two-step-1) mechanism [59] is operative. In this mechanism, the first electron absorbs two XUV photons and shares its energy with the second electron, leading to DI as a result of a binary electron-electron collision [41].

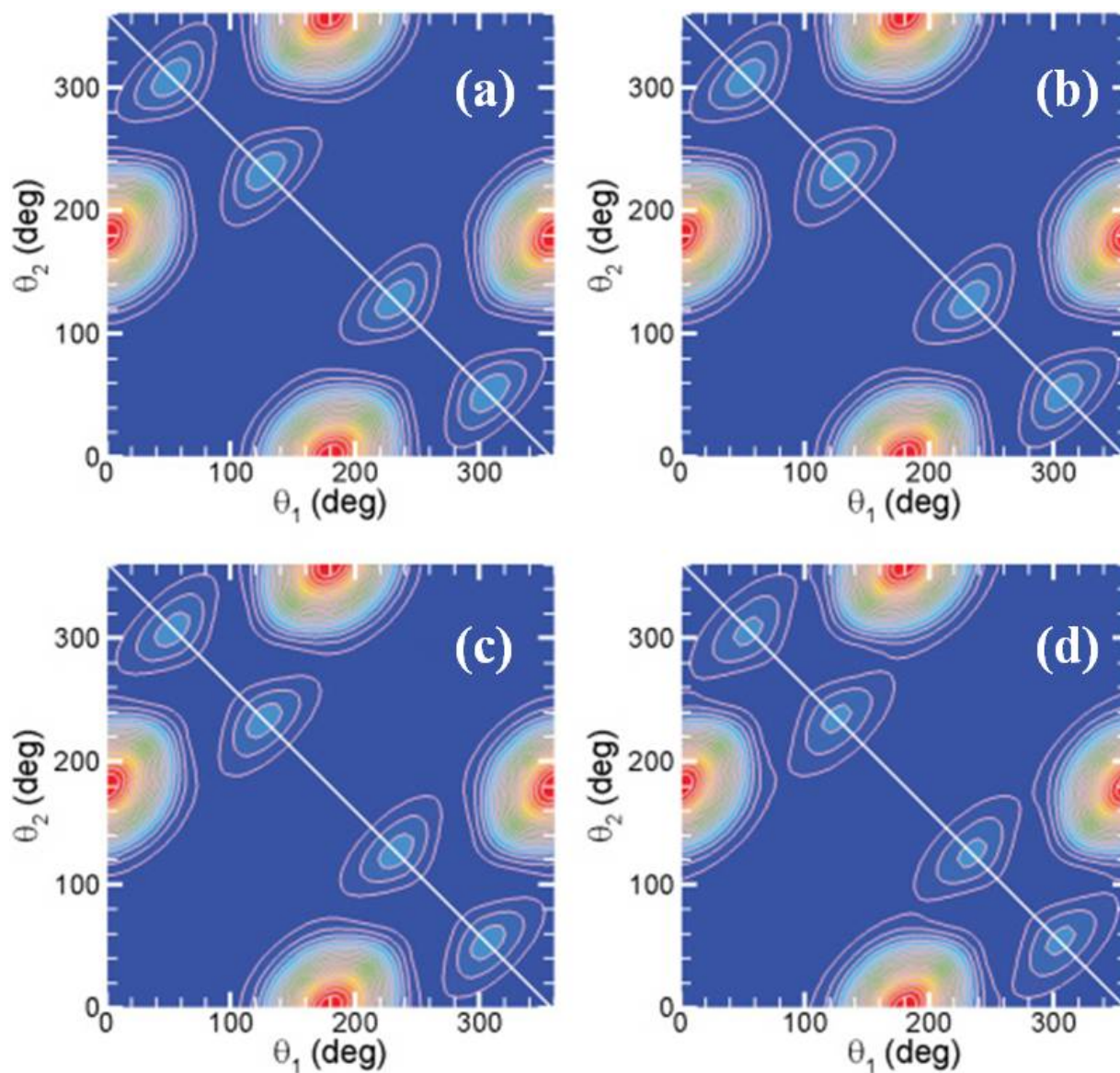


Figure 4.12: Calculated normalized angular distribution for the double ionization of helium by two $\hbar\omega_{\text{XUV}} = 42$ eV XUV photon for four different electron-energy sharing values: (a) $\varepsilon = 0.5$, (b) $\varepsilon = 0.3$, (c) $\varepsilon = 0.1$, and (d) $\varepsilon = 0.01$. These graphs were adapted from our reference [119].

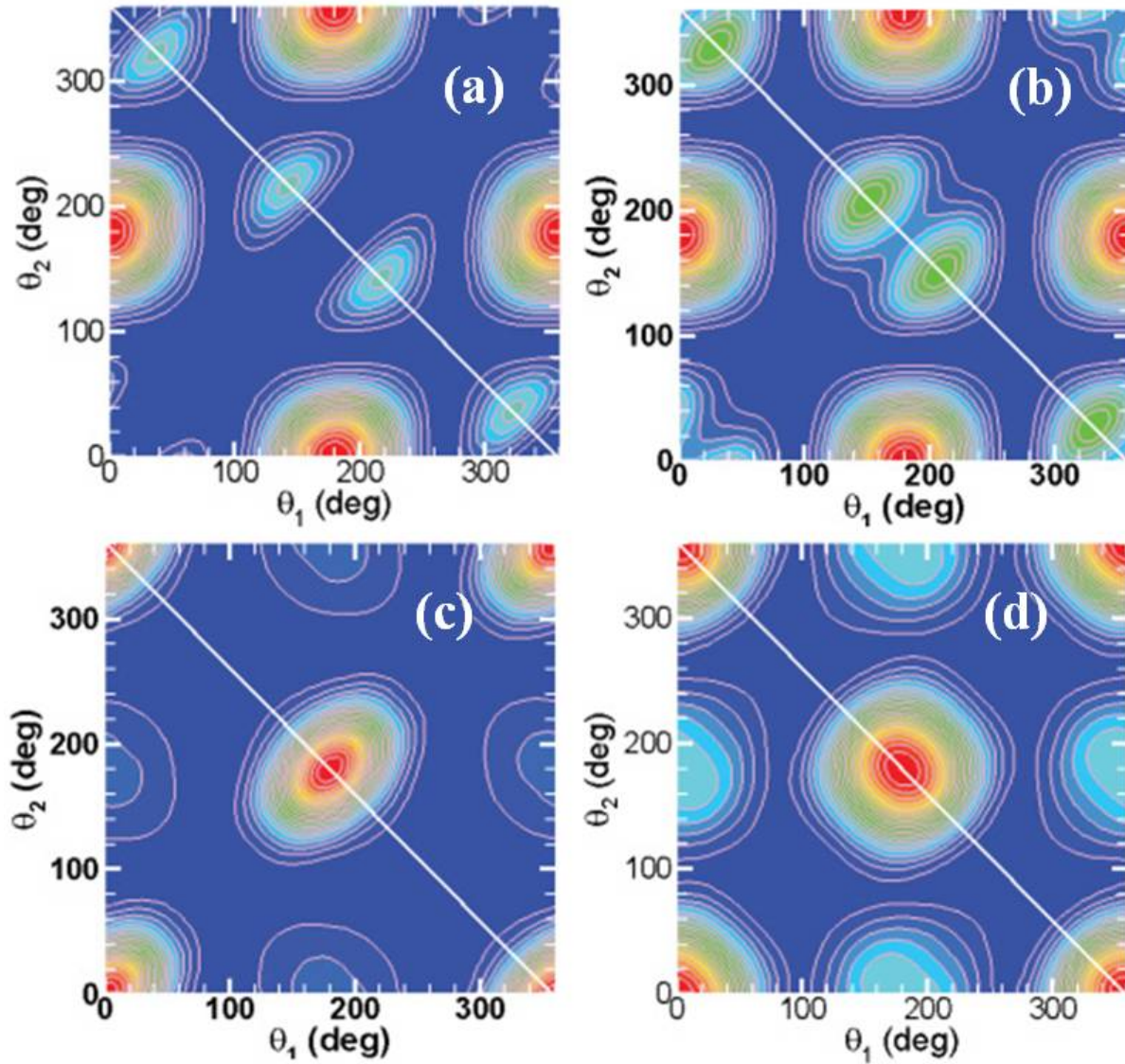


Figure 4.13: Calculated normalized angular distribution for the double ionization of helium by two $\hbar\omega_{\text{XUV}} = 70$ eV XUV photon for four different electron-energy sharing values: (a) $\varepsilon = 0.5$, (b) $\varepsilon = 0.3$, (c) $\varepsilon = 0.1$, and (d) $\varepsilon = 0.01$. These graphs were adapted from our reference [119].

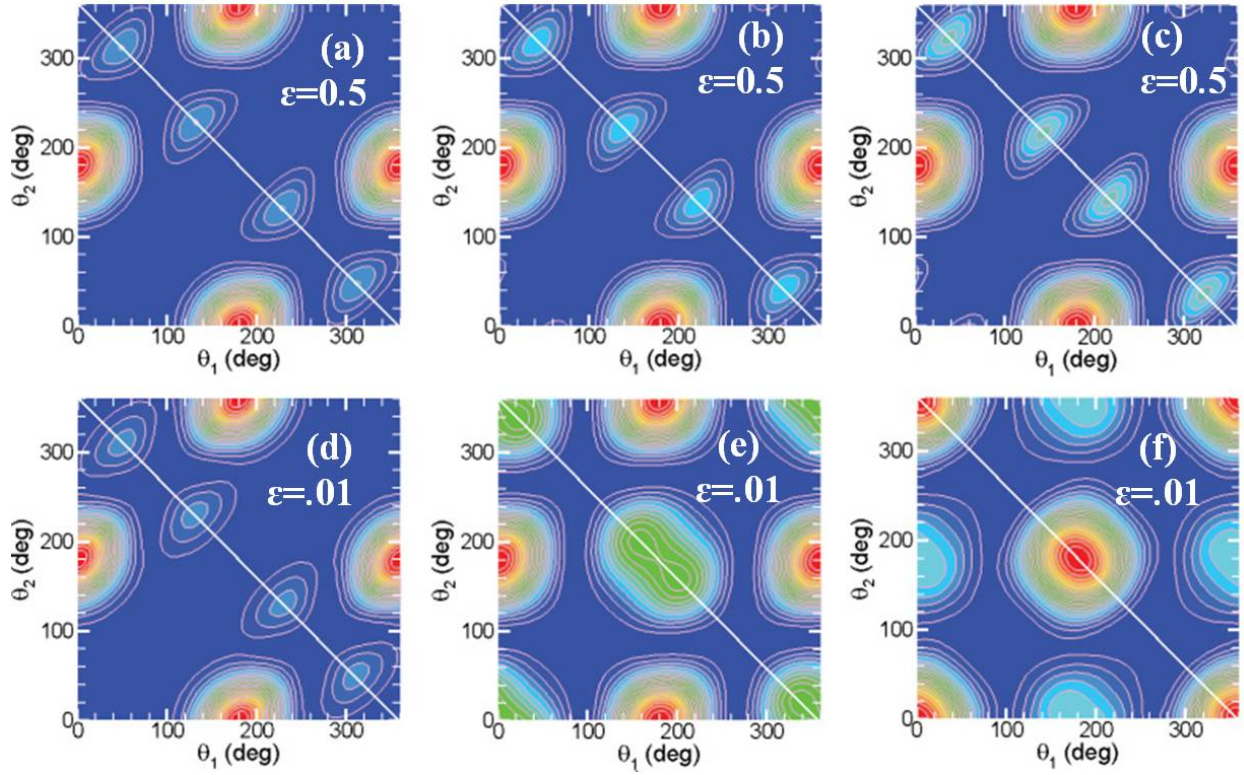


Figure 4.14: Calculated normalized angular distribution for TPDI of helium by two $\hbar\omega_{\text{XUV}} = 45$ eV (a,d), 54 eV (b,e) and 70 eV (c,f) XUV photon, respectively. The energy sharing for the top panel is equal ($\varepsilon = 0.5$), for the bottom panel it is extremely unequal ($\varepsilon = 0.01$). The XUV pulse has a peak intensity of $10^{14} \text{W}/\text{cm}^2$ and pulse length of 1 fs. These graphs were adapted from our reference [119].

While in the sequential regime, the normalized calculated JADs for the DI of helium by two $\hbar\omega_{\text{XUV}} = 70$ eV XUV photons are shown in Fig. 4.13. The central XUV-photon energy and entire spectral profile of the 1-fs XUV pulses are in the photon energy range for sequential DI, $\hbar\omega_{\text{XUV}} > 54.4$ eV, excluding contribution due to non-sequential DI within the non-sequential regime of spectrum. After the absorption of two electrons, as the non-sequential DI discussed above, the final state has even parity with the total angular momentum L being equal to either 0 or 2. In contrast to 42 eV TPDI, two bound electrons can be sequentially ionized by two photons. Side-by-side emission is now allowed for any unequal energy sharing of the photoelectrons. The double electron-emission process has little dependence on electronic correlation, and due to the lack of censorship imposed by selection rules instead, the unhindered final-state wave function shapes the JADs. For equal energy sharing, the electron-electron correlation still plays important roles, and the JAD is very similar to the 42 eV JAD in Fig. 4.12. When the energy sharing changes from equal to unequal, the JADs change significantly. Side-by-side emission increases slightly at $\varepsilon = 0.3$ and becomes dominant at $\varepsilon = 0.1$ and 0.01; back-to-back emission decreases from equal energy sharing to unequal energy sharing ($\varepsilon = 0.3$ ad 0.1), but becomes again prominent at extremely unequal energy sharing $\varepsilon = 0.01$.

In Fig. 4.14, we displays the JADs for two different energy sharing values ($\varepsilon = 0.5$ and 0.01) with three different XUV-photon energies: 45 eV, 54 eV and 70 eV. In the top panel, we notice that all three JADs are very similar. They are dominated by back-to-back emission and conic emission, and there are four minor peaks for symmetrical emission. It is also important to notice the gradual changes in each frame as the photon energy increases. The first change with increasing photon energy is that the distance between the centers of the first two minor peaks (counted from the left to the right) becomes larger. The second change is that the relative heights of the four minor peaks with respect to the four main peaks also become larger. These changes imply that, although electron correlation in the intermediate state is very important at equal energy sharing for any photon energy, the

degree of its importance decreases for larger photon energy. In particular, when the two electrons are ejected in the same hemisphere, the angle between them becomes increasingly smaller as the photon energy becomes larger. For example, the calculations show that the dominant angular difference between the two electrons emitted in the same hemisphere are about 84° and 74° , respectively, for photon energies of $\hbar\omega = 54$ and 70 eV.

For the unequal energy sharing, as shown in Fig. 4.14(d-f), the JADs change dramatically. In Fig. 4.14(d), the 45 eV JAD is very similar to the equal energy sharing JAD, because both JADs are shaped by strong electronic correlation when helium atoms are doubly ionized by 42 eV photons whose central photon energy belongs to the non-sequential regime. In Fig. 4.14(e), back-to-back emission remains dominant in 54 eV JAD, but the minor peaks for symmetrical emission are merging to side-by-side emission peaks. The 54 eV central energy XUV pulse with 1-fs pulse duration has a full-width at half-maximum (FWHM) in intensity of 6 eV. So actually the 54 eV 1-fs pulse covers both sequential and non-sequential regimes, which allows us to observe both sequential and non-sequential features. In Fig. 4.14(f), the 70 eV JAD shows dominant side-by-side emission, and weak back-to-back emission. For a pure SDI process, we are expecting the energy sharing $\varepsilon_{\text{SDI}} = (70-54.4)/(70 \times 2 - 79.01) \approx 0.26$. Because $\varepsilon = 0.01$ does not equal to this ε_{SDI} , electronic correlation also helps to shape the JAD. However, it is difficult to quantitatively describe the correlation for different energy sharing.

4.4.3 Total Cross Sections for One- and Two-XUV-Photon Coplanar Emission

We calculated the total cross sections $\sigma_{tot}^{N_{\text{XUV}}}$ for co-planar DI based on Eqn. (2.71) by integrating over the energies E_1 and E_2 of the emitted electrons, using Eqn. (11) of Ref. [119]. For DI induced by the absorption of a single 90 eV photon we find $\sigma_{tot}^1 = 7.40 \times 10^{-21}$ cm², in good agreement with the value of 7.53×10^{-21} cm² measured by Samson *et al.* [89]. For DI upon absorption of two 45 eV photons, we obtain $\sigma_{tot}^2 = 8.9 \times 10^{-53}$ cm⁴s, consistent with the cross section (8.5×10^{-53} cm⁴s) calculated by Guan *et al.* [27]

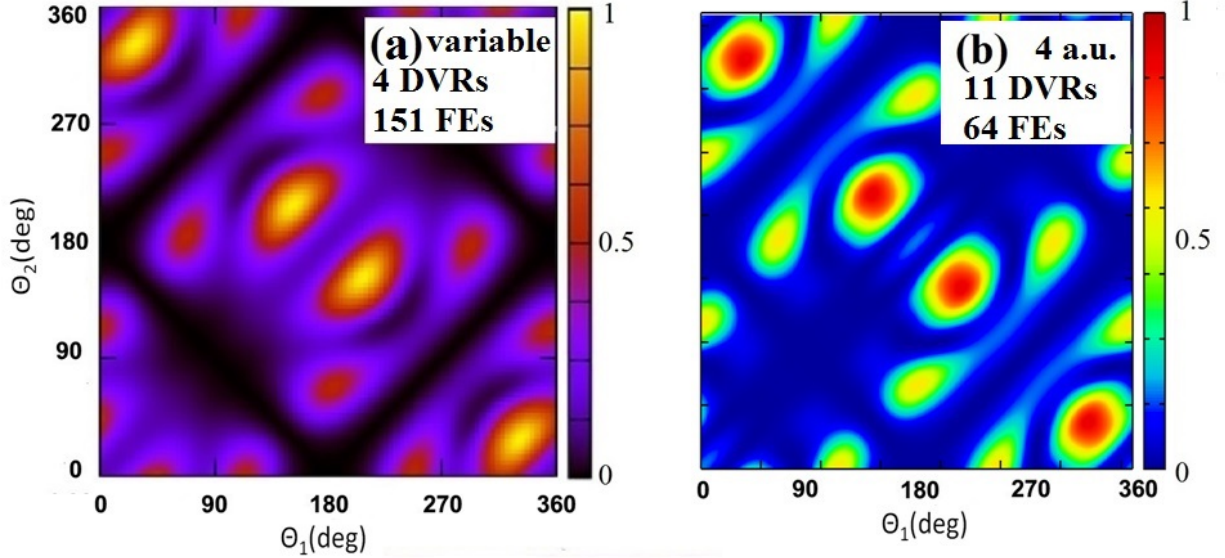


Figure 4.15: Calculated normalized joint angular distributions for the double ionization of helium by two $\hbar\omega_{\text{XUV}} = 30$ eV XUV photons with different FE-DVR parameters. (a) Used the Grid 3 defined in Sec. 4.3, the sizes of the FEs are non-uniform. (b) 64 FEs with 11 DVR functions in each FE. The FEs are 4 a.u. long [76].

4.5 Three-Photon Double Ionization

Obviously, SPDI belongs to NSDI. TPDI, depending on the central photon energy, can be either NSDI ($39.5 \text{ eV} < \hbar\omega_{\text{ctr}} < 54.4 \text{ eV}$) or SDI ($\hbar\omega_{\text{ctr}} > 79.01 \text{ eV}$). Three-photon DI processes can also be classified as NSDI and SDI. The NSDI regime for Three-photon DI of helium is very narrow: $26.3 \text{ eV} < \hbar\omega_{\text{ctr}} < 27.2 \text{ eV}$, but the spectral width of a 1-fs sine-squared pulse is 6 eV, therefore it is hard to observe the NSDI with three photons by 1-fs XUV pulse. We therefore discuss the SDI only in this section.

In Fig. 4.15(a,b), we present the equal-energy-sharing JAD for DI by three 30 eV photons with two different numerical parameter settings. Figure 4.15(a) shows the JAD obtained by using “Grid 3” (consisting 151 elements with 4 grid points in each FE) defined previously in Sec. 4.3, and Fig. 4.15(b) uses a uniform distribution of FEs with 11 DVR basis functions in each FE [75]. In both JADs for three-photon DI, besides the strong symmetrical emission, we observe two extra minor peaks around each symmetrical main peak.

The JAD for DI by three 30 eV photons in Fig. 4.15 is similar to the single-photon JAD in Fig. 4.8 in the sense that the same forbidden emission patterns are present. In either case, back-to-back, conic, and side-by-side emission are prohibited, as mandated by selection rules [56]. For one- and three-photon DI the JADs contain the same dominant nodal lines.

We calculated the three-photon JAD by propagating for the time $\tau_{\max} = 100$ a.u. past the end of XUV pulse in order to minimize unphysical side-by-side emission. For this propagation time, the contribution from side-by-side emission relative to the total DI yield for three-photon DI, integrated over a 10° -wide stripe (5° on each side) and centered about $\theta_1 = \theta_2$, is below 1.3%. Variation of τ_{\max} , i.e., of the total propagation time, allows us to disentangle effects that tend to influence the JAD in opposite ways (not shown). Since three-photon DI is (predominantly) sequential in nature, electronic correlation is not required to efficiently liberate both electrons. The photoelectrons thus tend to individually follow the electric force they experience in the linearly polarized XUV pulse. Furthermore, since back-to-back emission would violate parity conservation they initially tend to move in the same direction along the polarization. However, for equal energy sharing the effect of electron repulsion accumulates as time goes on and prevents the detection of side-by-side emission. As electron repulsion becomes increasingly influential, the initial “side-by-side electronic density” is pushed away from the $\theta_1 = \theta_2$ line and merges with the nearby peaks on the symmetric-emission line ($\theta_2 = 360^\circ - \theta_1$) in Fig. 4.18(b) (cf. the disappearance of the side-by-side contribution in Fig. C.2 for increasing τ_{\max}).

4.6 Comparison of Helium XUV Double Ionization by One, Two, and Three Photons

In previous sections, we have discussed the general features of helium few-photon DI in an XUV pulse separately. We have noticed that for all three processes, symmetrical emission is presented, but it is relatively weak in TPDI compared to SPDI and three-photon DI. At equal energy sharing, back-to-back emission is only allowed in TPDI, but forbidden in both

SPDI and three-photon DI. In this section, we compare these three processes, assuming the two photoelectrons carry the same total excess energy.

For all numerical results in this subsection (Chap. 4.6) we used the angular momentum limits $(L_{\max}, l_1^{\max}, l_2^{\max}) = (3, 3, 3)$ for one-photon DI and two-photon DI and $(L_{\max}, l_1^{\max}, l_2^{\max}) = (5, 5, 5)$ for three-photon DI in the expansion of wave function [Eqn. (2.40)], unless specified otherwise.

4.6.1 Few-photon Double Ionization in a Single XUV Pulse

Depending on the number of XUV photons involved, N_{XUV} , and photon energy, $\hbar\omega_{\text{XUV}}$, DI of helium in intense XUV pulses proceeds either sequentially or non-sequentially. In this section we discuss joint energy and angular distributions of the emitted electrons for DI of helium induced by the absorption of either one 90 eV, two 45 eV, or three 30 eV photons. For all three cases the total energy transferred to the atom is 90 eV (cf. Fig. 4.1), and the electrons leave the atom with a combined excess energy of $E_{\text{exc}} = 90 \text{ eV} - I_{p_1} - I_{p_2} = E_1 + E_2 \approx 11 \text{ eV}$. While DI is predominantly sequential for the absorption of three 30 eV photons, the absorption of two 45 eV or one 90 eV photon can only proceed through non-sequential DI.

Different from many-photon DI of helium in a strong laser field [86, 111], the angular distribution of photoelectrons is highly dependent on the photon number of absorbed [46]. For single-photon and three-photon DI, both back-to-back and side-by-side emission are not allowed or weak, which is not true for many-photon DI [86, 111], while for two-photon DI, back-to-back emission is dominant [27, 46, 119].

4.6.2 Energy Distributions

Figure 4.16 shows joint photoelectron energy distributions for the DI of helium by one, two, and three photons, with photon energies $\hbar\omega_{\text{XUV}} = 90, 45, \text{ and } 30 \text{ eV}$, respectively. The photon energies in each case are the central energy in the spectrum of an XUV pulse with peak intensity $I_0 = 10^{14} \text{ W/cm}^2$ and a pulse duration of 0.364 fs (FWHM in intensity),

corresponding to the spectral width (FWHM in spectral intensity) $\hbar\Delta\omega_{\text{XUV}}=6$ eV.

As expected, the energy distributions in Figs. 4.16(a-c) show dominant DI yields at 11 eV excess energy. Corresponding normalized DI yields, integrated over the XUV-pulse spectral profile,

$$P(\varepsilon) = \int_0^\infty dE_1 P(E_1, \frac{1-\varepsilon}{\varepsilon}E_1), \quad (4.16)$$

are given in Fig. 4.16(d) as a function of the energy sharing parameter ε [cf. Eqn. (2.71)]. For the spectrally broad sub-fs XUV pulses considered in this work and for non-sequential DI by one and two photons, the DI yields are distributed over a broad range of energy sharings with $E_{\text{exc}} \approx 11$ eV. For non-sequential DI by a single 90 eV photon, the DI yield is almost independent of the energy sharing between the photoelectrons [Figs. 4.16(a,d)]. This fact is well-established in the literature, both theoretically and experimentally. It was discussed in Ref. [11, 71, 119] for a slightly higher XUV photon energy of 99 eV. Non-sequential DI by two 45 eV photons slightly favors asymmetric energy sharing [Figs. 4.16(b,d)]. Our joint energy distributions in Fig. 4.16(b) qualitatively resemble, but are less asymmetrical than the distributions calculated by Guan *et al.* [27] for a slightly higher photon energy (48 eV).

In contrast, sequential DI by three 30 eV photons operates by one-photon absorption of the first electron with kinetic energy $E_1 \approx \hbar\omega_{\text{XUV}} - I_{p_1} = 5.4$ eV, followed by two-photon absorption of the second electron, leading to the energy release $E_2 \approx 2 \hbar\omega_{\text{XUV}} - I_{p_2} = 5.6$ eV. Accordingly, the largest yield in Fig. 4.16(c) occurs near $E_1 \approx E_2 = 5.5$ eV. The small energy difference of $E_2 - E_1 = 0.2$ eV is much less than the FWHM $= \hbar\Delta\omega_{\text{XUV}} \approx 6$ eV, and thus cannot be resolved in this graph within the spectral width of the XUV pulse.

4.6.3 Angular Distributions

Figure 4.17 displays the calculated JADs for these three different DI processes. The calculated JAD in Fig. 4.17(a) is dominated by four peaks on the $\theta_1 + \theta_2 = 360^\circ$ axis that correspond to symmetric emission (cf. Fig. 1.1). It excludes back-to-back, conic, and side-by-side emissions, which is in agreement with the selection rules B2 and F discussed by Maulbetsch and

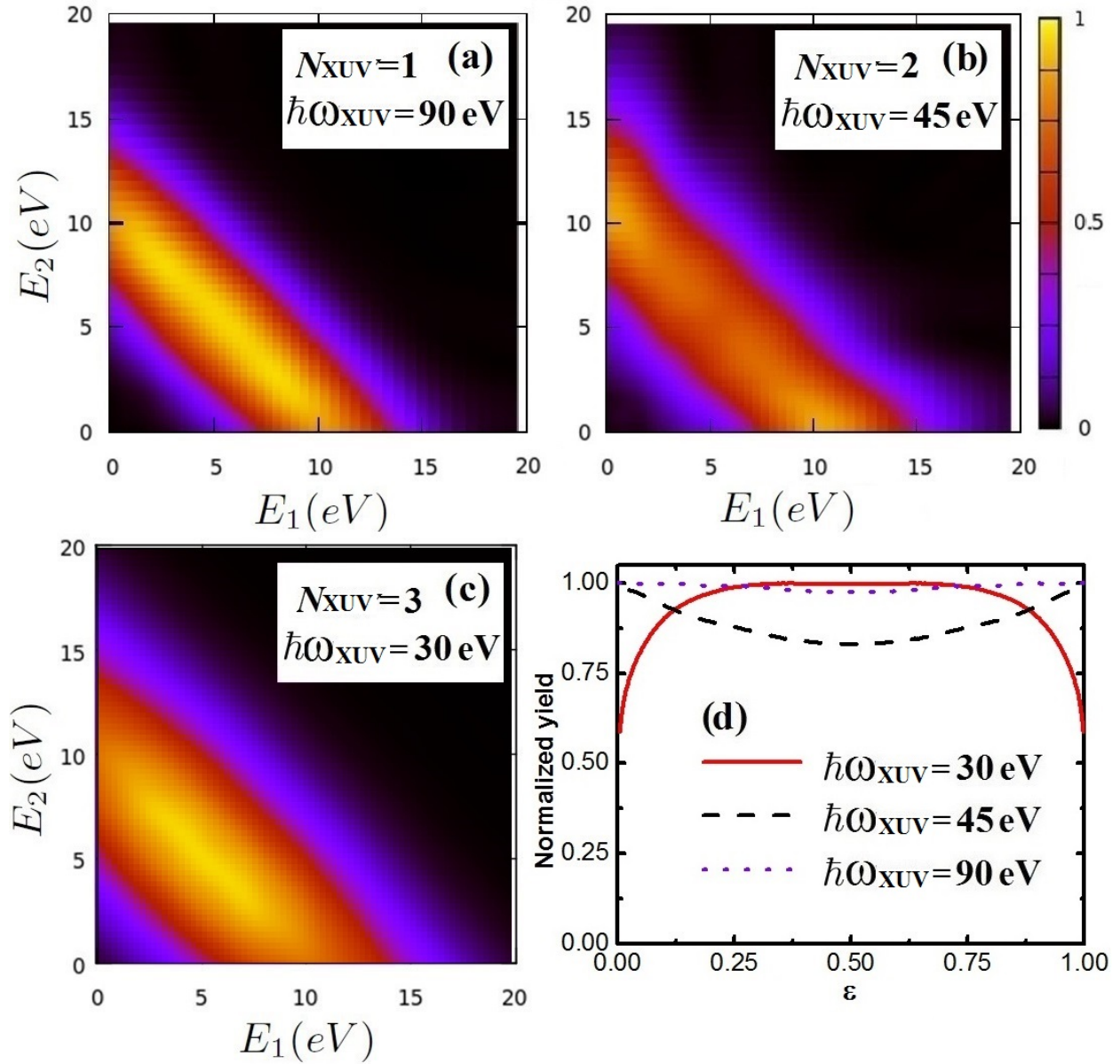


Figure 4.16: Normalized joint photoelectron energy distributions for the double ionization of helium by (a) one 90 eV, (b) two 45 eV, and (c) three 30 eV photons of a 10^{14} W/cm² peak intensity 1-fs long XUV pulse. (d) Corresponding normalized double-ionization yields, integrated over the XUV-pulse spectral profile, as a function of the energy sharing ϵ between the photoelectrons.

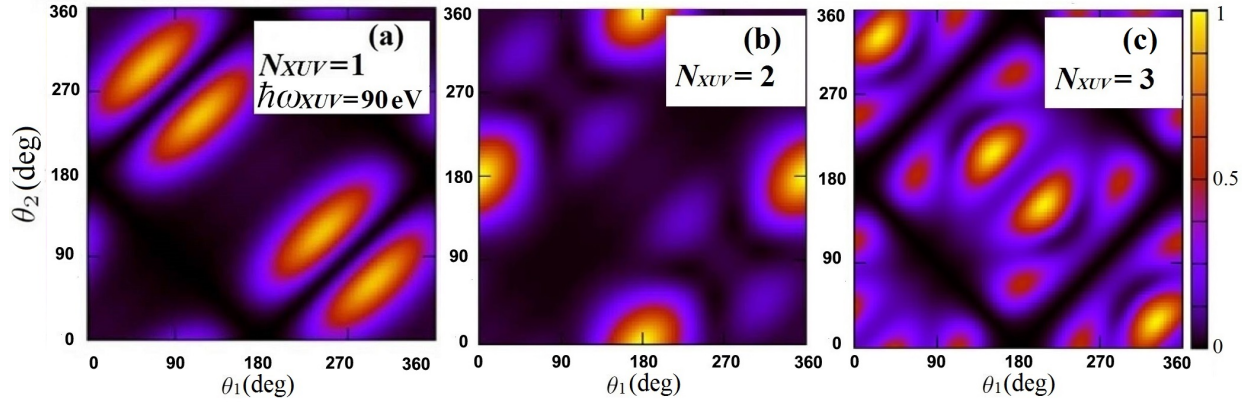


Figure 4.17: Calculated normalized joint angular distributions for the double ionization of helium at equal energy sharing by (a) single-photon DI by 90 eV XUV pulse, (b) two-photon DI by one 45 eV XUV pulse and (c) three-photon DI by 30 eV XUV pulse.

Briggs [56]. The absence of back-to-back emission agrees with the selection rule B2 which states that electron momenta satisfy $\hat{k}_1 = \pm \hat{k}_2$ and the sum of parity (π) and L is an odd integer, do not contribute to the DI process. The symbol π denotes the parity, with values 0 (for even parity) and 1 (for odd parity). This selection rule challenges the intuitive expectation that strong electronic correlation during non-sequential DI enforces back-to-back emission. However, since this would violate parity conservation, emission occurs instead with an angle of 130° between the emission directions of the electrons, rather than 180° . The absence of the conic emission is dictated by selection rule F. This rule stipulates that for $E_1 = E_2$ and $\theta_1 + \theta_2 = 180^\circ$, states with $M = 0$, odd values of $\pi + S$, and even values of $\pi + L$ do not contribute to the cross section. Side-by-side emission is forbidden because of the electronic Coulomb repulsion, and is also excluded by selection rule B2.

Our calculated angle-differential yield for equal-energy-sharing DI of helium as a result of the absorption of two 45 eV photons is shown in Fig. 4.17(b). It has four distinct peaks that correspond to back-to-back emission. Thus, features prohibited for single-photon sequential DI (back-to-back and conic emission) are dominant for two-photon DI, where the preferred emission type is back-to-back at equal energy sharing. The same conclusions can be drawn from the theoretical equal energy sharing JADs calculated by Zhang *et al.* [119] for photon

energies between 42 to 85 eV.

The JAD for DI by three-30 eV-photon DI is shown in Fig. 4.17(c). The selection rules demanding that back-to-back and side-by-side emissions be forbidden remain valid. This is similar to the single-photon JAD in Fig. 4.17(a) in the sense that the same forbidden emission patterns are present. In either case, back-to-back, conic, and side-by-side emission are prohibited, as mandated by selection rules [56]. For one- and three-photon DI the JADs contain the same dominant nodal lines.

Normalized DI yields for the emission of one electron along the XUV polarization direction ($\theta_2 = 0^\circ$ corresponding to the JADs in Figs. 4.18(a,b) are given in Figs. 4.18(c,d), respectively, where, in addition, contributions to the DI yields from individual allowed angular momenta L of the two-electron state are shown. These contributions are obtained by restricting the sum over L in Eqn. (2.40) to $L = 0$ or 2 in Fig. 4.18(c) and to $L = 1$ or 3 in Fig. 4.18(d). The shape of the angular distributions in Fig. 4.18 depends on the interference of the two contributing partial waves. Our two-photon angular distribution in Fig. 4.18(c) is dominated by D -waves ($L = 2$) and is in fair agreement with the CCC calculations of Kheifets and Ivanov [40] and in good agreement with the time-dependent close-coupling calculations of Colgan and Pinzola [11].

In general, successively increasing the number of absorbed XUV photons leads to JADs with alternating forbidden and dominant back-to-back and conic emission. This finding is consistent with the selection rules for equal energy sharing derived by Maulbetsch *et al.* [56, 57] and it is retained in the simplified, reduced-dimensionality model of Ni *et al.* [65] who constrained the center-of-mass of the two electrons to move on a straight line along the XUV polarization direction.

In Fig. 4.10 and Fig. 4.19, we display the JAD (a-c) and MAD (d) of 90 eV XUV single-photon DI and 45 eV two-photon DI, respectively. The energy sharing parameters are (a) 0.5 (equal energy sharing), (b) 0.1 (unequal energy sharing), and (c) 0.01 (extremely unequal energy sharing).

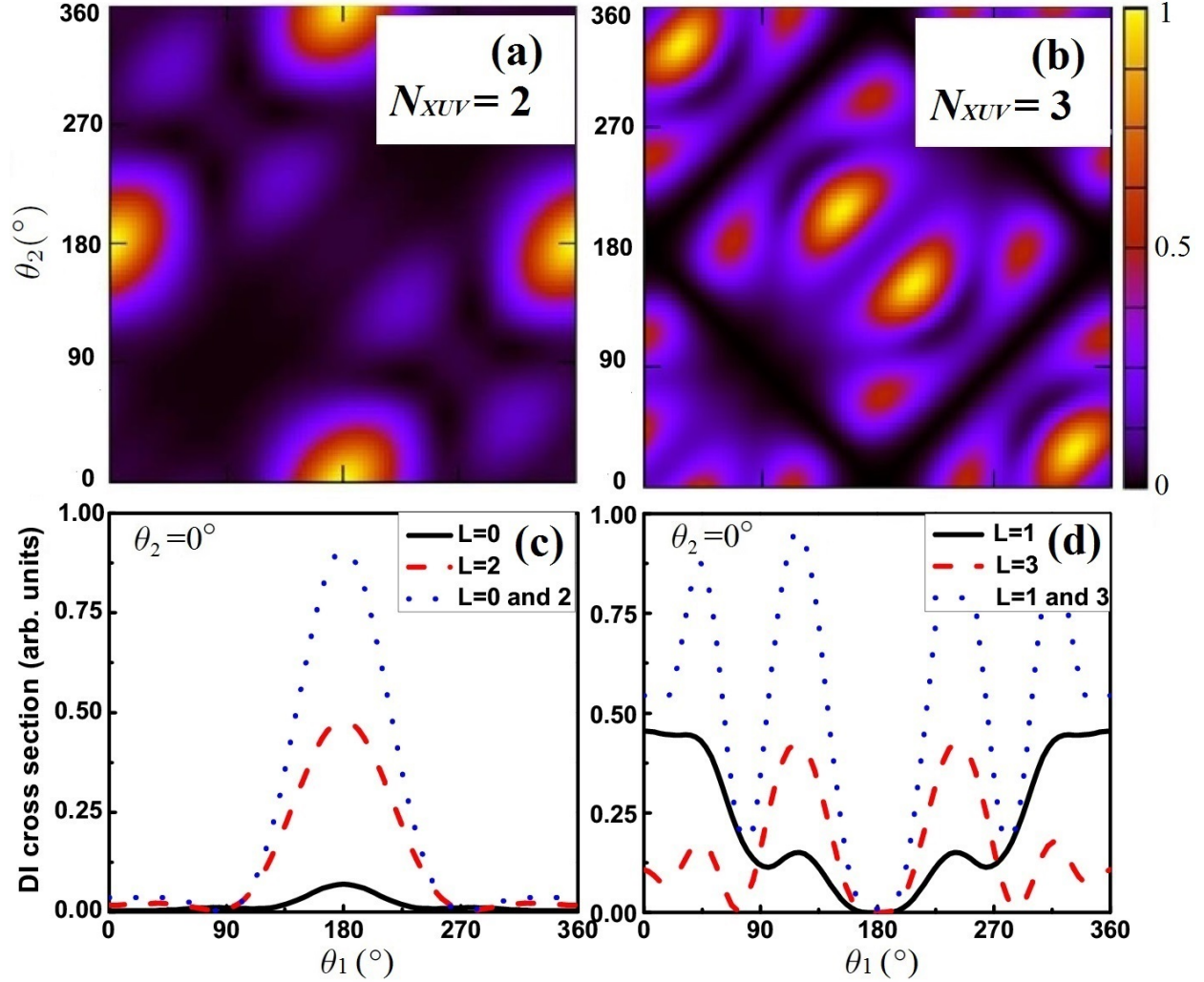


Figure 4.18: Calculated normalized joint angular distributions for the double ionization of helium at equal energy sharing by (a) two 45 eV photons and (b) three 30 eV photons in XUV pulses with a peak intensity of 10^{14} W/cm^2 and a pulse length of 1 fs. Panels (c) and (d): DI cross sections for individual total angular momentum (black solid and red dashed lines) that contribute to DI for two-photon DI (c) and three-photon DI (d) at fixed angle $\theta_1 = 0^\circ$. Cross sections (blue dotted lines) including (c): $L = 0$ and 2 and (d): $L = 1$ and 3.

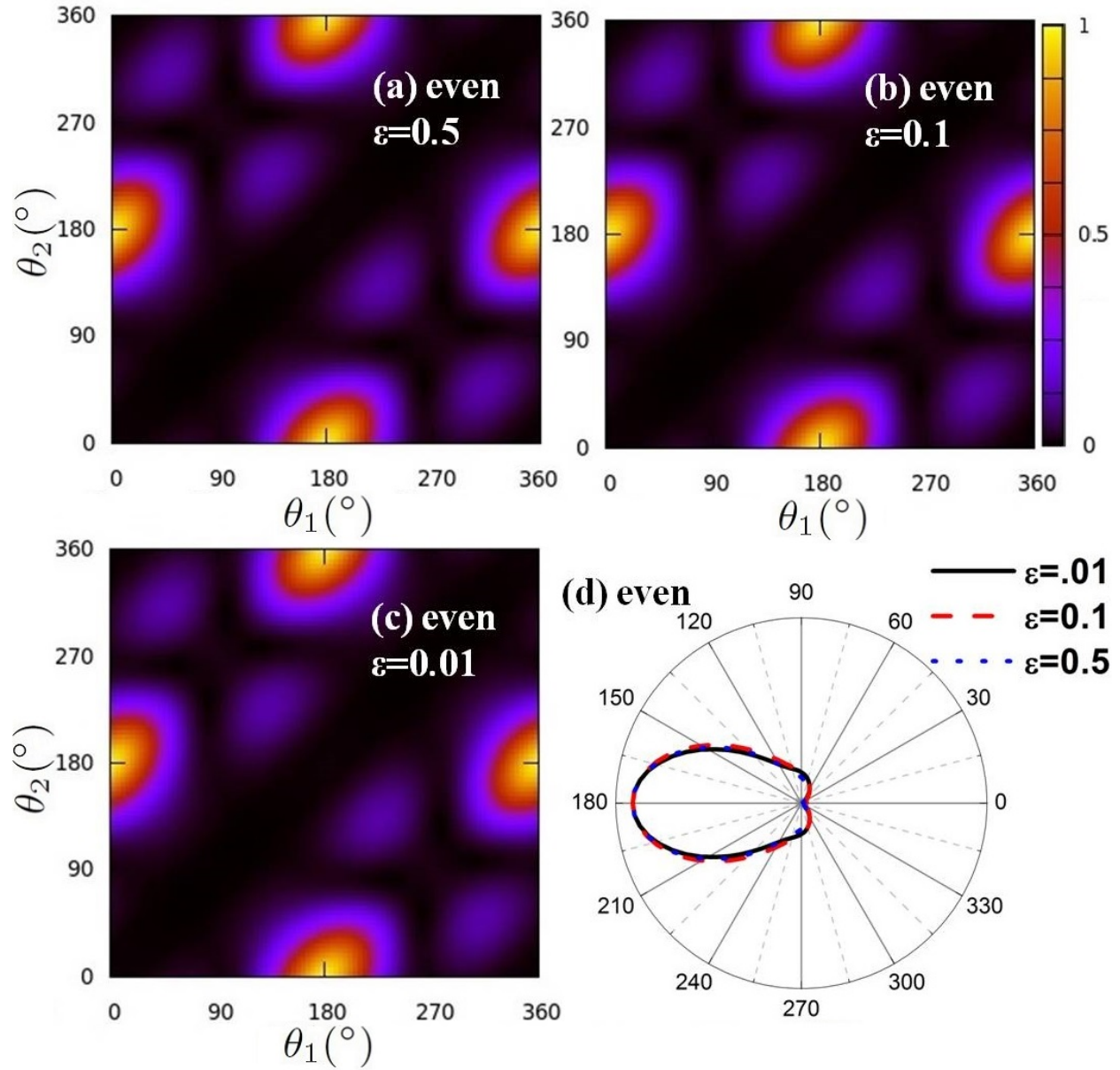


Figure 4.19: Calculated normalized joint angular distribution for the double ionization of helium by two $\hbar\omega_{\text{XUV}} = 45$ eV XUV photons at (a) equal energy sharing $\varepsilon = 0.5$, (b) unequal energy sharing $\varepsilon = 0.1$, and (c) extremely unequal energy sharing $\varepsilon = 0.01$. (d) Mutual angular difference distributions extracted from (a-c). The XUV pulse has a peak intensity of 10^{14}W/cm^2 and a pulse length of 1 fs. JADs for two-photon DI at different energy sharing. For two-photon DI, the JAD is not sensitive to the energy sharing change. From equal energy sharing $\varepsilon = 0.5$ to extremely unequal energy sharing $\varepsilon = 0.01$, the JAD is almost independent to the energy sharing ε .

In Fig. 4.10 (a-c), the JADs of single-photon DI show that from equal energy sharing ($\varepsilon = 0.5$) to unequal energy sharings ($\varepsilon = 0.1$ and 0.01), we observe that the symmetric component (symmetric emission) remains dominant, but the asymmetric component (back-to-back emission) raises from zero at equal energy sharing to a strong signal at extremely unequal energy sharing. The MAD in Fig. 4.10(d) clearly shows this change. The blue dotted curve represents the equal energy sharing results, the red dashed curve shows the unequal energy sharing with $\varepsilon = 0.1$, and the black solid curve shows the extremely unequal energy sharing ($\varepsilon = 0.01$) distribution. Each curve is divided by its total yield. The 90 eV XUV single-photon DI yield is almost flat over different energy sharings as discussed in the energy distribution in Fig. 4.16(d). The equal-energy-sharing curve shows that both back-to-back (anti-parallel) emission and side-by-side (parallel) emission are forbidden. The unequal-energy-sharing ($\varepsilon = 0.1, 0.01$) curves display that the more asymmetric the energy sharing is, the more back-to-back emission occurs. There is no side-by-side emission for any energy sharing. With regards to MAD, the blue dotted equal-energy-sharing curve shows no back-to-back emission and no side-by-side emission, with a dominant mutual angle of $\Theta_{12} = 130^\circ$. The red-dashed and black-solid curves show that the back-to-back emission is no longer forbidden. The $\varepsilon = 0.01$ curve shows that the yield at back-to-back emission is about 70% of the yield at $\theta_{12} = 130^\circ$.

Normalized calculated JAD for the helium DI by two $\hbar\omega_{XUV} = 45$ eV XUV photons are shown in Fig. 4.19 (a-c). The central XUV-photon energy and spectral profile of the 1 fs XUV pulses are in the photon energy range for non-sequential DI, $39.5 \text{ eV} < \hbar\omega_{XUV} < 54.4 \text{ eV}$, excluding contributions due to sequential DI. After the absorption of two photons, the final state of the three-particle system has even parity, the total angular-momentum quantum number L being equal to either 0 or 2. In contrast to the single-photon DI, where the odd final-state parity prohibits back-to-back emission, both equal and unequal energy sharing are subject to the same selection rules [54]. Back-to-back emission is now allowed for any energy sharing of the photoelectrons. As a result of the double electron-emission process

depending on electronic correlation and the lack of censorship imposed by selection rules, unhindered electronic repulsion shapes the JADs. Accordingly, our JADs for equal energy sharing in Fig. 4.19 (a), unequal energy sharing with $\varepsilon = 0.1$ [Fig. 4.19 (b)], and extremely unequal energy sharing with $\varepsilon = 0.01$ [Fig. 4.19 (c)] are insensitive to the energy sharing and dominated by back-to-back emission.

The MADs in Fig. 4.10 (d) clearly display the dependence of single-photon DI on the energy sharing, that is seen in the underlying JADs [Figs. 4.10 (a-c)]. The MADs show further that the photoelectrons are almost exclusively emitted into opposite hemispheres over a large range of energy sharing parameters ε . The curve for equal energy sharing $\varepsilon = 0.5$ conforms with the symmetry requirement of vanishing back-to-back and side-by-side emission, while back-to-back emission becomes more prominent for unequal ($\varepsilon = 0.1$) and extremely unequal $\varepsilon = 0.01$ energy sharing. For all energy sharings side-by-side emission is absent and the dominant mutual angle is $\Theta_{12} \approx 130^\circ$. At $\varepsilon = 0.01$ the yield at back-to-back emission is about 70% of the yield at $\theta_{12} = 130^\circ$.

The MADs for DI by two 45 eV photons in Fig. 4.19 (d) show dominant back-to-back emission and two minor peaks at $\theta_{12} \approx 75^\circ$ and $\approx 285^\circ$. The minor peaks correspond to the four minor peaks for symmetrical emission seen along the negatively sloped diagonal lines in the underlying JADs in Figs. 4.19 (a-c). The MADs also show almost no dependence on the energy sharing, as the JADs in Fig. 4.19 (a-c).

4.7 Conclusion of this Chapter

We briefly reviewed and discussed the few-photon DI of helium by short XUV pulses. Depending on the parity, DI with absorption of odd (even) number of photons presents similar pattern in the JADs, respectively. However, the behavior of the odd and even JADs varies differently as the energy sharing changes. Odd parity JADs are dominated by symmetrical emission; back-to-back emission is fading in to compete with increasing asymmetry in energy sharing. In contrast, even parity JADs are dominated by the overlap of back-to-back

emission and conic emission at arbitrary energy sharing. We discussed their prominence and absence for sequential and non-sequential DI upon absorption of up to three XUV photons without the presence of an assisting IR laser field. The laser-assisted DI by single-XUV pulse will be discussed in Chap. 6.

Chapter 5

Distinction of Sequential and Non-Sequential Processes in Two-Photon Double Ionization

In this section, we investigate the correlation and angular distribution in two-photon DI from 39 eV to 70 eV, and discuss the relation between them. We find that the strong correlation will result in similar angular distribution for two-photon DI. This is a characteristic feature of non-sequential double ionization with two photons.

Unless specifically stated, based on the convergence test [see Appendix C], the angular configuration we used throughout this chapter is $(L, l_1, l_2)_{\max}=(3, 3, 3)$.

5.1 Discovery of Non-Sequential Double Ionization

In 1975 the mechanism of *non-sequential double ionization* was revealed in the photoionization of alkaline earth atoms [103]. It is enabled by strong electronic correlation and thus is clearly distinctive from the *sequential double ionization* mechanism. NSDI was observed for noble gas atoms in 1982 [42], and received rapidly increasing attention [22, 85, 111] after the 1994 photo-double ionization experiment on helium atoms by Walker *et al.* [110].

5.2 Single-Photon Double Ionization

Single-photon double ionization is the simplest case of non-sequential DI. It requires a photon to carry at least 79.01 eV energy to strip off two electrons in the helium atom. In Chap. 3, we have discussed the general characteristics of SPDI momentum and angular distributions. Since the initial singlet state is an S -wave, the one-photon interaction leads to the final states only in P -waves. However, due to the selection rules and electron-electron correlation, the dominant emission mode is neither side-by-side nor back-to-back. It shows a dominant and symmetric distribution with respect to the angle difference of 130° between two photoelectrons. With increasing photon energy, this dominant angle difference decreases. Figure 4.8(a) shows our *ab-initio*-calculated JADs $P(\theta_1, \theta_2; \varepsilon)$ for SPDI and coplanar emission geometry. These JADs were found [46] to agree well with experimental results [6] and illustrate that symmetric electron emission remains dominant over a wide interval of energy sharing parameters ε . In contrast, the anti-symmetric component (back-to-back emission) occurs only for unequal energy sharing. This dependence on ε is also seen in the mutual angular distributions (MADs), which display DI yields as a function of θ_{12} and are normalized individually in Fig. 4.8(b) [48]. Overall, these MADs for SPDI depend weakly on the energy sharing and show a dominant mutual angle of $\approx 130^\circ$.

5.3 Sequential and Non-Sequential Two-Photon Double Ionization

While SPDI is always non-sequential, for sufficiently long XUV pulses two-photon DI (TPDI) of helium atoms proceeds sequentially if the central XUV photon energy $\hbar\omega_{XUV}$ is larger than the second ionization potential ($I_2 = 54.4$ eV) and non-sequentially for 39.5 eV $< \hbar\omega_{XUV} < I_2$. For such pulses SDI and NSDI are clearly distinguishable. TPDI is much more difficult to detect than SPDI due to its extremely small total cross section ($\approx 10^{-52}$ cm⁴s) [27, 30, 46]. It was first measured in 2005 [30], followed by many theoretical studies [19, 27, 34, 40, 46, 48, 75, 119]. Photoelectron angular distributions for TPDI were calculated in the sequential

and non-sequential regimes by applying convergent close-coupling theory [40] and by using time-dependent close-coupling methods [27, 119].

If the spectral profile of an ultrashort XUV pulse overlaps the sequential and non-sequential DI regimes, the distinction between SDI and NSDI becomes difficult. Furthermore, for extremely short pulse duration of less than a few hundred attoseconds, strong electronic correlation is enforced, even for central pulses energies in the sequential regime. In this case the time between the two photoabsorption events is so short that the inter-electronic distance remains sufficiently small to entail strong correlation of the released electrons. Accordingly, calculated JADs for DI at $\hbar\omega_{XUV} = 70$ eV dramatically change for decreasing XUV pulse length, moving from a product of two independent dipole distributions in the long-pulse limit (a few femtoseconds) to progressively forward-backward asymmetrical distributions with increasingly suppressed forward emission (both electrons being emitted in the same direction along the XUV polarization direction), resembling JADs for NSDI [19].

The role of electronic correlation in TPDI of helium with ultrashort XUV pulses was investigated in previous *ab initio* calculations [19], yet it remains unclear how to *quantitatively* characterize and distinguish sequential and non-sequential contributions. In this section, we investigate JADs for the DI of helium and refer to the degree of forward-backward emission asymmetry as a measure for the relative importance of SDI. We calculate JADs by numerically solving *ab initio* the TDSE, expanding the atomic wave function in the four angular variables of the two electrons. These calculations employ the FE-DVR scheme, and propagate the two-electron radial wave function on a numerical grid for the electrons' radial coordinates r_1 and r_2 . We partition the numerical grid into 100 to 200 FEs (adjusting the number of elements to the pulse duration) and use a DVR basis set in each element. A detailed description of our implementation of this method is given in Chap. 2.

Unless stated otherwise, based on convergence tests in Appendix C, we truncate the angular expansion of the atomic wave function for orbital and total angular quantum numbers

larger than 3. Throughout this chapter we assume XUV pulses with sine-squared temporal profiles and peak intensities of 10^{14} W/cm².

Absorption of two photons by ground-state helium atoms results in interfering S and D partial waves which one might expect to result in more structured JADs than in SPDI. However, as pointed out by Kheifets *et al.* [40], TPDI angular distributions consist of five terms that include electronic correlation effects as similar Gaussian factors and can be divided into symmetrical and antisymmetrical components in analogy to the SPDI angular distributions discussed above. Figure 5.1 shows calculated JADs [Figs. 5.1(a,c)] and MADs [Figs. 5.1(b,d)] for TPDI in XUV pulses with a pulse length of 1 fs and central photon energies of 50 eV (Figs. 5.1(a,b)) and 70 eV (Figs. 5.1(c,d)), normalized to their maxima, respectively. While the angular distributions for the photon energy $\hbar\omega_{XUV} = 50$ eV in the NSDI regime are virtually indistinguishable for different energy sharings, for $\hbar\omega_{XUV} = 70$ eV, i.e., in the SDI regime, the character of the angular distribution changes from being strongly dominated by back-to-back emission at equal energy sharing ($\varepsilon = 0.5$) to dominant forward (side-by-side) emission at extremely unequal energy sharing ($\varepsilon = 0.01$). The independence of the NSDI angular distributions on ε [Figs. 5.1(a,b)] was also noted in previous calculations [119].

The equal-energy-sharing JADs for $\hbar\omega_{XUV} = 50$ eV [Fig. 5.1(a)] and 70 eV [Fig. 5.1(c)] are similar and dominated by back-to-back emission, with two weak peaks along the $\theta_2 = 360^\circ - \theta_1$ diagonal, indicating symmetrical emission, and no side-by-side ($\theta_2 = \theta_1$) emission. At unequal energy sharing and for $\hbar\omega_{XUV} = 70$ eV [bottom-right panel of Fig. 5.1(c)], back-to-back emission ($\theta_{1,2} = 180^\circ$) remains strong, but side-by-side emission becomes dominant, since the importance of electronic correlation in DI decreases with increasing asymmetry. The photoelectrons thus become more efficiently directed by the XUV electric field, leading to the emergence of side-by-side emission along the laser polarization direction as a typical aspect of SDI at unequal energy sharing.

For the pulse length of 1 fs and corresponding spectral width of 6 eV, the spectra of

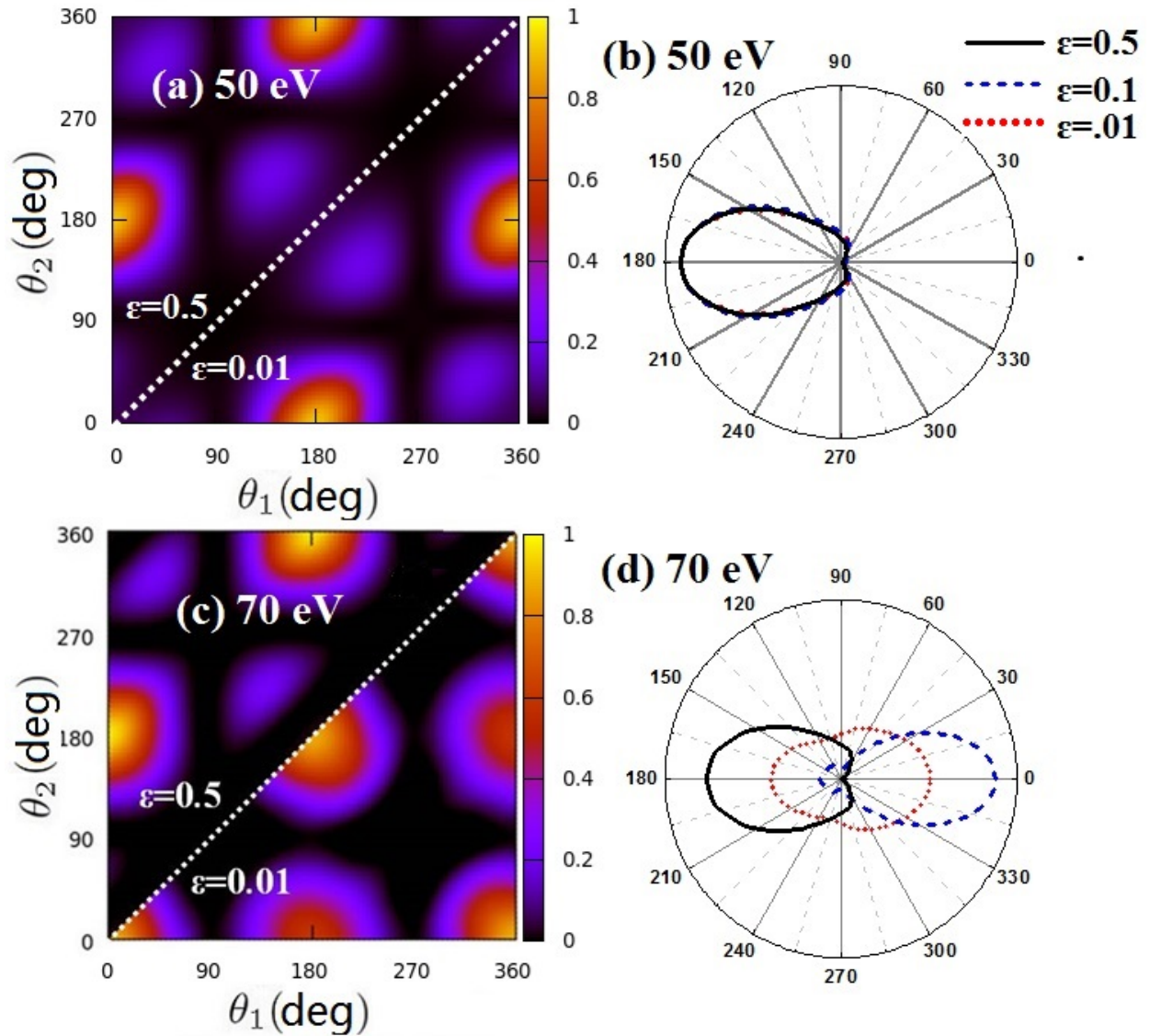


Figure 5.1: Calculated normalized (a,c) joint and (b,d) mutual angular distributions for two-photon double ionization of helium for energy sharing parameters $\epsilon = 0.01, 0.1, \text{ and } 0.5$. The XUV photon energy is (a,b) 50 eV and (c,d) 70 eV. All other XUV pulse parameters are the same as in Fig. 4.8.

the 50 and 70 eV XUV pulses considered above are confined to either the non-sequential or sequential DI regime, respectively. For significantly shorter pulse lengths, the distinction between these two DI spectral regimes becomes less obvious. As Feist *et al.* [19] revealed for central XUV-photon energies in the SDI regime, TPDI by ultrashort XUV pulses can have strong NSDI contributions. Conversely, as we show below, ultrashort XUV pulses that are spectrally centered in the NSDI regime can share the characteristics of SDI angular distributions.

5.4 Pulse-Duration Dependence of Two-Photon Double Ionization

In order to investigate the effect of spectral pulse overlap with the two DI regimes, in Fig. 5.2 we show conditional TPDI angular distributions for a fixed emission angle of one electron ($\theta_1 = 0^\circ$) and $\hbar\omega_{XUV} = 50$ eV XUV pulses with pulse durations of 160 as, 500 as, and 3 fs, corresponding to spectral pulse widths of 37, 12, and 2 eV [full-width at half-maximum (FWHM) in intensity], respectively. The full-range angular distributions in the left panel of each graph are normalized individually to their maxima. They show dominant back-to-back emission and minor peaks for emission into the same (“forward” relative to the XUV polarized direction) hemisphere. The normalized back-to-back emission yields for the two energy-sharing values and three pulse lengths are almost identical. The small forward-emission yields are displayed separately in the zoomed-in right panels. In contrast to the large back-to-back emission yields, the forward emission yields depend on the energy sharing and pulse length. They increase as the energy sharing changes from equal ($\varepsilon = 0.5$) to extremely unequal ($\varepsilon = 0.01$). This increase is most pronounced at the intermediate pulse length of 500 as [Fig. 5.2(b)]. The relatively strong forward emission for $\varepsilon = 0.01$ is reminiscent of the forward-emission dominance for SDI [cf. Fig. 5.1(c,d)]. Reducing the pulse length from 3 fs to 500 as, thus leads SDI character to the angular distribution. Interestingly, this trend is reversed by further reducing the pulse length from 500 as to 160 as, since the

constraint for DI to happen during the presence of the ultrashort 160 as pulse reinforces electronic correlation, suppressing (uncorrelated) sequential emission [19].

The preceding discussion suggests the SDI contribution has a lower pulse-length limit given by a temporal constraint, while being limited at larger pulse durations by vanishing spectral overlap with the SDI spectral domain. In order to quantitatively distinguish SDI from NSDI contributions, we evaluate the forward-backward asymmetry parameter

$$A(\theta_1 = 0; \varepsilon) = \frac{\left(\int_{-\pi/2}^{\pi/2} - \int_{\pi/2}^{3\pi/2} \right) P(0, \theta_2; \varepsilon) d\theta_2}{\left(\int_{-\pi/2}^{\pi/2} + \int_{\pi/2}^{3\pi/2} \right) P(0, \theta_2; \varepsilon) d\theta_2} \quad (5.1)$$

for the XUV-pulse durations, energy-sharing parameters, and central XUV-pulse energy considered in Fig. 5.2. The limiting cases of both electrons being emitted into the same hemisphere and into opposite hemispheres correspond to asymmetries of 1 and -1, respectively. As shown in Fig. 5.3, the asymmetry for 160 as and 3 fs pulse durations are large in magnitude ($A \approx -0.99$) and comparatively insensitive to changes in energy sharing. In contrast, the asymmetry for 500 as pulses more strongly depends on the energy sharing. It falls in between the asymmetries for 160 as and 3 fs pulses at equal energy sharing and increases to -0.956 at extremely unequal energy sharing ($\varepsilon = 0.01$). In order to compare this weak dependence of $A(\theta_1, \varepsilon)$ for pulses centered in the NSDI, the inset in Fig. 5.3 shows that asymmetry changes from 1 to -1 for XUV pulses with $\hbar\omega_{XUV}=70$ eV in the SDI regime and 1-fs pulse duration.

The inset in Fig. 5.4 shows the spectral intensity $I(\omega)$ of a 1 fs sine-squared XUV pulse with $\hbar\omega_{XUV} = 50$ eV. A small portion of $I(\omega)$ overlaps the SDI regime. Since $I(\omega)$ decreases rapidly above the second ionization threshold, the XUV-pulse spectral components in the SDI regime primarily account for DI with small excess kinetic energies of the emitted electrons, $E_1 + E_2 = 2\hbar\omega - 79.0$ eV, and extremely unequal energy sharing. For example, a typical frequency component of the pulse in the SDI regime at $\hbar\omega = 54.8$ eV results in a highly unequal energy sharing with $\varepsilon = (\hbar\omega - 54.4 \text{ eV}) / (2\hbar\omega - 79.0 \text{ eV}) = 0.013$. We therefore choose the small value $\varepsilon = 0.01$ for the following discussion.

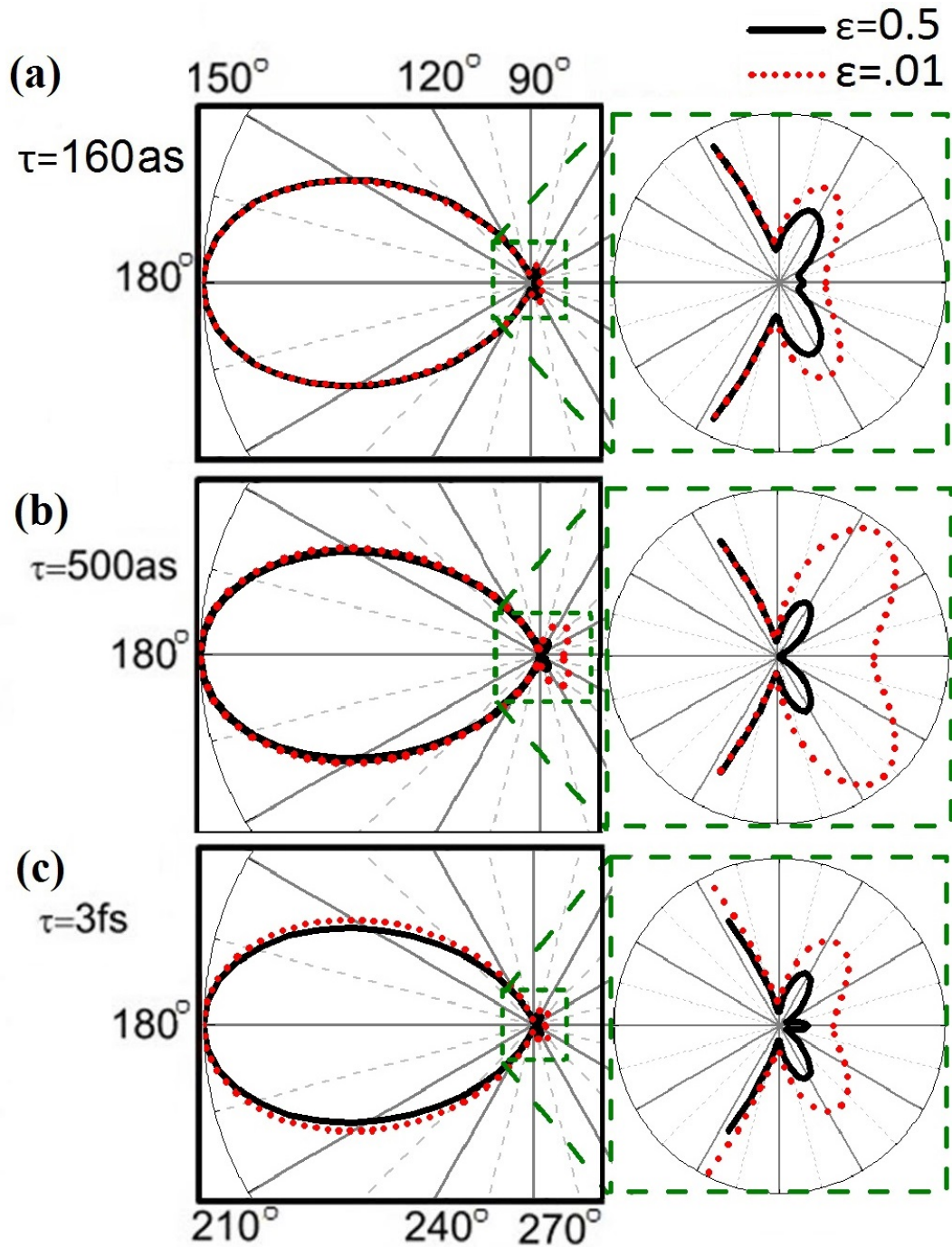


Figure 5.2: Conditional angular distributions with one electron emitted along the XUV linear polarization direction ($\theta_1 = 0^\circ$) for two-photon double ionization of helium in XUV pulses with a central photon energy of 50 eV and pulse lengths of (a) 160 as, (b) 500 as, and (c) 3 fs. Each panel shows results for equal ($\epsilon = 0.5$) and extremely unequal ($\epsilon = 0.01$) energy sharing. The full-range distributions (left panels) are normalized to their maxima. The right panels zoom in on the forward emission contributions.

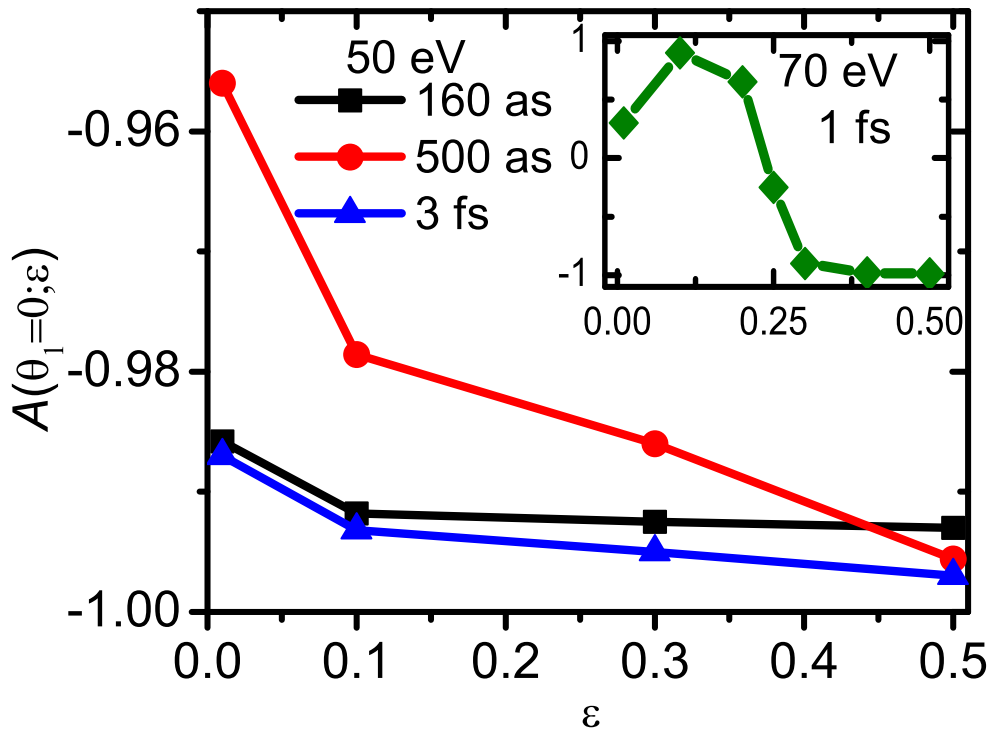


Figure 5.3: Forward-backward-emission asymmetries $A(\theta_1 = 0; \epsilon)$ for the conditional angular distributions in Fig. 5.2 and for $\epsilon = 0.1$ and 0.3 . The inset shows asymmetries for XUV pulses with a central photon energy of 70 eV and 1 fs pulse length, corresponding to the angular distributions in Figs. 5.1 (c,d). Markers represent ab initio calculations and are straight-line interpolated.

5.5 Yield of Sequential Two-Photon Double Ionization

Attempting to find a simple analytical description of the pulse-length dependence of A in Fig. 5.5, we first recall the known expression of the SDI yield [18, 75]

$$Y_{seq} = \frac{\sigma_1 \sigma_2 I_0^2}{\omega^2} (T_{\text{eff}})^2, \quad (5.2)$$

given in terms of the single-photon single-ionization cross sections for He (σ_1) and He⁺ (σ_2) and the effective interaction time of the XUV pulse for the single-photon processes, T_{eff} [Eqn. (2.74)]. For sine-squared pulses T_{eff} equals 3/8 times the full XUV-pulse duration τ [18, 27, 119].

5.6 Heuristic Formula

Guided by the SDI yield of Eqn. (5.2), we integrate over the SDI frequency range to construct the heuristic expression

$$Y_{seq}^{heur} = B \left[T_{\text{eff}} \int_{I_2}^{\infty} \frac{I(\omega)}{\omega} d\omega \right]^2 \quad (5.3)$$

for the SDI contribution, uniting the constraints for SDI on the temporal pulse profile (factor T_{eff}^2) and spectral overlap with the SDI spectral domain (factor $[\int_{I_2}^{\infty} \frac{I(\omega)}{\omega} d\omega]^2$). Figure 5.5 shows $\sqrt{Y_{seq}^{heur}}$ (blue solid line) for $\hbar\omega = 50$ eV after adjusting the proportionality constant B to the results of our *ab initio* calculation (stars). The stars in Fig. 5.5 show the asymmetries $A(\theta_1 = 0; \varepsilon = 0.01)$ derived from our *ab initio* FE-DVR numerical solution of the TDSE according to Eqn. (5.1) for XUV-pulse lengths between 160 as and 2.5 fs. Consistent with Figs. 5.2 and 5.3, the asymmetries are largest near 500 as. The normalized heuristic SDI contribution (blue solid curve) reaches its maximum at a pulse length of 650 as, in agreement with our *ab initio* calculation.

This confirms that the SDI yield can be neglected for pulse durations longer than 1.5 fs, as one would expect in view of the vanishing overlap between the pulse spectrum and the SDI spectral range. It also confirms the requirement of a sufficiently long pulse duration for SDI to occur, as discussed above. Accordingly, due to relatively small SDI contributions,

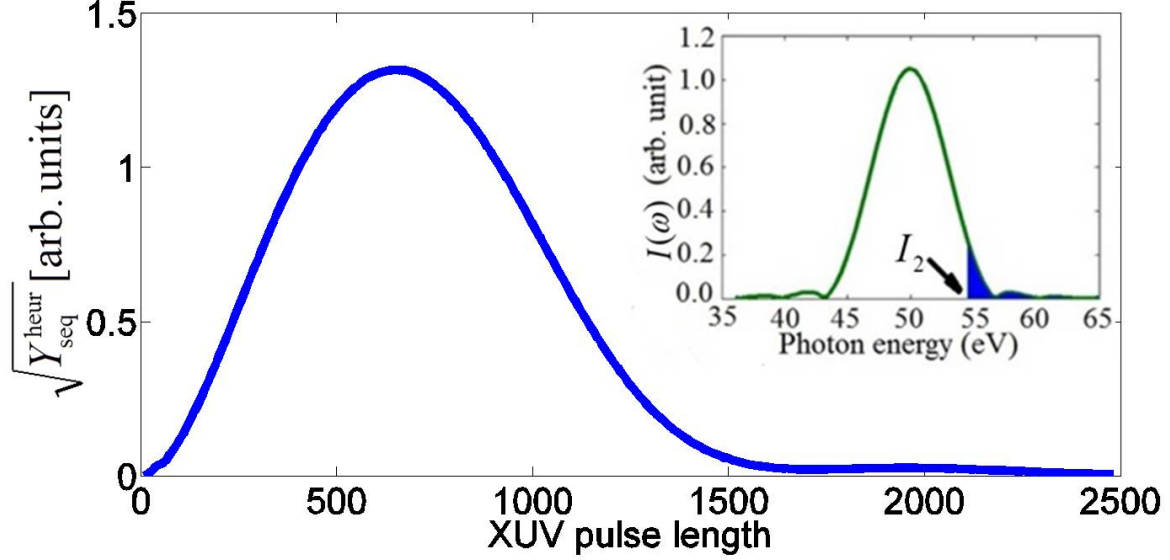


Figure 5.4: Effective sequential-double-ionization yield versus the total pulse duration. The yield is calculated by the heuristic formula Eqn. (5.3). The inset shows the spectrum of an $\hbar\omega_{XUV} = 50$ eV pulse with sine-squared temporal profile and a pulse length of 1 fs. The blue area indicates the overlap of the pulse spectrum and the spectral domain for sequential double ionization at $\hbar\omega > 54.4$ eV.

the asymmetries for 160 as and 3 fs in Fig. 5.3 are comparatively robust against changes in energy sharing [cf. Figs. 5.1 (a,b)].

5.7 Emission Asymmetry Parameter and Effective Sequential Double-Ionization Yield

In the discussion of Fig. 5.2 and Fig. 5.3, we have noticed that the emission asymmetry parameter A vanishes at both ultrashort and long pulse durations, and has a maximum around 500 as of pulse durations. In Fig. 5.5, we calculated 10 different pulse durations, and plotted the forward-backward DI asymmetries A with the square root of effective sequential-double-ionization yield. Based on the proportionality of $\sqrt{Y_{seq}^{heur}}$ and our *ab initio* calculated forward-backward DI asymmetries A , we conclude that A is a good indicator for the SDI contribution to the DI of helium for central pulse energies in the NSDI spectral domain.

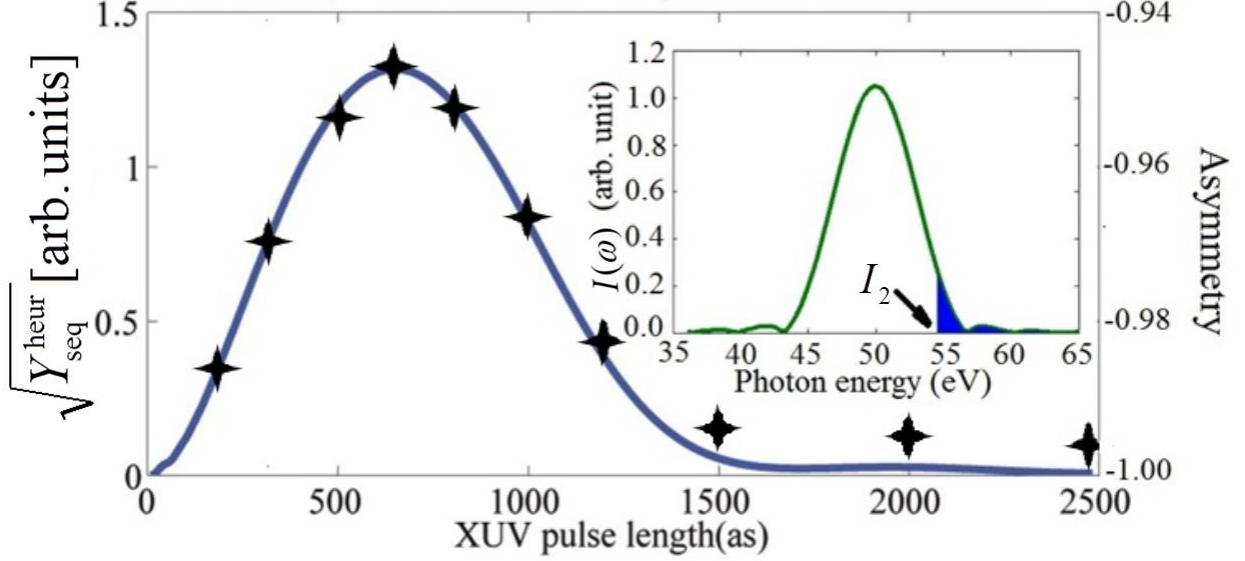


Figure 5.5: Comparison of *ab-initio* calculated forward-backward double-ionization asymmetries $A(\theta_1 = 0; \varepsilon = 0.01)$ (stars) with the heuristic formula [Eqn. (5.3)] for the sequential-double ionization contribution Y_{seq}^{heur} (solid blue line) as a function of the XUV-pulse length for a central pulse energy of 50 eV. The sequential double ionization yield is normalized to the maximum of A at 650 as. The inset displays the spectrum of an $\hbar\omega_{XUV} = 50$ eV pulse with sine-squared temporal profile and a pulse length of 1 fs. The blue area indicates the overlap of the pulse spectrum and the spectral domain for sequential double ionization at $\hbar\omega > 54.4$ eV.

This offers the possibility of determining the pulse lengths of ultrashort XUV pulses based on measured asymmetries A .

5.8 Conclusions of this Chapter

We studied sequential and non-sequential contributions to the TPDI of helium. We calculated photoelectron angular distributions by applying the FE-DVR numerical method to solve *ab initio* the TDSE for helium exposed to the electric field of an ultrashort XUV pulse. We found that forward-backward asymmetries of two-photoelectron angular distributions constitute an appropriate measure for the distinction between sequential and non-sequential DI contributions. We confirmed this link between the forward-backward asymmetry and the sequential DI contribution for central pulse energies below I_2 by matching the pulse-

length-dependent profile of our *ab initio* calculated forward-backward asymmetry with an intuitively appealing heuristic formula for the square root of the SDI fraction.

Chapter 6

Laser-Assisted Single-XUV-Photon Double Ionization

Observing the ultrafast motion in molecules and atoms in real time has been a fascinating and challenging task. A significant breakthrough was made by Ahmed H. Zewail, who won the 1999 chemistry Nobel prize for developing a rapid laser technique that enables scientists to study the action of atoms in chemical reactions, leading to the creation of femtochemistry [115, 116]. This technique is called the pump-probe technique, and is the analog of conventional snapshot photography.

In this chapter, we start to apply our new developed code to an XUV-pump-IR-probe investigation. However, due to the limits of computational resources, we only studied the special case, where the XUV and IR pulse overlap, that is, we only present results for zero delay between the XUV and IR pulses. We note, however, that our code is ready for the calculation of an entire delay range. Such calculations, based on our code, remain to be done with access to the most powerful computational resources available at supercomputer centers, such as National Energy Research Scientific Computing Center (NERSC) and the Oak Ridge Leadership Computing Facility (OLCF). We added a short and comparatively weak IR pulse to the single-XUV-photon DI process in helium atoms, and studied how the IR field will change the energy and angular distributions of photoelectrons.

For all numerical results in this chapter we used the angular momentum limits (L_{\max} , l_1^{\max}),

$l_2^{\max}) = (3, 3, 3)$ for one-photon DI and two-photon DI and $(L_{\max}, l_1^{\max}, l_2^{\max}) = (5, 5, 5)$ for all other processes in the expansion Eqn. (2.40), unless specified otherwise.

6.1 XUV Double Ionization in the Presence of an IR Laser Pulse

The presence of a comparatively weak IR pulse during the DI of helium in an intense XUV pulse can strongly modify the energy and angular distribution of photoelectrons. In this section we discuss and quantify effects of an assisting IR laser electric field on the XUV-DI process. The XUV and IR pulse are assumed to have overlapping sine-squared temporal profiles, as given in Eqn. (2.30), with identical phases ($\varphi_{\text{XUV}} = \varphi_{\text{IR}} = 0^\circ$). The XUV-pulse has a peak intensity of $I_{\text{XUV}} = 10^{14}$ W/cm², the central photon energy $\hbar\omega_{\text{XUV}} = 89$ eV, and a pulse length (full width at half intensity) of 10 XUV cycles or 0.46 fs. The IR parameters are $I_{\text{IR}} = 3 \times 10^{12}$ W/cm², and $\hbar\omega_{\text{IR}} = 1.61$ eV. At this intensity the IR pulse by itself would not ionize the atom [110]. We will discuss energy and angular distributions for assisting IR pulses with pulse lengths of 1 and 4 IR cycles or 2.6 and 10.3 fs, respectively.

6.1.1 Energy Distributions

Figure 6.1 shows the joint energy distributions for laser-assisted single XUV photon DI for an IR pulse length of 2.6 fs. Figures 6.1(a) and 6.1(b) display joint distributions where the effective number of absorbed minus emitted IR photons is even and odd, respectively. We separated the contributions from even and odd IR photon numbers in order to clearly resolve the sideband pattern [60, 117] in the joint energy distribution. Each stripe in the pattern complies with energy conservation, representing a certain effective number N_{IR} of absorbed minus emitted IR photons.

In each graph of Fig. 6.1, neighboring stripes are separated by the energy of two IR photons (~ 3.2 eV), as indicated by dashed and dotted lines. Regardless of the photon number, the largest DI yield occurs at equal energy sharing. The most intense stripes in

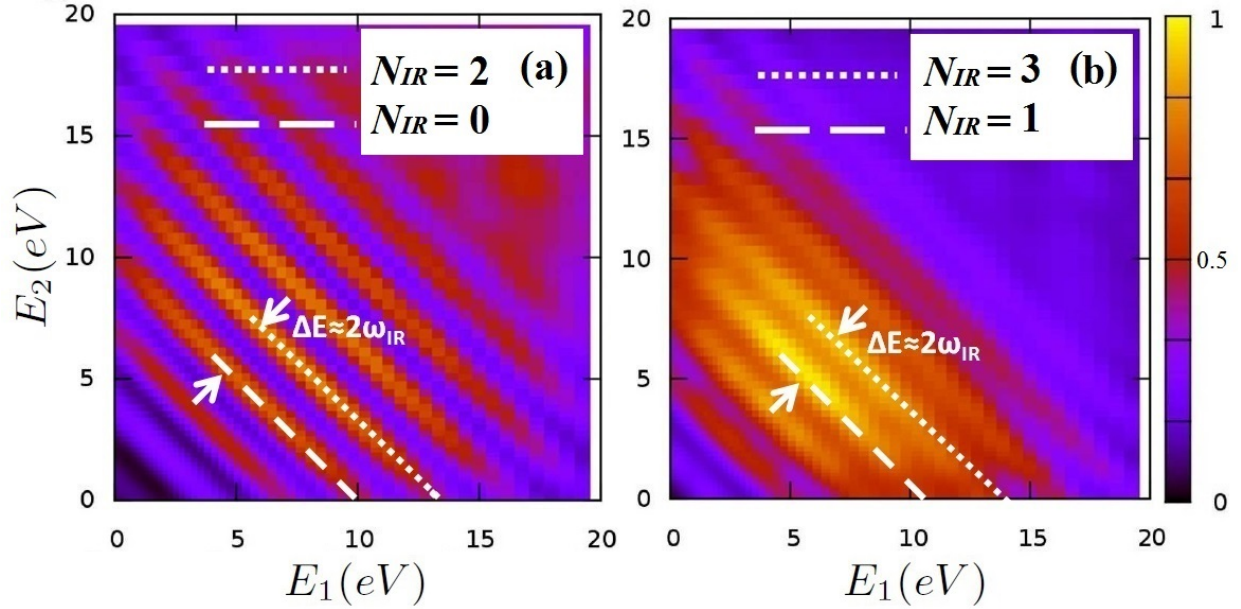


Figure 6.1: Normalized joint photoelectron energy distributions for IR-laser-assisted single-photon double ionization of helium at equal energy sharing in a 10-cycle XUV pulse of peak intensity 10^{14} W/cm², central photon energy $\hbar\omega_{XUV} = 89$ eV, and pulse length 0.46 fs. The assisting single-cycle laser pulse has a peak intensity of 3×10^{12} W/cm², photon energy of $\hbar\omega_{IR} = 1.61$ eV, and a pulse length of 2.6 fs. (a) Even effective numbers of IR photons. (b) Odd effective numbers of IR photons.

Fig. 6.1(a) occur at the total energies $E_1 + E_2 \approx 10, 13.2,$ and 16.4 eV, corresponding to the absorption of one XUV photon and, effectively, 0, 2, and 4 IR photons. The largest DI yields in Fig. 6.1(b) are located at $E_1 + E_2 \approx 11.5$ eV, corresponding to the absorption of (effectively) one XUV photon and one IR photon.

6.1.2 Angular Distributions for Even and Odd IR Photon Numbers

We analyze JADs for the special case of both emitted electrons having the same final kinetic energy. As in the previous subsection, we separately consider even and odd effective photon numbers for clarity. Figures 6.2(a,b,e) and (c,d,f) show our numerical results for laser-assisted XUV-photon DI of helium for odd and even total photon numbers, respectively. We obtain these angular distributions by integrating joint energy distributions across all sidebands for equal energy sharing. Note that for odd total photon numbers in Figs. 6.2(a,b,e) we include one 89 eV XUV plus any even number of IR photons. Likewise, for even total photon numbers in Figs. 6.2(c,d,f), we include one XUV plus any odd number of IR photons.

Figure 6.2(f) shows results for laser-assisted two-photon DI, including two 45 eV XUV and any even number of IR photons. We obtain the laser-assisted single XUV-photon JADs by including combined excess energies of the two electrons up to $E_{\text{exc}}^{\text{max}} = 3.0$ a.u. ≈ 82 eV, corresponding to $N_{\text{IR}} \leq 45$. The IR pulse lengths are 2.6 fs and 10.3 fs in Figs. 6.2(a,c) and (b,d), respectively, corresponding to one and four IR cycles. Figures 6.2(e) and (f) compare the JADs for symmetric emission by one and two XUV photons, respectively.

The nodal lines in the JADs for single- and three XUV-photon DI of helium without laser assistance in Figs. 4.8(a) and 4.18(b) resist the addition of any even effective number of IR photons in Figs. 6.2(a,b). Combinations of photoelectron emission directions that are forbidden in the absence of an IR laser pulse thus remain forbidden upon addition of the laser pulse, as long as the total number of photons remains odd. Likewise, for even total photon numbers, JADs without [Fig. 4.18(a)] and with an assisting laser pulse [Figs. 6.2(c,d)] are similar and dominated by back-to-back emission. For both, even and odd photon numbers,

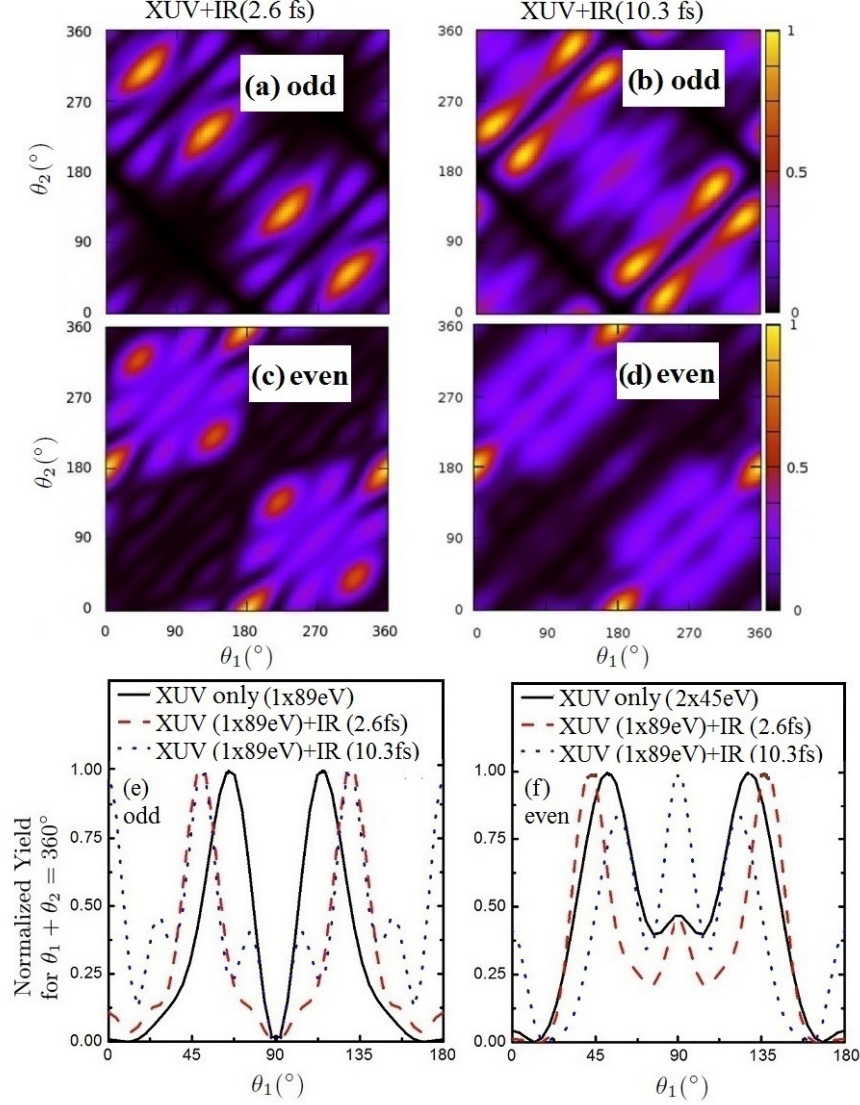


Figure 6.2: Normalized joint angular distributions for IR-laser-assisted double ionization of helium at equal energy sharing in a 10-cycle XUV pulse of peak intensity 10^{14} W/cm² and central photon energies of $\hbar\omega_{\text{XUV}} = 89$ eV and 45 eV. The assisting IR pulse has a peak intensity of 3×10^{12} W/cm², central photon energy $\hbar\omega_{\text{IR}} = 1.61$ eV, and pulse lengths (a,c) 2.6 fs and (b,d) 10.3 fs. (a-d) Laser-assisted single-89 eV-photon double ionization for (a,b) odd and (c,d) even total effective numbers of XUV and IR photons. (e) Normalized single-89 eV-photon double ionization for symmetric emission with and without assisting IR-laser pulses of pulse lengths 2.6 fs and 10.3 fs for odd total effective numbers of XUV and IR photons. (f) Normalized single-89 eV-photon double ionization for symmetric emission with an assisting 2.6 fs or 10.3 fs IR-laser pulse for even total effective numbers of XUV and IR photons, compared with IR-laser-free two-45 eV-photon double ionization. Calculation with angular momentum limits $(L_{\text{max}}, l_1^{\text{max}}, l_2^{\text{max}}) = (4, 4, 4)$ in Eqn. (2.40).

the assistance of the IR pulse adds structure to the JAD, along lines with $\theta_1 + \theta_2 = \text{const}$ and most obviously for symmetric emission.

In comparison with the laser-free XUV DI in Fig. 4.8(a) and Fig. 4.18, the laser-assisted yields in Fig. 6.2 show weak but enhanced (not observable) side-by-side emission, indicating a more pronounced influence of electronic correlation during the laser-assisted DI process. Increasing the IR pulse length from 2.6 fs to 10.3 fs leads to a redistribution of yields in the JADs. For odd total photon numbers, the four dominant symmetric emission peaks along $\theta_1 + \theta_2 = 360^\circ$ in Fig. 6.2(a) recede as the IR pulse length is increased to 10.3 fs in Fig. 6.2(b) and the dominant yield becomes focussed in eight peaks along lines $\theta_1 + \theta_2 = (360 \pm 90)^\circ$, consistent with the transfer of discrete amounts of IR-photon momenta. For even total photon numbers, the increase of the IR pulse length from 2.6 fs in Fig. 6.2(c) to 10.3 fs in Fig. 6.2(d) preserves the dominant back-to-back emission along the laser- and XUV-polarization direction. As for odd photon numbers, the more diffuse appearance of the JADs for the longer IR pulse can be understood as the result of a prolonged momentum exchange with the IR-laser electric field during the photoemission process.

Figures 6.2(e) and (f) include cuts of the JADs in Fig. 6.2(a-d) and Fig. 4.18(a) along the symmetric-emission line given by $\theta_1 + \theta_2 = 360^\circ$. Since convergence in the propagation time is slowest for side-by-side emission, the DI yield at $\theta_1 = 180^\circ$ in Figs. 6.2(e) and (f) allows us to quantify the overall degree of convergence achieved in the numerical calculation. For a fully converged calculation this yield has to vanish. In general, our JADs are closest to convergence for laser-free XUV DI and least converged for the longest pulse lengths of the assisting laser, for otherwise identical physical and numerical parameters. The deterioration of the convergence induced by the assisting laser pulse is more severe for odd photon numbers in Fig. 6.2(e).

6.1.3 Angular Distributions for Specific Effective IR Photon Numbers

Figure 6.3 shows normalized JADs for single-XUV photon DI of helium for specific even and odd total numbers of photons within the range $-1 \leq N_{\text{XUV}} + N_{\text{IR}} \leq 4$. Negative (positive) IR-photon numbers N_{IR} indicate that the number of emitted IR photons exceeds (is smaller than) the number of absorbed IR photons. The pulse length of the assisting IR laser pulse is 2.6 fs. All other laser, XUV-pulse, and numerical parameters are the same as in the preceding Sec. 6.1.2. These JADs were obtained from the energy distributions in Fig. 6.1 by integrating over a small energy domain near equal energy sharing given by

$$|E_1 + E_2 - E_{\text{exc}}| < \omega_{\text{IR}}. \quad (6.1)$$

where $E_{\text{exc}} = N_{\text{XUV}}\omega_{\text{XUV}} + N_{\text{IR}}\omega_{\text{IR}} - I_{p_1} - I_{p_2}$ is the total excess energy due to the (net) absorption of N_{XUV} ($=1,2$) XUV and N_{IR} IR photons. As for all JADs shown in this paper, each JAD is normalized separately to its maximum yield.

The IR-photon-number specific JADs in Figs. 6.3(a-f) resemble the distribution for unspecified odd and even photon numbers in Fig. 6.2(a) and (c). For odd photon numbers, the DI yields become more concentrated in the four prominent peaks at and near symmetric emission while all other structures loose intensity as N_{IR} is increased from -2 to 2 in Figs. 6.3(a-c). As observed for the laser-free XUV emission in Fig. 4.8(a) and for the laser-assisted emission in Figs. 6.2(a,b), back-to-back and conic emission remain separately forbidden for each number of IR photons N_{IR} , as long as the total photon number is odd.

For even N_{IR} symmetric emission is most likely. The progressive concentration of the DI yield in four peaks along the symmetric emission direction as N_{IR} increases from -2 to 3 in Figs. 6.3(a-f) is more pronounced for even than for odd total photon numbers. As for laser-free DI by absorption of two XUV photons in Fig. 4.18(a) back-to-back emission contributes significantly for laser-assisted XUV DI with $N_{\text{IR}} = -1$ [Fig. 6.3(d)]. However, as more IR photon are effectively absorbed, the momenta transferred from the IR-laser field onto the photoelectrons progressively weaken back-to-back emission and increase the relative

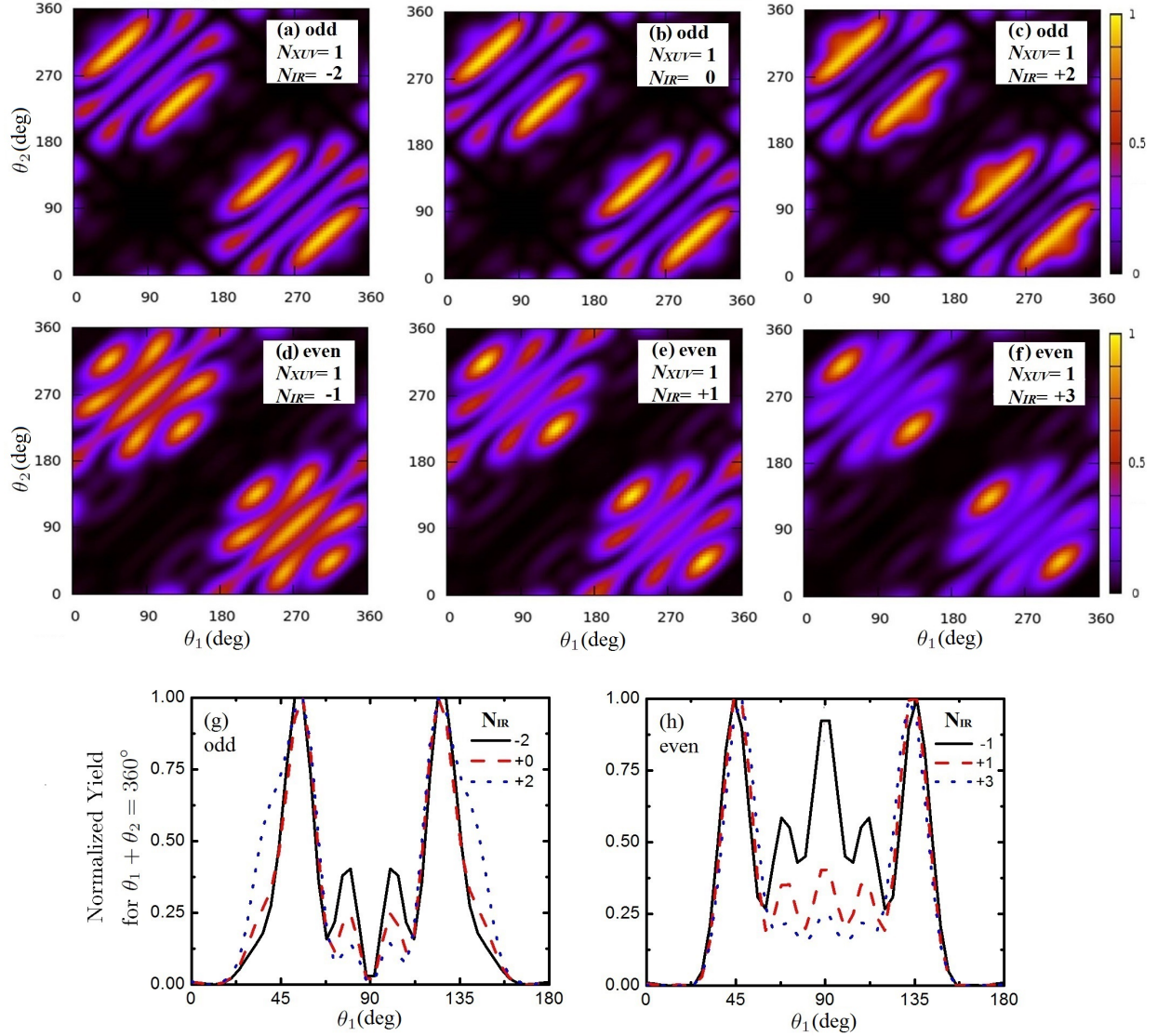


Figure 6.3: Normalized joint angular distributions for IR-laser-assisted single-XUV-photon double ionization of helium in a 10-cycle XUV pulse of peak intensity 10^{14} W/cm² and central photon energy (a-f) $\hbar\omega_{XUV} = 90$ eV. The assisting IR laser pulse has a pulse length of 2.6 fs. All other parameters are the same as for Fig. 6.2. (a-c,g) Odd and (d-f,h) even total effective numbers of photons. The effective number of absorbed IR photons is (a) $N_{IR} = -2$, (b) 0, (c) 2, (d) -1, (e) 1, and (f) 3. Negative photon numbers indicate that more IR photons are emitted than absorbed. (g,h) Normalized yields for symmetric laser-assisted XUV double-ionization. (g) Odd total numbers of photons with $N_{IR} = -2, 0$, and 2. (h) Even total numbers of photons with $N_{IR} = -1, 1$, and 3.

importance of symmetric emission in the dominant four peaks in Figs. 6.3(e) and (f). For increasing numbers of effectively absorbed IR photons, symmetric emission thus becomes more dominant for both, odd and even photon numbers. For equal energy sharing of the photoelectrons, this can be regarded as a compromise between (i) the simultaneous transfer of equal amounts of momenta along the laser and XUV pulse polarization direction from the IR-laser field to the emitted electrons (promoting side-by-side emission) and (ii) electronic repulsion (prohibiting side-by-side emission at sufficiently large propagation times).

The normalized DI yields for symmetric laser-assisted XUV DI for odd total photon numbers in Fig. 6.3(g) show a steady decrease of the DI yield near the back-to-back emission direction at $\theta_1 \approx (90 \pm 12)^\circ$ as N_{IR} is increased from -2 to +2. Simultaneously, the dominant symmetric emission peaks in this graph at $\theta_1 \approx 55^\circ$ and $\approx 125^\circ$ become broader, as one would expect for larger numbers of absorbed IR photons. For the case of even total photon numbers in Fig. 6.3(h) symmetric back-to-back emission in direction perpendicular to the laser polarization direction ($\theta_1 = 90^\circ$) becomes less likely as N_{IR} is increased from -1 to +3, in agreement with the intuitive picture of increasing momentum being transferred from the external IR electric field to the photoelectrons in direction parallel to the laser polarization.

Our discussion shows that for equal energy sharing, back-to-back emission oscillates between forbidden (for odd) and dominant (for even total photon numbers $N_{\text{XUV}} + N_{\text{IR}}$) as the number of effectively absorbed IR photon increases. This oscillation originates in dipole and selection parity selections rules [54, 56, 57].

6.1.4 Summary of Section 6.1

We investigated the IR laser-assisted XUV DI of helium based on a newly developed FE-DVR computer code for numerically solving the TDSE equation in full dimensionality.

We studied JADs separately for odd and even numbers of exchanged photons and for specific effective numbers of absorbed (and emitted) IR photons. We found that an assisting IR field retains some of the dominant features of the laser-free JADs while modifying the

distribution of DI yields in compliance with known dipole and parity selection rules. These modifications become more significant as the effective number of absorbed IR photons increases, in support of the intuitive picture of momentum transfer from the IR-laser field to the photo-emitted electrons in laser-polarization direction. In particular, we found that the IR pulse promotes side-by-side and enables back-to-back emission. For even numbers of absorbed (IR plus XUV) photons, the IR pulse was found to enable back-to-back emission and conic emission. This is in agreement with the dipole and parity selection rules that forbid (allow) back-to-back and conic emission for odd (even) total effective numbers of (IR plus XUV) photons, respectively.

6.2 Energy Sharing Dependence

In Sec. 6.1, we discussed the DI of helium at equal energy sharing and found the addition of a comparatively weak IR field to the ionizing XUV pulse leads to the appearance of characteristic sidebands in energy and angle distributions [46]. In this section we extend these investigations to nonequal energy sharing. We analyze JADs and MADs for XUV pulses with 10^{14} W/cm^2 peak intensity, $\tau_{\text{XUV}} = 1 \text{ fs}$ pulse duration, and $\hbar\omega_{\text{XUV}} = 89 \text{ eV}$ central photon energy that coincide with an assisting IR pulse with a peak intensity of $3 \times 10^{12} \text{ W/cm}^2$, pulse length $\tau_{\text{IR}} = 2.6 \text{ fs}$, and $\hbar\omega_{\text{IR}} = 1.61 \text{ eV}$ photon energy, as given by Eqn. (2.30).

We are going to compare angular distributions for equal and unequal energy sharing between the photoelectrons and distinguish contributions from even and odd effective numbers of photons involved for clarity. For even (odd) effective numbers we include one 89 eV XUV photon plus any odd (even) number of IR photons. We calculate these “even” and “odd” contributions to JADs and MADs by restricting the partial-wave expansion of the time-dependent wave function for the helium atom Eqn. (2.40) in the combined XUV and IR fields to even and odd values of the total angular momentum quantum number L . We compute the angular distributions discussed below by integrating joint energy distributions

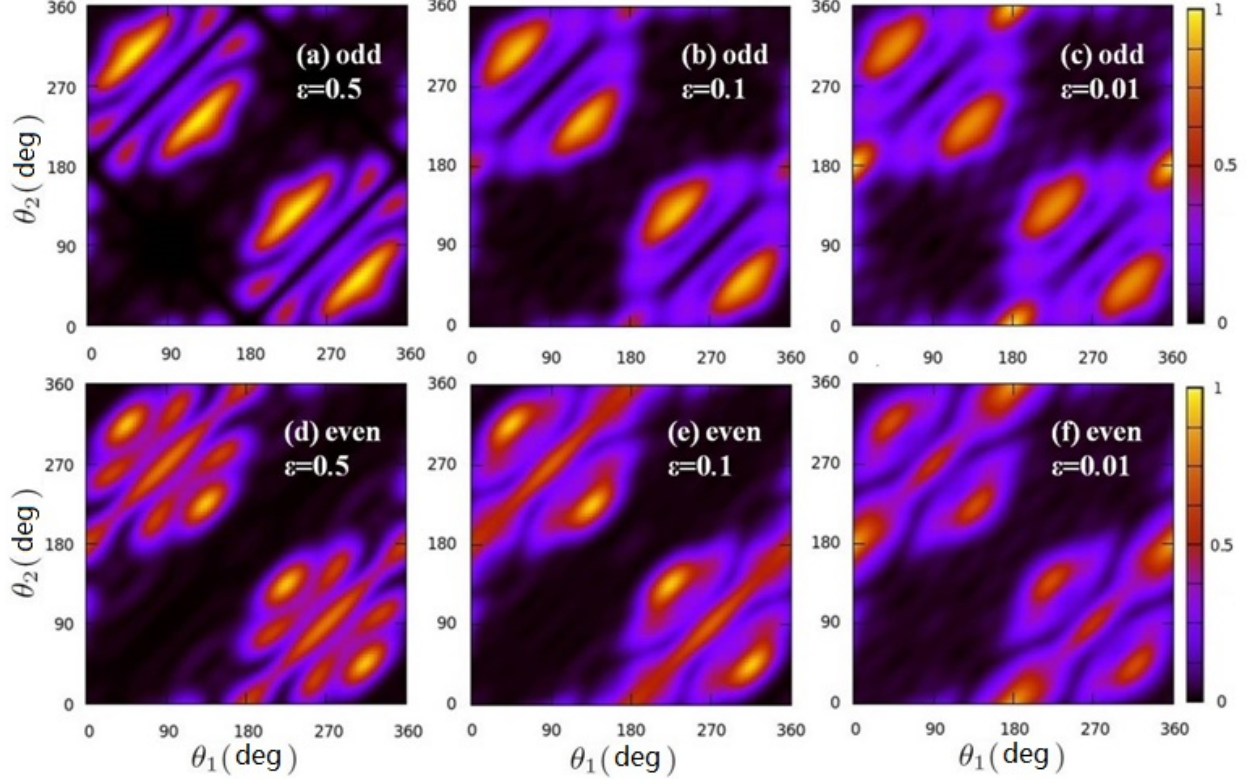


Figure 6.4: Calculated normalized joint angular distributions for IR laser-assisted single-XUV-photon double ionization of helium by $10^{14} W/cm^2$ peak intensity $\hbar\omega_{XUV} = 89$ eV XUV pulses assisted by coincident $3 \times 10^{12} W/cm^2$ IR-laser pulses. Contribution to the double-ionization yield from (a)-(c) odd and (d)-(f) even total effective numbers of XUV plus IR photons. Results for (a,d) equal energy sharing ($\varepsilon = 0.5$), (b,e) unequal energy sharing ($\varepsilon = 0.1$), and (c,f) extremely unequal energy sharing ($\varepsilon = 0.01$).

across along all sidebands (all possible energies E_1 and E_2) for a given value of the energy-sharing parameter ε .

6.2.1 Joint Angular Distributions

Figure 6.4 shows our calculated JADs for laser-assisted single-XUV-photon DI for the odd and even effective photon numbers in the top panel and bottom panel, respectively, for three different values of energy sharing. Even though side-by-side emission is possible at unequal energy sharing, no such contribution can be seen on the linear-scale graphs, regardless of the final-state parity.

For odd effective photon numbers (odd parity final states), the equal energy sharing distributions in Figs. 6.4 (a-c) have kept the four symmetrical-emission peaks which are the main features of single-photon DI without an assisting IR field [cf. Fig. 4.8]. As the energy symmetry is broken, symmetrical emission remains dominant at $\varepsilon = 0.1$ [Fig. 6.4 (b)] and small contribution from back-to-back emission emerge, as for the laser-free single-XUV-photon DI [cf. Fig. 4.8 (b)]. For extremely unequal energy sharing at $\varepsilon = 0.01$ [Fig. 6.4 (c)], both symmetric and back-to-back emission are prominent in the JAD. However, in contrast to the laser-free DI [cf. Fig. 4.8 (c)], the peak DI yield for back-to-back exceeds the peak yields for symmetric emission. For odd parity final states and unequal energy sharing, a striking change induced by the assisting laser pulse is thus the promotion of back-to-back emission.

Contributions to the JAD from even effective photon numbers (even parity final states) show competing symmetrical and back-to-back emission over a large range of energy sharing. These main contributors to DI in Fig. 6.4 (d-f) are the same as for laser-free DI by two 45 eV photons [cf. Fig. 4.19], albeit with very different relative yields. Unlike laser-free even-parity DI by two 45 eV photons, our even-photon-number results in Fig. 6.4 (d-f) are sensitive to changes in the energy sharing. Interestingly, while at equal energy sharing back-to-back emission is strictly prohibited for single-photon DI, the absorption of an additional IR photon enables clearly noticeable back-to-back emission [Fig. 6.4 (d)].

6.2.2 Mutual Angular Distributions

Figure 6.5 shows MADs for the laser-assisted single-XUV-photon DI. All distributions are normalized to the enclosed area and extracted from the corresponding JADs shown in Fig. 6.4 according to Eqn. (2.79).

For odd total effective numbers of XUV plus IR photons (odd parity), side-by-side ($\theta_{12} = 0^\circ$) and back-to-back emission ($\theta_{12} = 180^\circ$) are strictly forbidden at equal energy sharing [Fig. 6.5 (a)]. For unequal energy sharing, both side-by-side and back-to-back emission (red

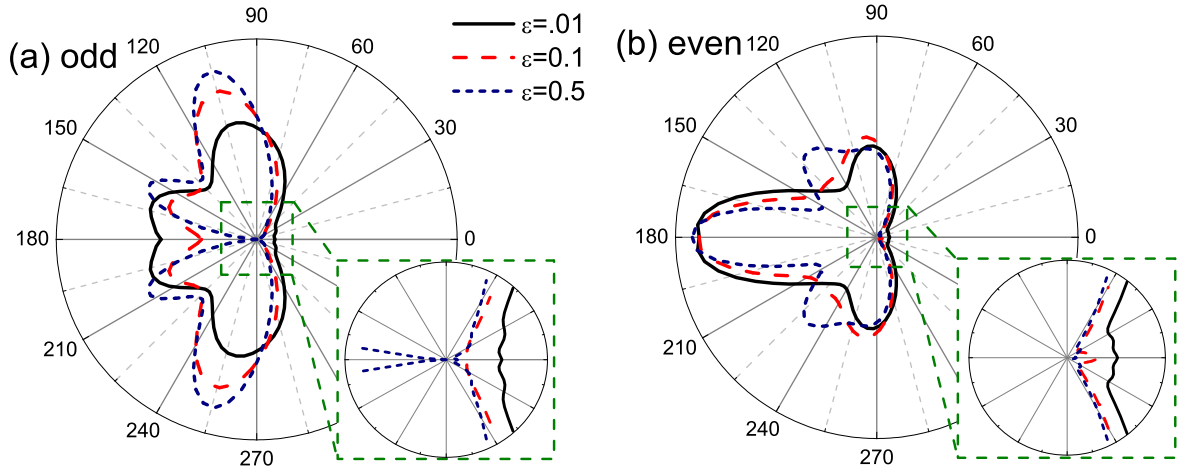


Figure 6.5: Mutual angular distributions for IR-laser-assisted single-XUV-photon double ionization of helium for different energy sharings ε . (a) Contributions to the double-ionization yield from (a) odd and (b) even total effective numbers of XUV plus IR photons. The XUV and IR pulse parameters are the same as in Fig. 6.4. The insets zoom into the distributions near the mutual angles $\theta_{12} = 0^\circ$ and 180° .

dashed line) occur and become increasingly prominent with increasing energy asymmetry. For extremely unequal energy sharing ($\varepsilon = 0.01$), the back-to-back-emission yield reaches $\approx 80\%$ of the peak value at $\Theta_{12} \approx 105^\circ$, while the side-by-side-emission yield reaches $\approx 15\%$ of the peak value.

For even parity back-to-back emission strongly dominates the MADs in Fig. 6.5 (b), regardless of the energy sharing. The side-by-side-emission yields remain very small at unequal energy sharing ($\varepsilon = 0.1$) and are largest at extremely unequal energy sharing ($\varepsilon = 0.01$). The small but noticeable side-by-side-emission yield at $\varepsilon = 0.01$ is compatible with a two-step mechanism. This mechanism operates by the fast photoelectron carrying away almost the entire excess energy, while the slow electron reverses its motion by absorbing one IR photon to follow the fast electron. This picture thus explains noticeable side-by-side contributions by allowing the electrons to initially move in opposite directions, i.e., along the strongly favored back-to-back emission directions, while being compatible with dipole selection rules that would prohibit side-by-side emission without an assisting IR-laser pulse.

Figure 6.6 depicts the schematic of laser splitting the emission peaks and enabling the

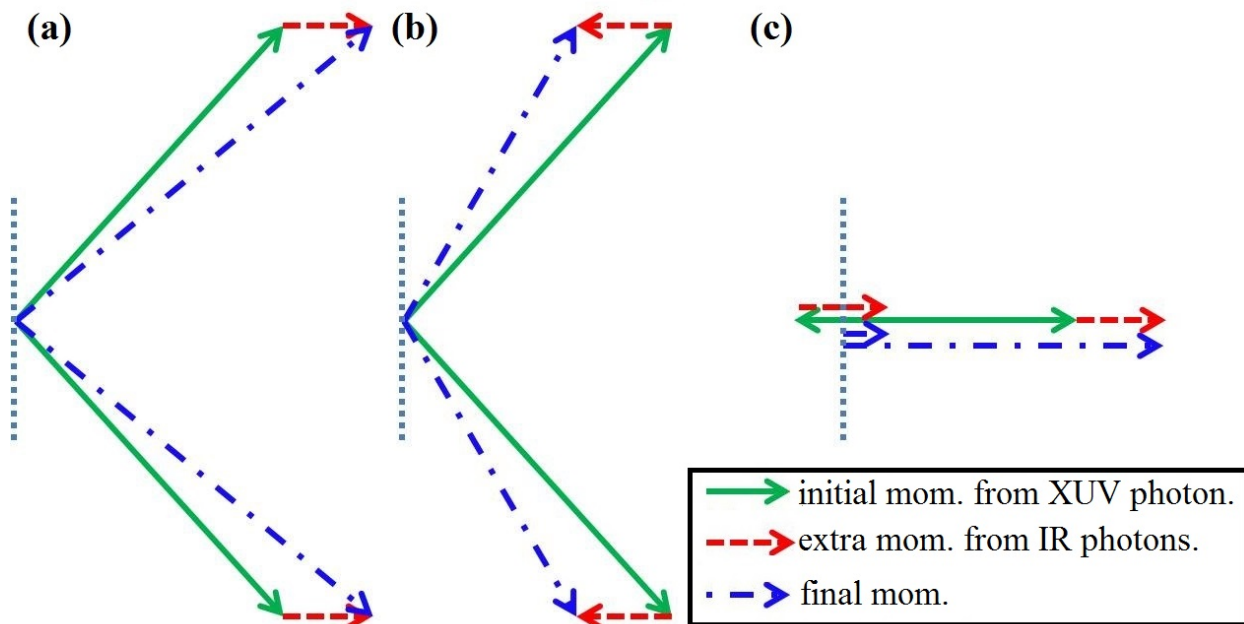


Figure 6.6: Schematics of laser controlled DI. (a) Shift to side by side emission; (b) shift to back-to-back emission, and (c) enabling the side-by-side emission. The green solid lines stand for the momentum without laser assistance. The red dashed lines stand for the extra momentum obtained from the laser field. The momenta are plotted in blue dotted dashed lines.

parallel emissions. Fig. 6.6(a,b) displays how the laser controls the photoelectrons shift to parallel/anti-parallel emissions, respectively. The DI photoelectrons gain initial energy by absorbing one XUV photon, and propagate in the laser field. The laser field can streak the photoelectrons, and these electrons can obtain equal amounts of extra energies and momenta. These momenta can be parallel (a) or antiparallel (b) to the electric field. In the case (a), initial and extra momenta both point to the left, the angle difference of their total momenta therefore decreases, which means the photoemission shifts to side-by-side emission. On the other hand, panel (b) displays the photoemission shifting to back-to-back emission. Panel (c) depicts how the laser can enable side-by-side emission. The initial momenta of the two electrons are asymmetrical. One electron takes almost all the energy, while the other takes little. Because of correlation, the two photoelectrons go in opposite directions. When the IR laser is added, both electrons obtain extra momenta, as shown in panel (c), both pointing to right. Since the extra momentum is greater than the smaller initial momentum, the momentum of this electron will therefore be turned 180° , the same as the other electron. Since back-to-back emission is relatively strong only in the extremely unequal energy sharing cases, side-by-side emission is also observable for small energy sharing.

In order to more clearly display the enhancement of side-by-side and back-to-back emission by the assisting IR-laser pulse and to show this effect on observable MADs (including odd and even parity contributions), we compare in Fig. 6.7 MADs for single-XUV-photon DI of helium with and without the assisting IR-laser field at different energy sharing. To allow a quantitative comparison, the distributions in Fig. 6.7 are not individually, normalized, in contrast to the MADs shown in Fig. 6.5.

This comparison shows that each peak in the MADs for IR-laser-free DI splits into two peaks in the presence of the weak IR-laser field. This splitting of the dominant emission angles is due to momentum transfers from the IR field. Absorbing equal amounts of energy from the IR field, photoelectrons released by the XUV field are thus pushed either towards the side-by-side or back-to-back emission direction. At equal energy sharing [Fig. 6.7 (b)],

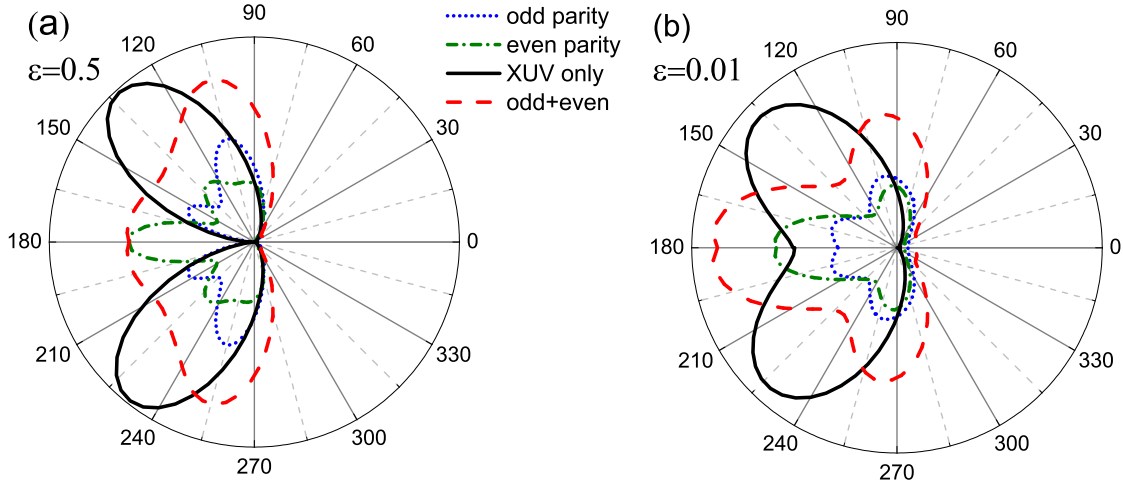


Figure 6.7: Contributions to the mutual angular distributions for IR-laser-assisted single-XUV-photon double ionization of helium for (a) equal energy sharing and (b) extremely unequal energy sharing with $\varepsilon = 0.01$. XUV- and IR-pulse parameters are the same as in Fig. 6.4. The black solid curves correspond to XUV-pulse-only results, blue dotted lines to odd parity, and green dash-dotted lines display even parity. The red dashed curves show coherent additions of odd and even parity contributions.

this momentum transfer changes the dominant relative emission angle from $\Theta_{12} \approx 130^\circ$ for IR-laser-free emission to $\approx 105^\circ$ and $\approx 170^\circ$ for IR-laser-assisted emission. For extremely unequal energy sharing [Fig. 6.7 (a)], the dominant relative emission angle splits from $\approx 135^\circ$ for IR-laser-free emission to $\approx 95^\circ$ and $\approx 170^\circ$ for IR-laser-assisted emission.

The dominant mutual angles for the even-parity contributions are $\approx 130^\circ$ and $\approx 180^\circ$ for equal, and $\approx 95^\circ$ and $\approx 170^\circ$ for extremely unequal energy sharing (Fig. 6.7). For odd parity final states the dominant relative angles can be estimated by vector addition. For equal energy sharing ($E_1 = E_2 = 5$ eV), the dominant photoelectron momentum vector (in plane polar coordinates), $(k_1, \Theta_{12}) = (0.606, 130^\circ)$, changes upon absorption of an IR photon by $\pm(A_{0,IR}, 0)$ where $A_{0,IR} \approx 0.156$ is the peak amplitude of the vector potential at 3×10^{12} W/cm² peak intensity of the IR pulse. This vector addition results in estimated dominant mutual angles for IR-laser-assisted emission of $\Theta_{12} = 106^\circ$ and 159° , in good agreement with the numerical results in Fig. 6.7 (a).

We note that for even parity (i.e., absorption of one XUV, assisted by an odd number of

IR photons) the exchange of IR photons results in final states that include contributions from different total angular momenta, e.g., $L = 0, 2$ if one IR photon is absorbed. Due to this coherent superposition of states with different symmetry, the simple addition of electron momenta and IR vector potential does not explain the dominant angles for even-parity contributions to laser-assisted XUV DI.

6.2.3 Conclusion of Section 6.2

We analyzed the dependance of joint and mutual photoelectron angular distributions on the energy sharing of the emitted electrons for the double ionization of helium atoms by short XUV pulses in co-planar emission geometry with and without the presence of a comparatively weak IR-laser pulse. Compared to the laser-free single-XUV-photon DI of helium, we found that the presence of a weak IR field can dramatically change the JAD of the two escaping electrons, leading to (i) angular shifts and a splitting into two dominant emission directions, (ii) strong enhancement of back-to-back emission at all energy sharings, and (iii) enhanced side-by-side emission yields at extremely unequal energy sharing.

These IR-pulse-induced changes in photoelectron angular distributions illustrate known constraints imposed by dipole selection rules. They are robust over a large range of energy sharings between the emitted electrons, and, for special cases, can be classically estimated by simple vector addition, based on the transfer of IR-photon momenta to photoelectrons.

6.3 Intensity Dependence

Figure 6.8 displays the joint energy distributions (JEDs) of the laser-assisted DI at different laser intensities. The left panels are JEDs for odd parity, and the right panels show JEDs for even parity. The top-left graph shows the laser-free JED. From top to bottom, the IR intensities are 0, 10^{10} , 10^{11} and 10^{12} W/cm², respectively. With increasing IR-laser intensity, the odd-parity probability density in the JEDs decreases, while the even-parity probability density increases. This means that assisted by a weak IR-laser field, the DI yield does not

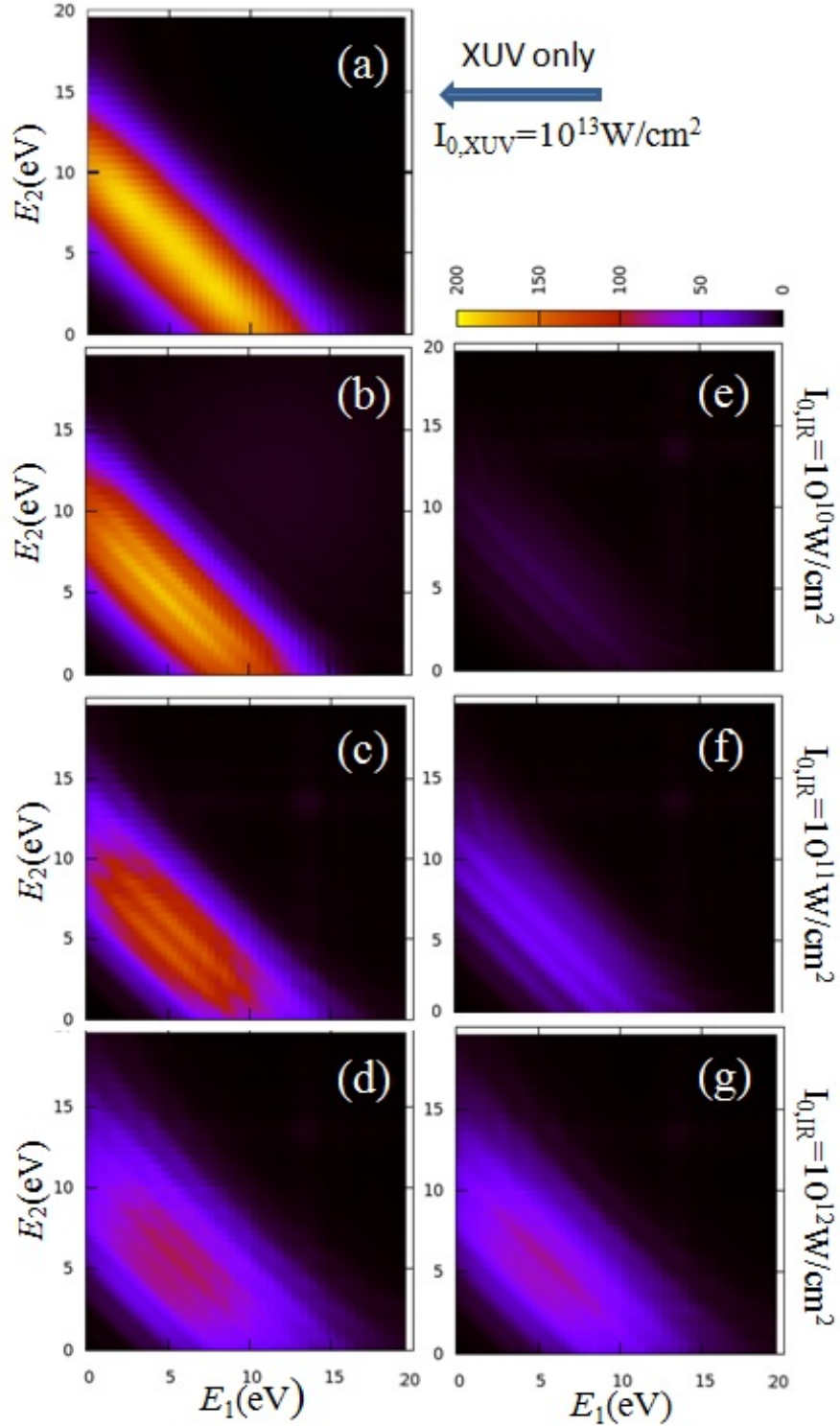


Figure 6.8: Intensity dependence of JEDs. Panel (a) is laser-free result for comparison. (a-d) are JEDs with odd parity, and (e-g) are JEDs with even parity, respectively.

change a lot. The odd-parity and even-parity photoelectrons are competing. Stronger IR fields can boost the even-parity photoelectrons. At the intensity 10^{12} W/cm², the odd-parity and even-parity probability densities are comparable in magnitude. However, if we keep increasing the IR-laser intensity, e.g. to 10^{13} W/cm², the DI-probability increases due to the strong IR-laser field can be significant, and many-photon process will be important or even dominant. Since we would have to employ many more partial waves to describe such a process, no numerical results for stronger assisted IR field are shown in this thesis, the numerical effort being significant and requiring access to computational resource that are not locally available to us.

6.3.1 Conclusions of Section 6.3

We have studied the control of electrons emission in XUV DI of helium by short IR laser pulses. By changing the laser intensity, we can turn on and off back-to-back emission and side-by-side emission.

Chapter 7

Conclusions and Outlook

7.1 Summary and Conclusions

We have developed a set of codes to simulate and analyze single and double photo-ionization of helium atoms. These codes are based on the implementation of the TDCC and FE-DVR methods, and are validated by comparison with published experimental and theoretical results, and by assessing the convergence in the number of included angular momentum eigen-states, propagation time, and numerical grid size.

We studied sequential and non-sequential contributions to the TPDI of helium. We calculated photoelectron angular distributions by applying the FE-DVR method to solve *ab initio* TDSE for helium exposed to the electric field of an ultrashort XUV pulse. We found that forward-backward asymmetries of two-photoelectron angular distributions constitute an appropriate measure for the distinction between sequential and non-sequential DI contributions. We confirmed this link between the forward-backward asymmetry and the sequential DI contribution for central pulse energies below I_2 by matching the pulse-length-dependent profile of our *ab initio* calculated forward-backward asymmetry with an intuitively appealing heuristic formula for the square root of the SDI fraction.

We also investigated the IR-laser-assisted XUV DI of helium based on our newly developed FE-DVR computer code for numerically solving the TDSE in full dimensionality. We first focused on equal energy sharing of the emitted electron, where for side-by-side emission

convergence in the propagation time is slowed by the Coulomb interaction of the emitted electrons and thus serves as a lower limit for the degree of convergence at different emission angles (and non-equal energy sharing). We classified the distinct back-to-back, side-by-side, conic, and symmetric double emission modes in JADs at equal energy sharing, and discussed their prominence and absence for sequential and non-sequential DI upon absorption of up to three XUV photons and with and without the presence of an assisting IR laser field.

We discussed JADs separately for odd and even numbers of exchanged photons and for specific effective numbers of absorbed (and emitted) IR photon. We found that an assisting IR field retains some of the dominant features of the laser-free JADs while modifying the distribution of DI yields in compliance with known dipole and parity selection rules. These modifications become more significant as the effective number of absorbed IR photons increases, in support of the intuitive pictures of momentum transfer from the IR-laser field to the photo-emitted electrons in laser-polarization direction. In particular, we found that the IR pulse promotes side-by-side and enables back-to-back emission. For even numbers of absorbed (IR plus XUV) photons, the IR pulse was found to enable back-to-back emission and conic emission. This is in agreement with the dipole and parity selection rules that forbid (allow) back-to-back and conic emission for odd (even) total effective numbers of (IR plus XUV) photons, respectively.

We analyzed the dependance of joint and mutual photoelectron angular distributions on the energy sharing of the emitted electrons for the double ionization of helium atoms by short XUV pulses in co-planar emission geometry with and without the presence of a comparatively weak IR-laser pulse. Compared to the laser-free single-XUV-photon DI of helium, we found that the presence of a weak IR field can dramatically change the JADs of the two escaping electrons, leading to (i) angular shifts and a splitting into two dominant emission directions, (ii) strong enhancement of back-to-back emission at all energy sharing, and (iii) enhanced side-by-side emission yields at extremely unequal energy sharing.

These IR-pulse-induced changes in photoelectron angular distributions illustrate known

constraints imposed by dipole selection rules. They are robust over a large range of energy sharing between the emitted electrons, and, for special cases, can be classically estimated by simple vector addition, based on the transfer of IR-photon momenta to photoelectrons.

7.2 Challenges and Outlook

We discussed laser-assisted single-XUV-photon DI and our study connects to many more challenging problems. We plan to investigate the time-delay dependence DI induced by strong IR fields, and laser-assisted single-XUV-photon DI including transient doubly excited states. We also intend to apply our new code to systematically investigate the influence of the carrier-envelope phases of the XUV and IR pulse, the XUV-pulse length, and the delay between XUV and IR pulse have on the correlated electron dynamics during the DI process.

The transient absorption experimental results [10] are a significant numerical challenge when we consider the IR pulse lengths and XUV-IR delay range in typical experiments [10, 108]. In such experiments, they use very long pulse durations (~ 10 fs) and large time delays (up to ~ 40 fs) between the XUV and IR pulses. Both long pulse durations and large time delays are challenge to numerical simulation on current computational resources.

Nowadays, the optimization with graphics processing unit (GPU) as an emerging high-performance computing platform, has been introduced to physics [36]. The GPU-based optimization is available in many supercomputers, such as Edison at NERSC [63], Titan at OLCF [69, 107]. Although GPU-based optimization and Many-Integrated-Core Architecture (MIC) [107] of Intel®Xeon Phi™ Coprocessors can be applied to accelerate the computation, it is still difficult for us to solve our problems above. We have to seek for optimization schemes other than through hardware, as discussed in the two following subsections.

7.2.1 *L*-Shaped Grid

For DI, we often need to keep both radial coordinates equal. However, when we consider only single ionization of helium, where one electron remains bound to the nucleus core,

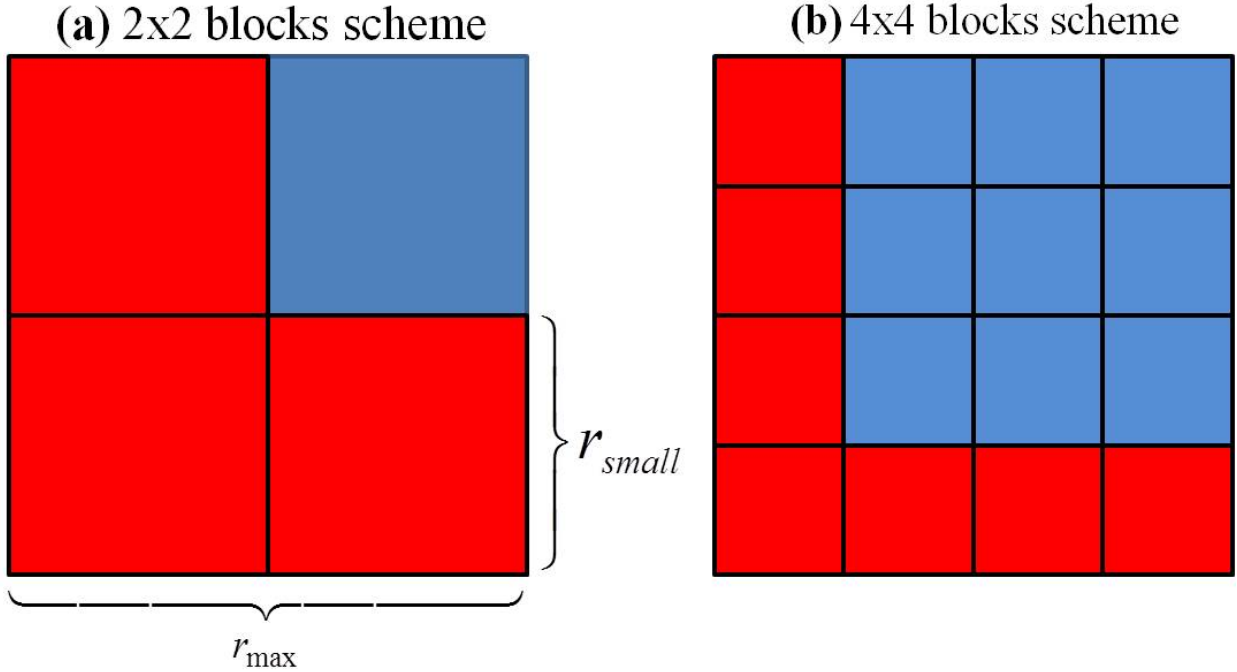


Figure 7.1: L -shaped grid. Panel (a): 2×2 blocks. Panel (b): 4×4 blocks. The red blocks form the L -shaped grid, the blue blocks are truncated, because the two electron radial probability densities in these regions are negligible for single ionization process.

we can use an L -shaped grid. In such a grid, we assign no points to the wave function where both r_1 and r_2 exceed some value r_{small} . For example, in Fig. 7.1(a), we set $r_{\text{small}} = r_{\text{max}}/2$ and reduce the computational efforts by 25%. If we set $r_{\text{small}} = r_{\text{max}}/4$, as shown in Fig. 7.1(b), we can reduce the computational efforts by up to 56.25%.

The L -shaped grid is convenient in distributed-memory parallel computing. We can assign the small blocks to different nodes, such that only a few ghost points need to be communicated between different computing nodes.

7.2.2 Further Reducing the Number of Partial Waves

Although selection rules and symmetries, as discussed in Chap. 4.2, can eliminate irrelevant partial waves and largely reduce the number of partial waves we used in solving the TDSE, the number of partial waves is still too large to numerically solve TDSE if there are many photons involved in a process. For example, when $(L_{\text{max}}, l_1^{\text{max}}, l_2^{\text{max}}) = (6, 6, 6)$, we have to

use 106 partial waves. This number currently is at the limit of our local current computing resources. If we need to consider DI in an IR laser field, to make sure the result is converged, we would have to use at least the configuration $(L_{max}, l_1^{max}, l_2^{max}) = (30, 30, 30)$ [34], which requires about 8,000 (or 5,000 without symmetry redundancy) partial waves. It is impossible for us to perform such simulations in the near future; neither with local resources nor at supercomputer centers, e.g., NERSC [63] and OLCF [69]. So we need to reduce the number of partial waves effectively, without significantly sacrificing accuracy.

Due to electron-electron correlation, the ground state of helium can be expanded in configurations according to $|1S\rangle = c^{(0)}|ss\rangle + c^{(1)}|pp\rangle + c^{(2)}|dd\rangle + c^{(3)}|ff\rangle + \dots$, and $|c^{(0)}| \gg |c^{(1)}|$. For DI, the dominant component is the $|ss\rangle$ state, but the remaining components $|pp\rangle$, $|dd\rangle$ and $|ff\rangle$ also play important roles in detailed structure of angular distribution [119]. Partial waves with even higher angular momenta [l_1 (or l_2) ≥ 4] are neglected in most of our calculations for single-photon DI and two-photon DI.

For excited states, different partial waves play different roles. In Fig. 7.2, we display the probability distributions versus the partial waves, extracted from the final-state wave function for DI at the end of the 1-fs 42 eV XUV pulse. Different L 's are plotted in different colors: $L=0$ in black, $L=1$ in red, $L=2$ in blue and $L=3$ in purple. As expected, the $(0, 0, 0)$ partial wave is dominant. To better view the wave functions for four partial waves with $L=0$, we plot the probability densities of the four wave functions in Fig. 7.3. In Fig. 7.3 (a), there is a large overlap with the ground-state wave function (see Fig. 4.2). This means that two electrons mostly stay in the ground state due to the relatively “weak” XUV field. Besides the component overlapping with the ground state, there are also “DI” and/or “doubly excited” components: the wave function with $r_1 > 10$ and $r_2 > 10$. Other than this $(0, 0, 0)$ partial wave, the other three partial waves with $L=0$ show “DI” and/or “doubly excited” components [$r_1(r_2) > 10$]. The second strongest partial waves are $(1, 0, 1)$ and $(1, 1, 0)$. This is due to the one-photon process, singly ionization of helium by 42 eV XUV photon. The next strongest component is $(0, 1, 1)$. It could be from either the initial ground

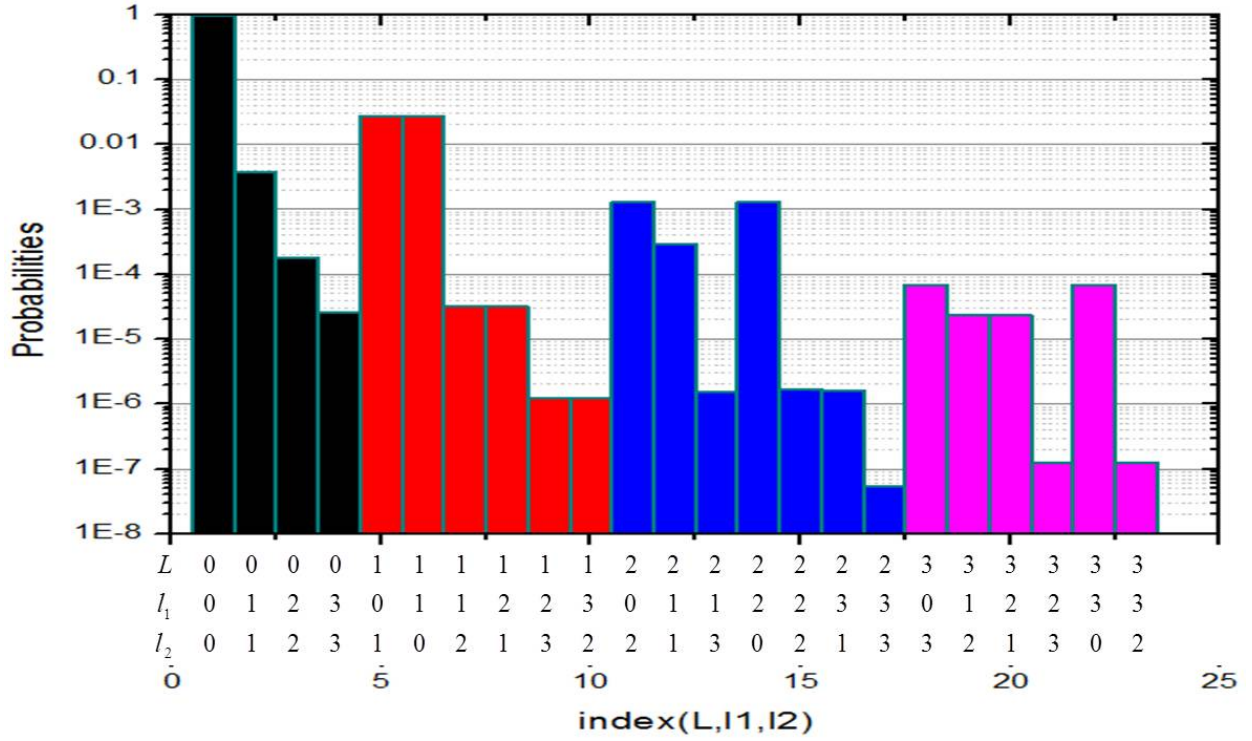


Figure 7.2: Histogram of the probability-density distribution of partial waves in 42 eV XUV photon TPDI. The x-axis lists partial waves configurations (L, l_1, l_2) and corresponding index numbers for each partial wave. Different L values are plotted in different color: $L=0$ in black, $L=1$ in red, $L=2$ in blue and $L=3$ in purple. The $(0, 0, 0)$ partial wave corresponds to the $|ss\rangle$ state, it approximates 1. XUV pulse parameters: 5×10^{14} W/cm², and 1-fs pulse duration.

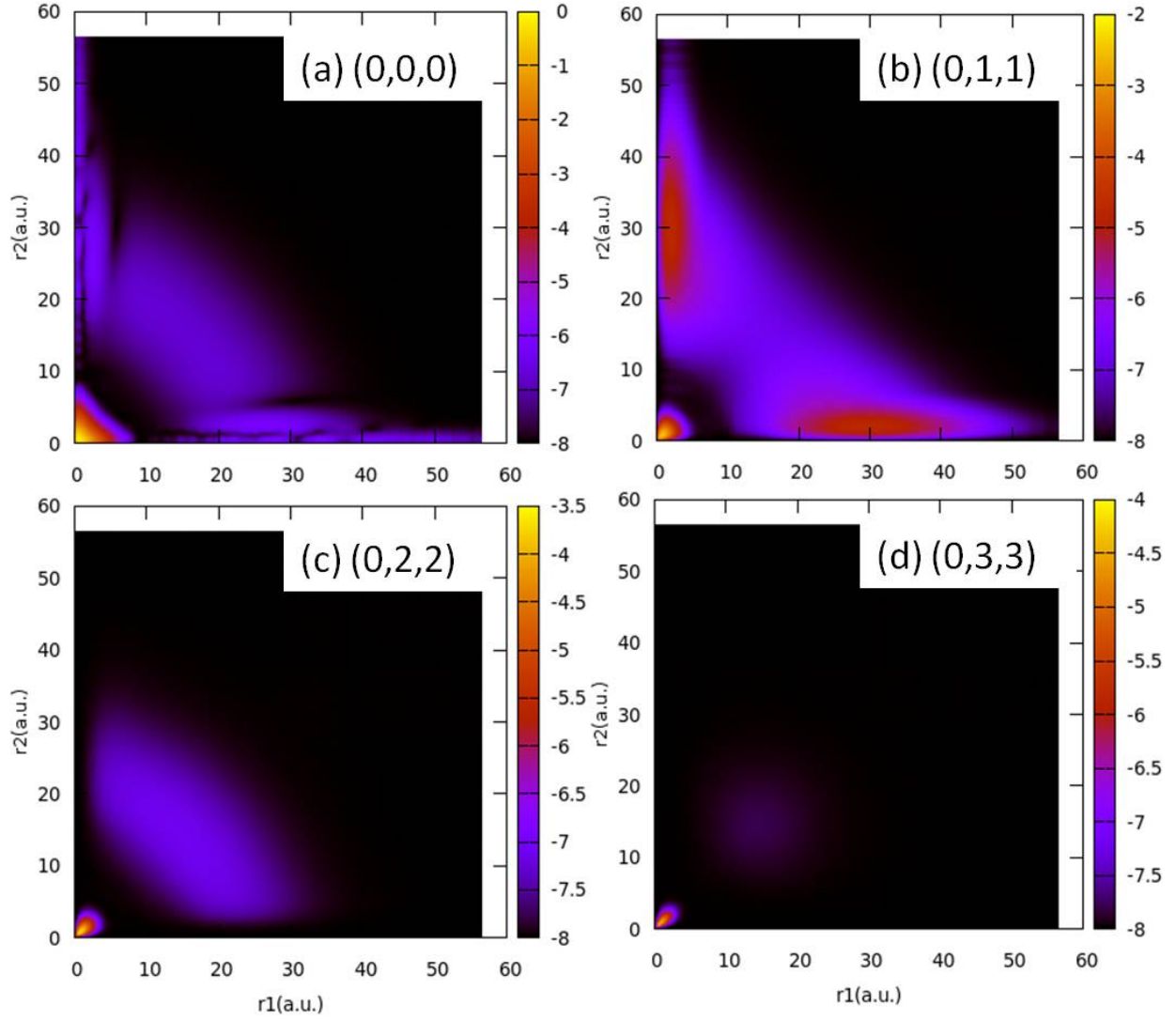


Figure 7.3: The probability densities of 4 partial waves with $L = 0$ in TPDI by single 1-fs duration XUV pulse with 42 eV central energy. The color scales are different in each panel. The $(0, 0, 0)$ partial wave is the most important component, it indicates that most electrons stay in ground state. With increasing l_1/l_2 , the probability densities decrease. These graphs agree with the results shown in Fig. 7.2.

state or the two-photon DI process. The next important partial waves are $(2, 0, 2)$, $(2, 2, 0)$ and $(2, 1, 1)$. They are the strongest DI contributions, not counting the $L=0$ components which overlap with ground state. Compared to these partial waves, some partial waves are very low in probability amplitude. For instance, the $(2, 3, 3)$ partial wave has a probability amplitude less than 10^{-7} , and the partial waves $(3, 2, 3)$ and $(3, 3, 2)$ are a little above 10^{-7} . So they are negligible in our simulation, and we can truncate them. If we only consider the partial waves with probabilities higher than 10^{-5} , we can truncate 8 partial waves from 23 partial waves in total. This is true even when the photon number is large [34]. Actually, in Hu's simulation, only 381 partial waves are needed in the configuration $(30, 30, 30)$ to describe the atto-second boosted IR-laser DI of helium [34]. Thus, this truncation would make it possible to apply our newly developed code to examine DI of helium by intense IR pulse with intensities of about 10^{16} W/cm² by using Titan at OLCF [69].

Bibliography

- [1] M. Abramowitz, I. Stegun, *Handbook of Mathematical Functions (with Formulas, Graphs, and Mathematical Tables)*, (Dover, Mineola, New York, 1972).
- [2] S. A. Alexander, S. Datta, and R. L. Coldwell. Lowest-order relativistic corrections of helium computed using Monte Carlo methods. *Phys. Rev. A* **81**, 032519 (2010).
- [3] L. Avaldi and A. Huetz. Photodouble ionization and the dynamics of electron pairs in the continuum. *J. Phys. B: At. Mol. Opt. Phys.* **38**, S861 (2005).
- [4] H. Bachau. Theory of two-photon double ionization of helium at the sequential threshold. *Phys. Rev. A* **83**, 033403 (2011).
- [5] A. R. Barnett. The calculation of spherical bessel and Coulomb functions. in *Computational Atomic Physics*, edited by K. Bartschat (Springer, Heidelberg, New York, 1996), Chap.9, p. 181.
- [6] H. Bräuning, R. Dörner, C. L. Cocke, M. H. Prior, B. Krässig, A. S. Kheifets, I. Bray, A. Bräuning-Demian, K. Carnes, S. Dreuil, V. Mergel, P. Richard, J. Ullrich, and H. Schmidt-Böcking. Absolute triple differential cross sections for photo-double ionization of helium - experiment and theory. *J. Phys. B: At. Mol. Opt. Phys.* **31**, 5149 (1998).
- [7] M. Brauner, J. S. Briggs, and H. Klar. Triply-differential cross sections for ionisation of hydrogen atoms by electrons and positrons. *J. Phys. B: At. Mol. Opt. Phys.* **22**, 2265 (1989).
- [8] J. S. Briggs and V. Schmidt. Differential cross sections for photo-double-ionization of the helium atom. *J. Phys. B: At. Mol. Opt. Phys.* **33**, R1 (2000).
- [9] Z. Chang. *Fundamentals of attosecond Optics*. CRC Press, Boca Raton, FL, 2011.

- [10] M. Chini, B. Zhao, H. Wang, Y. Cheng, S. X. Hu, and Z. Chang. Subcycle ac Stark shift of helium excited states probed with isolated attosecond pulses. *Phys. Rev. Lett.* **109**, 073601 (2012).
- [11] J. Colgan and M. S. Pindzola. Core-excited resonance enhancement in the two-photon complete fragmentation of helium. *Phys. Rev. Lett.* **88**, 173002 (2002).
- [12] R. Dörner, Th. Weber, M. Weckenbrock, A. Staudte, M. Hattass, R. Moshhammer, J. Ullrich, and H Schmidt-Böcking. Multiple ionization in strong laser fields. *Adv. At. Mol. Opt. Phys.* **48**, 1 (2002).
- [13] F. J. Duarte. *Tunable Lasers Handbook*. Academic, New York (1995).
- [14] N. Elander and E. Yarevsky. Exterior complex scaling method applied to doubly excited states of helium. *Phys. Rev. A* **57**, 3119 (1998).
- [15] J. Emsley. *Nature's Building Blocks*. Oxford University Press, Oxford (2001).
- [16] U. Fano. Effects of configuration interaction on intensities and phase shifts. *Phys. Rev.* **124**, 1866 (1961).
- [17] J. M. Feagin. Wannier threshold theory for the Coulomb break-up of three-particle systems. *J. Phys. B: At. Mol. Opt. Phys.* **17**, 2433 (1984).
- [18] J. Feist, S. Nagele, R. Pazourek, E. Persson, B. I. Schneider, L. A. Collins, and J. Burgdörfer. Nonsequential two-photon double ionization of helium. *Phys. Rev. A* **77**, 043420 (2008).
- [19] J. Feist, S. Nagele, R. Pazourek, E. Persson, B. I. Schneider, L. A. Collins, and J. Burgdörfer. Probing electron correlation via attosecond XUV pulses in the two-photon double ionization of helium. *Phys. Rev. Lett.* **103**, 063002 (2009).
- [20] J. Feist. Two-photon double ionization of helium. *PhD thesis*. Technischen Universität Wien (2009).

- [21] M. Førre, S. Selstø, and R. Nepstad. Nonsequential two-photon double ionization of atoms: identifying the mechanism. *Phys. Rev. Lett.* **105**, 163001 (2010).
- [22] B. Feuerstein, R. Moshhammer, D. Fischer, A. Dorn, C. D. Schröter, J. Deipenwisch, J. R. Crespo Lopez-Urrutia, C. Höhr, P. Neumayer, J. Ullrich, H. Rottke, C. Trupp, M. Wittmann, G. Korn, and W. Sandner. Separation of recollision mechanisms in nonsequential strong field double ionization of Ar: the role of excitation tunneling. *Phys. Rev. Lett.* **87**, 043003 (2001).
- [23] P. S. Ganas and A. E. S. Green. Electron impact excitation of the rare gases. *Phys. Rev. A* **4**, 182 (1971).
- [24] R. G. Gould. The LASER, Light Amplification by Stimulated Emission of Radiation. In Franken, P.A. and Sands, R.H. (Eds.). *The Ann Arbor Conference on Optical Pumping, the University of Michigan, 15 June through 18 June 1959*. p. 128. (1959).
- [25] A. E. S. Green, D. L. Sellin, and A. S. Zachor. Analytic independent-particle model for atoms. *Phys. Rev.* **184**, 1 (1969).
- [26] X. Guan, O. Zatsarinny, K. Bartschat, B. I. Schneider, J. Feist, and C. J. Noble. General approach to few-cycle intense laser interactions with complex atoms. *Phys. Rev. A* **76**, 053411 (2007).
- [27] X. Guan, K. Bartschat, and B. I. Schneider. Dynamics of two-photon double ionization of helium in short intense XUV laser pulses. *Phys. Rev. A* **77**, 043421 (2008).
- [28] X. Guan. The Lobatto basis in finite-element DVR method. *private communication*.
- [29] A. Huetz, P. Selles, D. Waymel, and J. Mazeau. Wannier theory for double photoionization of noble gases. *J. Phys. B: At., Mol. Opt. Phys.* **24**, 1917 (1991).
- [30] H. Hasegawa, E. J. Takahashi, Y. Nabekawa, K. L. Ishikawa, and K. Midorikawa.

- Multiphoton ionization of He by using intense high-order harmonics in the soft-x-ray region. *Phys. Rev. A* **71**, 023407 (2005).
- [31] F. He, C. Ruiz, A. Becker, and U. Thumm. Attosecond probing of instantaneous ac Stark shifts in helium atoms. *J. Phys. B: At. Mol. Opt. Phys.* **44**, 211001 (2011).
- [32] D. A. Horner, F. Morales, T. N. Rescigno, F. Martín, and C. W. McCurdy. Two-photon double ionization of helium above and below the threshold for sequential ionization. *Phys. Rev. A* **76**, 030701(R) (2007).
- [33] S. X. Hu. Optimizing the FEDVR-TDCC code for exploring the quantum dynamics of two-electron systems in intense laser pulses. *Phys. Rev. E* **81**, 056705 (2010).
- [34] S. X. Hu. Boosting Photoabsorption by Attosecond Control of Electron Correlation. *Phys. Rev. Lett.* **111**, 123003 (2013).
- [35] W. R. Johnson. *Atomic Structure Theory: Lectures on Atomic Physics* (Springer, Berlin, Heidelberg, New York, 2007), Chap. 4, p. 126.
- [36] X. Jia, P. Ziegenhein and S. B. Jiang. GPU-based high-performance computing for radiation therapy. *Phys. Med. Biol.* **59**, R151 (2014).
- [37] W. C. Jiang, L. Y. Peng, W. H. Xiong, and Q. Gong. Comparison study of electron correlation in one-photon and two-photon double ionization of helium. *Phys. Rev. A* **88**, 023410 (2013).
- [38] A. S. Kheifets and I. Bray. Application of the CCC method to the calculation of helium double-photoionization triply differential cross sections. *J. Phys. B: At. Mol. Opt. Phys.* **31** L447 (1998).
- [39] A. S. Kheifets and I. Bray. Symmetrized amplitudes of the helium-atom double photoionization. *Phys. Rev. A* **65**, 022708 (2002).

- [40] A. S. Kheifets and I. A. Ivanov. Convergent close-coupling calculations of two-photon double ionization of helium. *J.Phys. B: At. Mol. Opt. Phys.* **39**, 1731 (2006).
- [41] M. Yu. Kuchiev. Atomic antenna. *Pis'ma Zh. Eksp. Teor. Fiz.* **45**, 319 (1987) [JETP Lett. **45**, 404 (1987)].
- [42] A. L'Huillier, L. A. Lompre, G. Mainfray, and C. Manus. Multiply charged ions formed by multiphoton absorption processes in the continuum. *Phys. Rev. Lett.* **48**, 1814 (1982).
- [43] A. L'Huillier, L. A. Lompre, G. Mainfray, and C. Manus. Multiply charged ions induced by multiphoton absorption in rare gases at 0.53 μm . *Phys. Rev. A* **27**, 2503 (1983).
- [44] J. C. Light, Z. Bacic. Adiabatic approximation and nonadiabatic corrections in the discrete variable representation - highly excited vibrational-states of triatomic-molecules. *J. Chem. Phys.* **87**, 4008 (1987).
- [45] J. V. Lill, G. A. Parker, J. C. Light. The discrete variable finite basis approach to quantum scattering, *J. Chem. Phys.* **85**, 900 (1986).
- [46] A. Liu and U. Thumm. Laser-assisted XUV few-photon double ionization of helium: joint angular distributions. *Phys. Rev. A* **89**, 063423 (2014).
- [47] A. Liu and S. Li. Relativistic electron scattering from a freely movable proton in a strong laser field. *Phys. Rev. A* **90**, 055403 (2014).
- [48] A. Liu and U. Thumm. Laser-assisted XUV double ionization of helium: Energy-sharing dependence of joint angular distributions. *Phys. Rev. A* **91**, 043416 (2015).
- [49] A. Liu and U. Thumm. A criterion for distinguishing sequential from non-sequential contributions to the double ionization of helium in ultrashort XUV pulses. *Submitted to Phy. Rev. Lett.*

- [50] L. B. Madsen, L. A. A. Nikolopoulos, T. K. Kjeldsen, and J. Fernández. Extracting continuum information from $\Psi(t)$ in time-dependent wave-packet calculations. *Phys. Rev. A* **76**, 063407 (2007).
- [51] G. D. Mahan. *Many-particle physics (Third Edition)*. Kluwer Academic/Plenum Publishers, New York (2000).
- [52] D. E. Manolopoulos and R. E. Wyatt. Quantum scattering via the log derivative version of the kohn variational principle. *Chem. Phys. Lett.* **152**, 23 (1988).
- [53] W. C. Martin. Energy levels of neutral helium ($^4\text{He I}$). *J. Phys. Chem. Ref. Data* Vol. **2**, No. 2 (1973).
- [54] F. Maulbetsch and J. S. Briggs. Angular distribution of electrons following double photoionization. *J. Phys. B: At. Mol. Opt. Phys.* **26**, 1679 (1993).
- [55] F. Maulbetsch and J. S. Briggs. Double photoionization in the case of unequal energy sharing. *J. Phys. B: At. Mol. Opt. Phys.* **27**, 4095 (1994).
- [56] F. Maulbetsch and J. S. Briggs. Selection rules for transitions to two-electron continuum states. *J. Phys. B: At. Mol. Opt. Phys.* **28**, 551 (1995).
- [57] F. Maulbetsch, M. Pont, J. S. Briggs, and R. Shakeshaft. Angular distributions for double photoionization of helium: a comparative study. *J. Phys. B: At. Mol. Opt. Phys.* **28**, L341 (1995).
- [58] C. W. McCurdy, M. Baertschy, and T. N. Rescigno. Solving the three-body Coulomb breakup problem using exterior complex scaling. *J. Phys. B: At. Mol. Opt. Phys.* **37**, R137 (2004).
- [59] J. H. McGuire, *Electron correlation dynamics in atomic collisions*, Cambridge Monographs on Atomic, Molecular, and Chemical Physics (Cambridge University Press, Cambridge, 1997).

- [60] M. Meyer, P. Radcliffe, T. Tschentscher, J. T. Costello, A. L. Cavalieri, I. Grguras, A. R. Maier, R. Kienberger, J. Bozek, C. Bostedt, S. Schorb, R. Coffee, M. Messerschmidt, C. Roedig, E. Sistrunk, L. F. Di Mauro, G. Doumy, K. Ueda, S. Wada, S. Düsterer, A. K. Kazansky, and N. M. Kabachnik. Angle-resolved electron spectroscopy of laser-assisted auger decay induced by a few-femtosecond X-ray pulse. *Phys. Rev. Lett.* **108**, 063007 (2012).
- [61] H. Motz, W. Thon, R. N. Whitehurst. Experiments on radiation by fast electron beams. *Journal of Applied Physics*, **24**, 826 (1953).
- [62] H. G. Muller. Numerical simulation of high-order above-threshold-ionization enhancement in argon. *Phys. Rev. A* **60**, 1341 (1999).
- [63] National Energy Research Scientific Computing Center, www.nersc.gov.
- [64] New era of research begins as world’s first hard X-ray laser achieves “First Light”. *SLAC National Accelerator Laboratory*. April 21, 2009. (Retrieved at April 28, 2015 through <http://home.slac.stanford.edu/pressreleases/2009/20090421.htm>.)
- [65] H. Ni, S. H. Chen, C. Ruiz, and A. Becker. Selection rules in the few-photon double ionization of the helium atom. *J. Phys. B: At. Mol. Opt. Phys.* **44**, 175601 (2011).
- [66] T. Niederhausen and U. Thumm. Controlled vibrational quenching of nuclear wave packets in D_2^+ . *Phys. Rev. A* **77**, 013407 (2008).
- [67] NIST Atomic Spectra Database. http://physics.nist.gov/PhysRefData/ASD/levels_form.html.
- [68] Nobel Prize in Physics. http://www.nobelprize.org/nobel_prizes/physics/.
- [69] Oak Ridge Leadership Computing Facility, www.olcf.ornl.gov.
- [70] A. Palacios, T. N. Rescigno, and C. W. McCurdy. Cross sections for short-pulse single and double ionization of helium. *Phys. Rev. A* **77**, 032716 (2008).

- [71] A. Palacios, T. N. Rescigno, and C. W. McCurdy. Time-dependent treatment of two-photon resonant single and double ionization of helium by ultrashort laser pulses. *Phys. Rev. A* **79**, 033402 (2009).
- [72] A. Palacios, T. N. Rescigno, and C. W. McCurdy. Two-electron time-delay interference in atomic double ionization by attosecond pulses. *Phys. Rev. Lett.* **103**, 253001 (2009).
- [73] A. Palacios, D. A. Horner, T. N. Rescigno, and C. W. McCurdy. Two-photon double ionization of the helium atom by ultrashort pulses. *J. Phys. B: At. Mol. Opt. Phys.* **43**, 194003 (2010).
- [74] J. R. Partington. *A Short History of Chemistry*. Reprinted by Greenwood Press, Inc. (1979).
- [75] R. Pazourek, S. Nagele and J. Burgdörfer. Probing time-ordering in two-photon double ionization of helium on the attosecond time scale. *J. Phys. B: At. Mol. Opt. Phys.* **48**, 061002 (2015).
- [76] R. Pazourek, *private communication*.
- [77] J. S. Parker, L. R. Moore, K. J. Meharg, D. Dundas, and K. T. Taylor. Double-electron above threshold ionization of helium. *J. Phys. B: At. Mol. Opt. Phys.* **34**, L69 (2001).
- [78] T. J. Park and J. C. Light. Unitary quantum time evolution by iterative lanczos reduction. *J. Chem. Phys.* **85**, 5870 (1986).
- [79] L. Y. Peng, Z. Zhang, W. C. Jiang, G. Q. Zhang, and Q. H. Gong. Probe of the electron correlation in sequential double ionization of helium by two-color attosecond pulses. *Phys. Rev. A* **86**, 063401 (2012).
- [80] M. S. Pindzola and F. J. Robicheaux. Total ionization cross section for electron-hydrogen scattering using a time-dependent close-coupling method. *Phys. Rev. A* **54**, 2142 (1996).

- [81] M. S. Pindzola and F. J. Robicheaux. Time-dependent close-coupling calculations of correlated photoionization processes in helium. *Phys. Rev. A* **57**, 318 (1998).
- [82] M. S. Pindzola and F. J. Robicheaux. Erratum: Time-dependent close-coupling calculations of correlated photoionization processes in helium [Phys. Rev. A 57, 318 (1998)]. *Phys. Rev. A* **58**, 779 (1998).
- [83] M. S. Pindzola, F. J. Robicheaux, S. D. Loch, J. C. Berengut, T. Topcu, J. Colgan, M. Foster, D. C. Griffin, C. P. Ballance, D. R. Schultz, T. Minami, N. R. Badnell, M. C. Witthoef, D. R. Plante, D. M. Mitnik, J. A. Ludlow and U. Kleiman. The time-dependent close-coupling method for atomic and molecular collision processes. *J. Phys. B: At. Mol. Opt. Phys.* **40**, R39 (2007).
- [84] M. Pont and R. Shakeshaft. Absolute triply differential cross sections for double photoionization of helium at 10, 20, and 52.9 eV above threshold. *Phys. Rev. A* **51**, R2676 (1995).
- [85] A. Rudenko, V. L. B. de Jesus, Th. Ergler, K. Zrost, B. Feuerstein, C. D. Schröter, R. Moshhammer, and J. Ullrich. Correlated multielectron dynamics in ultrafast laser pulse interactions with atoms *Phys. Rev. Lett.* **93**, 253001 (2004).
- [86] A. Rudenko, K. Zrost, B. Feuerstein, V. L. B. de Jesus, C. D. Schröter, R. Moshhammer, and J. Ullrich. Correlated two-electron momentum spectra for strong-field nonsequential double ionization of He at 800 nm. *Phys. Rev. Lett.* **99**, 263003 (2007).
- [87] A. Rudenko, L. Foucar, M. Kurka, Th. Ergler, K. U. Kühnel, Y. H. Jiang, A. Voitkiv, B. Najjari, A. Kheifets, S. Lüdemann, T. Havermeier, M. Smolarski, S. Schössler, K. Cole, M. Schöffler, R. Dörner, S. Düsterer, W. Li, B. Keitel, R. Treusch, M. Gensch, C. D. Schröter, R. Moshhammer, and J. Ullrich. Recoil-ion momentum distributions for two-photon double ionization of He and Ne by 44 eV free-electron Laser radiation. *Phys. Rev. Lett.* **101**, 073003 (2008).

- [88] T. N. Rescigno and C. W. McCurdy. Numerical grid methods for quantum-mechanical scattering problems. *Phys. Rev. A* **62**, 032706 (2000).
- [89] J. A. R. Samson, W. C. Stolte, Z. X. He, J. N. Cutler, Y. Lu, and R. J. Bartlett. Double photoionization of helium. *Phys. Rev. A* **57**, 1906 (1998).
- [90] B. I. Schneider and N. Nygaard. Orthogonal Functions, Discrete Variable Representation, and Generalized Gauss Quadratures. *J. Phys. Chem. A* **106**, 10773 (2002).
- [91] B. I. Schneider and N. Nygaard. Discrete variable representation for singular Hamiltonians. *Phys. Rev. E* **70**, 056706 (2004).
- [92] B. I. Schneider, L. A. Collins, and S. X. Hu. Parallel solver for the time-dependent linear and nonlinear Schrödinger equation. *Phys. Rev. E* **73**, 036708 (2006).
- [93] O. Schwarzkopf, B. Krässig, J. Elmiger, and V. Schmidt. Energy- and angle-resolved double photoionization in helium. *Phys. Rev. Lett.* **70**, 3008 (1993).
- [94] O. Schwarzkopf, B. Krässig, and V. Schmidt. Energy- and angle-resolved (γ , 2e) experiments with synchrotron radiation: helium and argon. *J. Physique* **3**, 169 (1993); O. Schwarzkopf, *PhD Thesis*, University of Freiburg, Germany (1995).
- [95] O. Schwarzkopf and V. Schmidt. Experimental determination of the absolute value of the triple differential cross section for double photoionization in helium. *J. Phys. B: At. Mol. Opt. Phys.* **28**, 2847 (1995).
- [96] O. Schwarzkopf and V. Schmidt. Experimental determination of the absolute value of the triple differential cross section for double photoionization in helium (CORRIGENDA). *J. Phys. B: At. Mol. Opt. Phys.* **29**, 1877 (1996).
- [97] A. Scrinzi and B. Piraux. Two-electron atoms in short intense laser pulses. *Phys. Rev. A* **58**, 1310 (1998).

- [98] S. Selstø, X. Raynaud, A. S. Simonsen, and M. Førre. Distinction between sequential and direct ionization in two-photon double ionization of helium. *Phys. Rev. A* **90**, 053412 (2014).
- [99] A. E. Siegman. *Lasers*. University Science Books, Sausalito, CA (1986).
- [100] A. S. Simonsen, H Bachau, and M. Førre. Two-photon double ionization of metastable $^{1,3}S$ $1s2s$ helium. *Phys. Rev. A* **89**, 043427 (2014).
- [101] S. A. Sørngård, S. Askeland, R. Nepstad, and M. Førre. Multiphoton ionization and stabilization of helium in superintense XUV fields. *Phys. Rev. A* **83**, 033414 (2011).
- [102] A. W. Stewart. Recent advances in physical and inorganic chemistry. Longmans, Green and Co., New York (2008).
- [103] V. V. Suran, I. P. Zapesochny. Observation of Sr^{2+} in multiple-photon ionization of strontium. *Sov. Tech. Phys. Lett.* **1** 420 (1975).
- [104] Z. Teng and R. Shakeshaft. Double ionization of helium by a single high-energy photon. *Phys. Rev. A* **47**, 3487(R) (1993).
- [105] Z. Teng and R. Shakeshaft. Double ionization of $He(1s^2)$ and $He(1s2s^3S)$ by a single high-energy photon. *Phys. Rev. A* **49**, 3597 (1994).
- [106] X. M. Tong and C. D. Lin. Empirical formula for static field ionization rates of atoms and molecules by lasers in the barrier-suppression regime. *J. Phys. B: At. Mol. Opt. Phys.* **38**, 2593 (2005).
- [107] TOP500 Supercomputer Sites. www.top500.org.
- [108] H. Wang, M. Chini, S. Chen, C.-H. Zhang, F. He, Y. Cheng, Y. Wu, U. Thumm, and Z. Chang. Attosecond Time-resolved autoionization of argon. *Phys. Rev. Lett.* **105**, 143002 (2010).

- [109] G. H. Wannier. The threshold law for single ionization of atoms or ions by electrons. *Phys. Rev.* **90**, 817 (1953).
- [110] B. Walker, B. Sheehy, L. F. DiMauro, P. Agostini, K. J. Schafer, and K. C. Kulander. Precision measurement of strong field double ionization of helium. *Phys. Rev. Lett.* **73**, 1227 (1994).
- [111] Th. Weber, M. Weckenbrock, A. Staudte, L. Spielberger, O. Jagutzki, V. Mergel, F. Afaneh, G. Urbasch, M. Vollmer, H. Giessen, and R. Dörner. Recoil-ion momentum distributions for single and double ionization of helium in strong laser fields. *Phys. Rev. Lett* **84**, 443 (2000).
- [112] F. J. Yang. *Atomic physics (Third Edition)*. Higher Education Press, Beijing (2000).
- [113] R. N. Zare. *Angular Momentum: understanding spatial aspects in chemistry and physics*. Wiley interscience, Now York (1987).
- [114] J. Y. Zeng. *Quantum mechanics*. Scientific Press, Beijing (2005).
- [115] A. H. Zewail. *Femtochemistry: ultrafast dynamics of the chemical bond*, volume 1. World Scientific, 1994.
- [116] A. H. Zewail. Femtochemistry: Atomic-scale dynamics of the chemical bond. *The Journal of Physical Chemistry A*, **104**, 5660 (2000).
- [117] C. H. Zhang and U. Thumm. Laser-assisted photoemission from adsorbate-covered metal surfaces: Time-resolved core-hole relaxation dynamics from sideband profiles. *Phys. Rev. A* **80**, 032902 (2009).
- [118] Q. Zhang, P. Lan and P. Lu. Empirical formula for over-barrier strong-field ionization. *Phys. Rev. A* **90**, 043410 (2014).

- [119] Z. Zhang, L. Y. Peng, M. H. Xu, A. F. Starace, T. Morishita, and Q. Gong. Two-photon double ionization of helium: Evolution of the joint angular distribution with photon energy and two-electron energy sharing. *Phys. Rev. A* **84**, 043409 (2011).
- [120] K. E. Atkinson and G. Chandler. Boundary integral equation methods for solving Laplace's equation with nonlinear boundary conditions: the smooth boundary case. *Mathematics of Computation*, **55**, 451 (1990).
- [121] A. S. Kheifets and I. A. Ivanov. Transverse-electron-momentum distribution in pump-probe sequential double ionization. *Phys. Rev. A* **90**, 033404 (2014).
- [122] I. A. Ivanov and A. S. Kheifets. Time delay in atomic photoionization with circularly polarized light. *Phys. Rev. A* **87**, 033407 (2013).
- [123] M. Nurhuda and F. H. M. Faisal. Numerical solution of time-dependent Schrödinger equation for multiphoton processes: A matrix iterative method. *Phys. Rev. A* **60**, 3125 (1999).

Appendix A

Symmetries in Joint Angular Distribution

In this part, we discuss the symmetries of JADs. Figure 2.3 displays two typical JADs in both linear for SPDI (a) and 3PDI (b) at unequal energy sharing. Both plots display the symmetries about two diagonal lines, these symmetries about the second diagonal line is caused by the indistinguishability of two identical electrons,

$$P(\theta_2, \theta_1) = P(\theta_1, \theta_2). \quad (\text{A.1})$$

The other one comes from the spherical harmonics. We can see more symmetries about these points (θ_1, θ_2) : $(90^\circ, 90^\circ)$, $(180^\circ, 180^\circ)$, $(270^\circ, 90^\circ)$, $(90^\circ, 270^\circ)$, and $(270^\circ, 270^\circ)$. In other words, we have

$$\begin{aligned} P(\theta_1, \theta_2) &= P(\pi + \theta_1, \pi + \theta_2) = P(\pi - \theta_1, \pi - \theta_2) \\ &= P(2\pi - \theta_1, 2\pi - \theta_2). \end{aligned} \quad (\text{A.2})$$

We start from the fact that the spherical harmonics have well-defined parity in the sense that they are either even or odd with respect to reflection about the origin. Reflection about the origin is represented as

$$Y_{lm}(\pi - \theta, \pi + \phi) = (-1)^l Y_{lm}(\theta, \phi). \quad (\text{A.3})$$

and the distribution is proportional to the modules square of bipolar spherical harmonics,

the factor $[(-1)^{l_1+l_2}]^2$ is always 1. Now we have

$$P(\theta_1, \phi_1; \theta_2, \phi_2) = P(\pi - \theta_1, \pi + \phi_1; \pi - \theta_2, \pi + \phi_2). \quad (\text{A.4})$$

Because ϕ and $\phi + \pi$ are on the same plane, it is symmetric about the axis $z = 0$. And we define the $(\pi - \theta, \pi + \phi)$ as $(\pi + \theta, \phi)$:

$$P(\pi - \theta_1, \pi + \phi_1; \pi - \theta_2, \pi + \phi_2) = P(\pi + \theta_1, \phi_1; \pi + \theta_2, \phi_2). \quad (\text{A.5})$$

Because $P(\theta_1, \phi_1; \theta_2, \phi_2)$ is actually independent of ϕ . So we have

$$P(\theta_1, \phi_1; \theta_2, \phi_2) = P(\theta_1, \pi + \phi_1; \theta_2, \pi + \phi_2), \quad (\text{A.6})$$

and

$$P(\pi + \theta_1, \pi + \theta_2) = P(\pi - \theta_1, \pi - \theta_2). \quad (\text{A.7})$$

Adding π on both sides for each variable, we find

$$P(2\pi + \theta_1, 2\pi + \theta_2) = P(2\pi - \theta_1, 2\pi - \theta_2), \quad (\text{A.8})$$

that is

$$P(\theta_1, \theta_2) = P(2\pi - \theta_1, 2\pi - \theta_2). \quad (\text{A.9})$$

Considering the indistinguishability of two identical electrons, $P(\theta_2, \theta_1) = P(\theta_1, \theta_2)$, we have

$$P(\theta_1, \theta_2) = P(2\pi - \theta_2, 2\pi - \theta_1). \quad (\text{A.10})$$

This is the symmetry about the main diagonal line.

Appendix B

First Derivative of the Gaussian-Lobatto Basis in the Finite-Element Discrete Variable Representation Method

Although the first derivative of DVR basis [Eqn. (2.25)] can be found in Refs. [52, 88], we are not aware of an explicit derivation in the literature. In this Appendix, we analytically derive the first derivation of DVR basis at the mesh points [28].

We rewritten the Eqn. (2.25) in one FE only as follow (dismiss the index i)

$$f'_m(x_{m'}) = \begin{cases} \frac{1}{x_m - x_{m'}} \prod_{k \neq m, m'} \frac{x_{m'} - x_k}{x_m - x_k}, & m \neq m', \\ \frac{1}{2\omega_m} (\delta_{m,n} - \delta_{m,1}), & m = m'. \end{cases} \quad (\text{B.1})$$

The first line of Eqn. (B.1) is trivial. We only discuss the derivation of the second line in Eqn. (B.1).

B.1 Preliminary

Because we have to transform all finite elements in physical space into the model space spanned by x from -1 to $+1$, in what follows, we only consider the Legendre polynomial $P_\ell(x)$ in the region $x \in [-1, +1]$. Before we go any further, it is better to keep the differential equation satisfied by $P_\ell(x)$

$$(1 - x^2)P''_\ell(x) - 2xP'_\ell(x) + \ell(\ell + 1)P_\ell(x) = 0. \quad (\text{B.2})$$

in mind. Here $P'_\ell(x)$ and $P''_\ell(x)$ are the first- and second-order derivatives of $P_\ell(x)$, respectively. We assume that we choose N DVR mesh points in the region $[-1, +1]$. These N points are determined through the zero points of $P'_{N-1}(x)$ and two boundary points at ± 1 . In other words, we organize the mesh points in the following way: $x_1, x_2, x_3, \dots, x_{N-1}, x_N$, in which $x_1 = -1$, $x_N = +1$, and $P'_{N-1}(x_i) = 0$ ($2 \leq i \leq N-1$). Once the mesh points are determined, the relevant Lobatto basis in the DVR method is defined by

$$f_i(x) = \prod_{j=1(\neq i)}^N \frac{x - x_j}{x_i - x_j}. \quad (\text{B.3})$$

Let us consider how to analytically obtain their first-order derivative at the same mesh point where the basis is defined, i.e., $df_i(x_i)/dx$. To this end, we divide the problem into the two cases: (i) non-boundary DVR basis [$f_i(x)$ ($2 \leq i \leq N-1$)], and (ii) boundary DVR basis [$f_1(x)$ and $f_N(x)$].

B.2 Case (i)

In this case, the DVR basis [Eqn. (B.3)] can be recast as

$$f_i(x) = \frac{1}{A_{N-2}} \frac{1}{\prod_{j \neq i} (x_i - x_j)} \frac{(x^2 - 1)P'_{N-1}(x)}{x - x_i}. \quad (\text{B.4})$$

Here, A_{N-2} is the coefficient corresponding to the highest-order term of x^{N-2} in $P'_{N-1}(x)$. In what follows, we will leave $1/[A_{N-2} \prod_{j \neq i} (x_i - x_j)]$ out in $f_i(x)$ to simplify notation, since it is a constant for a given basis. Therefore, we have

$$\begin{aligned} f'_i(x) &= \frac{(x^2 - 1)P''_{N-1}(x)}{x - x_i} + \frac{2xP'_{N-1}(x)}{x - x_i} - \frac{(x^2 - 1)P'_{N-1}(x)}{(x - x_i)^2} \\ &= \frac{1}{(x - x_i)^2} \left\{ (x - x_i) \left[(N-1)NP_{N-1}(x) - 2xP'_{N-1}(x) \right] \right. \\ &\quad \left. + 2x(x - x_i)P'_{N-1}(x) - (x^2 - 1)P'_{N-1}(x) \right\} \\ &= \frac{1}{(x - x_i)^2} \left\{ (x - x_i)(N-1)NP_{N-1}(x) - (x^2 - 1)P'_{N-1}(x) \right\}, \end{aligned} \quad (\text{B.5})$$

in which Eqn. (B.2) was used. In the limit of $x \rightarrow x_i$, the above derivative turns to be a limit of type 0/0. After carrying out the derivatives of the denominator and numerator separately, we have

$$\begin{aligned}
f'_i(x_i) &= \lim_{x \rightarrow x_i} \frac{1}{2(x-x_i)} \left\{ N(N-1)(x-x_i)P'_{N-1}(x) + N(N-1)P_{N-1}(x) \right. \\
&\quad \left. - 2xP'_{N-1}(x) - (x^2-1)P''_{N-1}(x) \right\} \\
&= \frac{1}{2}N(N-1)P'_{N-1}(x_i) = 0.
\end{aligned} \tag{B.6}$$

At this point, we recognize that $f'_i(x_i) = 0$ for non-boundary DVR basis. This indicates that the the first-order derivative of the DVR basis vanishes at the point where the DVR basis is defined. In other words, x_i is an extreme point for $f_i(x)$. It comes as no surprise, since we already know that $f_i(x_i) = 1$ at $x = x_i$, which corresponds to a maximum of $f_i(x)$.

B.3 Case (ii)

Now we consider a boundary. We only take the case of $x_1 = -1$ as an example to show how we derive $f'_1(x_1)$. The same procedure can be extended to the case of $x_N = +1$. We know that for the Gauss-Lobatto quadrature, we always have

$$P'_{N-1}(x) = A_{N-2} \prod_{i=2}^{N-1} (x - x_i), \tag{B.7}$$

where the coefficient A_{N-2} corresponds to the leading term of x^{N-2} in $P'_{N-1}(x)$. Its detailed expression is not important for our present purpose. A_{N-2} should be canceled, as we will see later. In this case, after using

$$f_1(x) = \frac{1}{\prod_{j \neq 1}^N (x_1 - x_j)} \frac{P'_{N-1}(x)}{A_{N-2}} (x - 1), \tag{B.8}$$

we have

$$f'_1(x) = \frac{1}{A_{N-2} \prod_{j \neq 1}^N (x_1 - x_j)} \left[P''_{N-1}(x)(x-1) + P'_{N-1}(x) \right]. \tag{B.9}$$

On the other hand, at $x_1 = -1$, we have

$$\prod_{j \neq 1}^N (x_1 - x_j) = (-1 - x_2)(-1 - x_3) \cdots (-1 - x_{N-1})(-1 - 1) = \frac{(-2)}{A_{N-2}} P'_{N-1}(-1). \quad (\text{B.10})$$

Therefore, $f'_1(-1)$ can be recast as

$$f'_1(-1) = \frac{P''_{N-1}(-1)}{P'_{N-1}(-1)} - \frac{1}{2}. \quad (\text{B.11})$$

Now, the question is, how can we obtain $P'_{N-1}(-1)$ and $P''_{N-2}(-1)$. The value of $P'_{N-1}(-1)$ is trivial. It is available in some books [1]. However, $P''_{N-1}(-1)$ is far from trivial, which can be found in Ref.¹. Here, I am going to show how I obtain both $P'_{N-1}(-1)$ and $P''_{N-1}(-1)$ in a systematical way. For the Legendre polynomial $P_\ell(x)$ at any order $\ell \geq 0$, I start with

$$P_\ell(x) = \frac{1}{2^\ell} \sum_{k=0}^{\ell} \binom{\ell}{k}^2 (x-1)^{\ell-k} (x+1)^k. \quad (\text{B.12})$$

Therefore, we have

$$P'_\ell(x) = \frac{1}{2^\ell} \sum_{k=0}^{\ell} \binom{\ell}{k}^2 k (x-1)^{\ell-k} (x+1)^{k-1} + \frac{1}{2^\ell} \sum_{k=0}^{\ell} \binom{\ell}{k}^2 (\ell-k) (x-1)^{\ell-k-1} (x+1)^k, \quad (\text{B.13})$$

$$\begin{aligned} P''_\ell(x) &= \frac{1}{2^\ell} \sum_{k=0}^{\ell} \binom{\ell}{k}^2 k(k-1) (x-1)^{\ell-k} (x+1)^{k-2} \\ &+ \frac{1}{2^\ell} \sum_{k=0}^{\ell} \binom{\ell}{k}^2 k(\ell-k) (x-1)^{\ell-k-1} (x+1)^{k-1} \\ &+ \frac{1}{2^\ell} \sum_{k=0}^{\ell} \binom{\ell}{k}^2 k(\ell-k) (x-1)^{\ell-k-1} (x+1)^{k-1} \\ &+ \frac{1}{2^\ell} \sum_{k=0}^{\ell} \binom{\ell}{k}^2 (\ell-k-1)(\ell-k) (x-1)^{\ell-k-2} (x+1)^k. \end{aligned} \quad (\text{B.14})$$

Keeping only those non-zero terms ($k \leq 2$, say), simple algebra shows at $x = -1$,

$$P'_\ell(-1) = -\frac{1}{2}(-1)^\ell \ell(\ell+1) \quad \text{and} \quad P''_\ell(-1) = \frac{1}{8}(-1)^\ell (\ell-1)\ell(\ell+1)(\ell+2). \quad (\text{B.15})$$

After replacing ℓ by $N-1$, this means that

$$f'_1(-1) = \frac{P''_{N-1}(-1)}{P'_{N-1}(-1)} - \frac{1}{2} = -\frac{1}{4}(N-1)N. \quad (\text{B.16})$$

Furthermore, the same procedure applied to $x_N = +1$ shows that

$$f'_N(+1) = \frac{1}{4}(N-1)N. \quad (\text{B.17})$$

Remember that at these two boundary points, the weight factor in Gauss-Lobatto quadrature is

$$\omega_{1,N} = \frac{2}{(N-1)N}. \quad (\text{B.18})$$

The results at the two boundary points $x_i = -1$ and $x_i = +1$ can be summarized as

$$f'_i(x_i) = \frac{1}{2\omega_i}[\delta_{iN} - \delta_{i1}]. \quad (\text{B.19})$$

B.4 Conclusion

At this point, we recognized that the results we derived so far [both cases (i) and (ii)] can be written in a single equation

$$f'_i(x_i) = \frac{1}{2\omega_i}[\delta_{iN} - \delta_{i1}], \quad (\text{B.20})$$

for any Lobatto mesh point x_i from x_1 to x_N . This equation corresponds to Eqn. (17a) in the paper of Manolopoulos and Wyatt [52]. The same equation was shown as the second case of Eqn. (20) in Rescigno and McCurdy's work [88]. Comparing their equations with my equation, we see that Manolopoulos and Wyatt's equation has a misprint. The order of the two terms in that equation should be exchanged, i.e., a minus sign should be multiplied to correct the equation.

Appendix C

Numerical Convergence Test

We have tested our new FE-DVR code to assess the accuracy of our numerical results relative to the numerical effort (in terms of computing time and random access memory) and published data.

C.1 Convergence with Respect to l_1 and l_2

As a first test, we computed the ground and two first excited $L = 0$ state energies of helium. Using the imaginary time propagation method [31], we replace the real time variable t in our FE-DVR code by the imaginary time variable $\tau = it$ and numerically propagated Eqn. (2.43) in imaginary time. The propagation starts with an initial two-electron trial wave function for the helium ground state, given as the product of Gaussian functions,

$$\psi_{l_1 l_2}^{00}(r_1, r_2; t = 0) = A e^{-(r_1 - r_0)^2 - (r_2 - r_0)^2} \quad (\text{C.1})$$

with the normalization constant A and $r_0 = 10$. Since we have to normalize the wave function every couple steps (e.g., every 10 steps we used), it doesn't matter what the initial value of the normalization constant A is, we could simply set it as 1 for the initial state.

To test our code, we represent the radial distances $0 \leq r_1 \leq r_1^{\max} = 60$ and $0 \leq r_2 \leq r_2^{\max} = 60$ on two different numerical grids. For each radial distance, "Grid 1" consists of 50 elements with 4 grid points in each FE. After taking the bridge DVR functions into account, it results in a total $50 \times (4 - 1) - 1 = 149$ points for "Grid 1". Similarly, "Grid 2" contains

Table C.1: The energies of the 1^1S ground state and the two lowest $L=0$ excited states (2^1S and 3^1S) of helium. The correlation matrix elements $r_{<}^l/r_{>}^{l+1}$ (cf. Appendix A) are computed by either Gaussian-Lobatto integration (“Direct-integration method”) or by solving Poisson’s equation (“Poisson’s Eqn.”). The FE-DVR imaginary time propagation calculations were performed for two different radial numerical grids covering $0 \leq r_1 \leq r_1^{\max} = 60$ a.u. and $0 \leq r_2 \leq r_2^{\max} = 60$ a.u.: “Grid 1” uses 50 elements with 4 grid points in each element, and “Grid 2” uses 20 elements with 10 grid points in each element. The last three rows show theoretical [97, 119] and experimental [53] energies from literature. All the energies are given in a.u.

Method/Source	1^1S	2^1S	3^1S
Direct integration (Grid 1)	-2.889 6	-2.130 1	–
Direct integration (Grid 2)	-2.901 7	-2.144 6	–
Poisson’s Eqn. (Grid 1)	-2.903 363 5	-2.145 900 6	-2.061 272 0
Theoretical value [119]	-2.903 669 0	-2.145 970 6	-2.061 271 0
Theoretical value [97]	-2.903 724 4	-2.145 974 0	-2.061 272 0
Experimental value [53]	-2.903 561 2	-2.145 898 6	-2.061 201 7

20 elements with 10 grid points in each FE, resulting in a total of 179 grid points for each radial coordinate.

We repeatedly applied Eqn. (2.43), propagating the TDSE for 0.5 fs with equidistant time steps for predetermined maximal values l_1^{\max} and l_2^{\max} of l_1 and l_2 . We used the same time step as Hu [33], $\Delta t = 0.0041$. For $0 \leq l_1 \leq l_1^{\max} = 3$, $0 \leq l_2 \leq l_2^{\max} = 3$, and $L = 0$, we found that the ground-state energy has converged with respect to the propagation time and number of time steps to at least four significant decimal digits on either Grid 1 or Grid 2.

Our energies for the 1^1S ground state of He, computed by FE-DVR imaginary-time-propagation for $l_1^{\max} = l_2^{\max} = 3$, including the four channels $(L, l_1, l_2) = (0,0,0)$, $(0,1,1)$, $(0,2,2)$, and $(0,3,3)$, agree to four significant digits with our result for $l_1^{\max} = l_2^{\max} = 10$, including eleven $L = 0$ channels. Our calculated ground-state energies also coincide to four significant digits with published experimental [53] and recently calculated theoretical [119] energies (Tab. C.1).

Following the same imaginary time-propagation procedure, and projecting the converged

ground state out of the trial wave function Eqn. (C.1) every 10 steps, we obtain the energies of the first excited 2^1S state listed in third column of Tab. C.1. Similarly, repeatedly projecting both, the converged ground and first excited states out of Eqn. (C.1) every 10 time steps during the numerical wave-function propagation, we arrive at the second excited zero-angular-momentum 3^1S state energy in the fourth column. We obtain our most accurate values for the energies of the 2^1S state, -2.145 900 6 a.u., and the 3^1S state, -2.061 272 0 a.u., by applying the ‘‘Poisson’s equation method’’ [see Sec. (C.3)] [46, 58]. These first and second excited $L = 0$ state energies are in good agreement with the theoretical values, -2.145 970 6 a.u. and -2.061 271 0 a.u., calculated by Zhang *et al.* [119] using the same FE-DVR method with parameters $l_1^{\max} = l_2^{\max} = 7$ a.u., $r_1^{\max} = r_2^{\max} = 60$ a.u. divided into 64 elements, and the measured energies, -2.145 898 6 and -2.061 201 7 a.u. [53], respectively. The corresponding radial probability densities,

$$p(r_1, r_2) = \sum_{Ll_1l_2} |\psi_{l_1l_2}^{L0}(r_1, r_2)|^2, \quad (\text{C.2})$$

are calculated on numerical Grid 1 by imaginary time propagation for the ground and first excited state with $L=0$ and shown in Fig. 4.2. The ground-state probability density has a maximum at $r_1 = r_2 \approx 0.9$ a.u. The first excited state has maxima at $r_1 = r_2 \approx 0.5$ a.u. and $r_1 = r_2 \approx 4.5$ a.u., and a node at $r_1 = r_2 \approx 1.7$ a.u.

C.2 Convergence with Respect to the Numerical Grid Size

We compared the ground-state and first excited-state energies for imaginary time propagation calculations with different numbers of FEs and different numbers of grid points in each element. We performed these calculations with $L = 0$ and $l_1^{\max} = l_2^{\max} = 3$.

Table C.1 includes our results for the ground and first-excited-state energies of helium. As listed in the first two rows, the calculation on Grid 1 results in the energies -2.889 6 a.u. and -2.130 1 a.u., while using Grid 2 we obtain -2.901 7 a.u. and -2.144 6 a.u., respectively

for the 1^1S and 2^1S states of helium. As expected, the numerical grid with more points (Grid 2) yield results in better agreement with the measured energies (the last row in Tab. C.1).

C.3 Comparison of the “Poisson Equation” and “Direct Integration” Methods

We next compare results for the lowest helium energies obtained by either diagonalizing the matrices representing the electronic correlation terms $r_{<}^l/r_{>}^{l+1}$ [$r_{<} \equiv \min(r_1, r_2)$, and $r_{>} \equiv \max(r_1, r_2)$] in Eqn. (2.41) via Gauss-Lobatto integration or by solving Poisson’s equation [58]. Knowing that the “Poisson equation” method is better suited to overcome numerical problems related to the singular $1/|\mathbf{r}_2 - \mathbf{r}_1|$ electronic correlation interaction, it is nevertheless worth pointing out that our ground and excited states energies agree better with the calculated energies of Zhang *et al.* [119] and the measured data by Martin [53] for calculations with the smaller numerical grid (Grid 1) in combination with Poisson’s equation than for calculations carried out on the larger grid (Grid 2) in conjunction with a straight-forward Gauss-Lobatto integration. Using the Poisson equation method and the smaller Grid 1 we find that the three lowest helium energies in Tab. C.1 are converged to at least four significant digits and agree to at least three significant digits with published experimental [53] and recently calculated theoretical [119] energies.

The ground-state energy (-2.903 67 a.u.) obtained by Zhang *et al.* [119] is in slightly better agreement with the experimental value (-2.903 56 a.u.) than our best value in Tab. C.1 (-2.903 36 a.u.). This is to be expected in view of the numerically significantly more expensive FE-DVR calculation by Zhang *et al.* with parameters $r_1^{\max} = r_2^{\max} = 60$ a.u., $l_1^{\max} = l_2^{\max} = 7$, 64 FEs, and 8 grid points in each element. Our best numerical value for the ground-state energy in Tab. C.1, agrees equally well with the result of a calculation using an explicitly correlated basis, -2.903 72 a.u., by Scrinzi *et al.* [97].

The third and fourth column of Tab. C.1 compare the energies of first- and second-excited $L = 0$ states from different sources. Our best values for the energies of the 2^1S state

(dominated by the configurations $1s2s$), $-2.145\,900\,6$ a.u., and 3^1S state ($1s3s$ dominated), $-2.061\,272\,0$ a.u., are in good agreement with the theoretical values, $-2.145\,970\,6$ and $-2.061\,271\,0$ a.u., of Zhang *et al.* [119], $-2.145\,974\,0$ and $-2.061\,272\,0$ a.u. of Scrinzi *et al.* [97], and the experimental values, $-2.145\,898\,6$ and $-2.061\,201\,7$ a.u., of Martin *et al.* [53], respectively. Our results for the excited-state energies agree to five digits with the measured energies, while we reproduce the measured ground-state energy to three digits. We note that the experimental energies quoted in Table I also agree slightly better with both, relativistic and non-relativistic calculations by Alexander *et al.* [2] for the excited states than the ground state.

C.4 Convergence in the Number of Included Total Angular Momenta L

In this subsection, we discuss the convergence of joint angular distributions with regard to the number of total angular momentum states $\psi_{l_1 l_2}^{LM}$ included in Eqn. (2.40) for the IR-laser-pulse-assisted XUV DI of helium. The central frequency, intensity, and pulse length for the XUV and IR pulses are $\hbar\omega_{XUV} = 89$ eV, $I_{XUV} = 10^{14}$ W/cm², $\tau_{XUV} = 0.47$ fs (10 XUV optical cycles) and $\hbar\omega_{IR} = 1.61$ eV, $I_{IR} = 3 \times 10^{12}$ W/cm², $\tau_{IR} = 2.6$ fs (1 IR optical cycle), respectively. We assume that the two linearly polarized pulses coincide (no time delay) and equal energy sharing of the emitted electrons ($E_1 = E_2$). We performed these calculations for a numerical grid, referred to as “Grid 3”, with 151 elements, 4 grid points in each FE, the first FE length (near the origin) equal to 0.5, and $r_{\max} \approx 277$. Grid 3 is an extension of “Grid 1” with additional 101 elements.

The graphs in Fig. C.1 shows JADs for IR-laser-assisted XUV DI obtained from separate calculations for maximal angular momentum quantum numbers, $(L, l_1, l_2)_{\max} \equiv (L_{\max}, l_1^{\max}, l_2^{\max}) = (3, 3, 3), (4, 4, 4), (5, 5, 5)$ and $(6, 6, 6)$, corresponding to 23, 42, 69 and 106 channels, respectively. All the angular distributions are snapshots taken 20 a.u. after the end of the cosine-squared-shaped IR laser pulse. The graphs in the top (bottom) row show angular

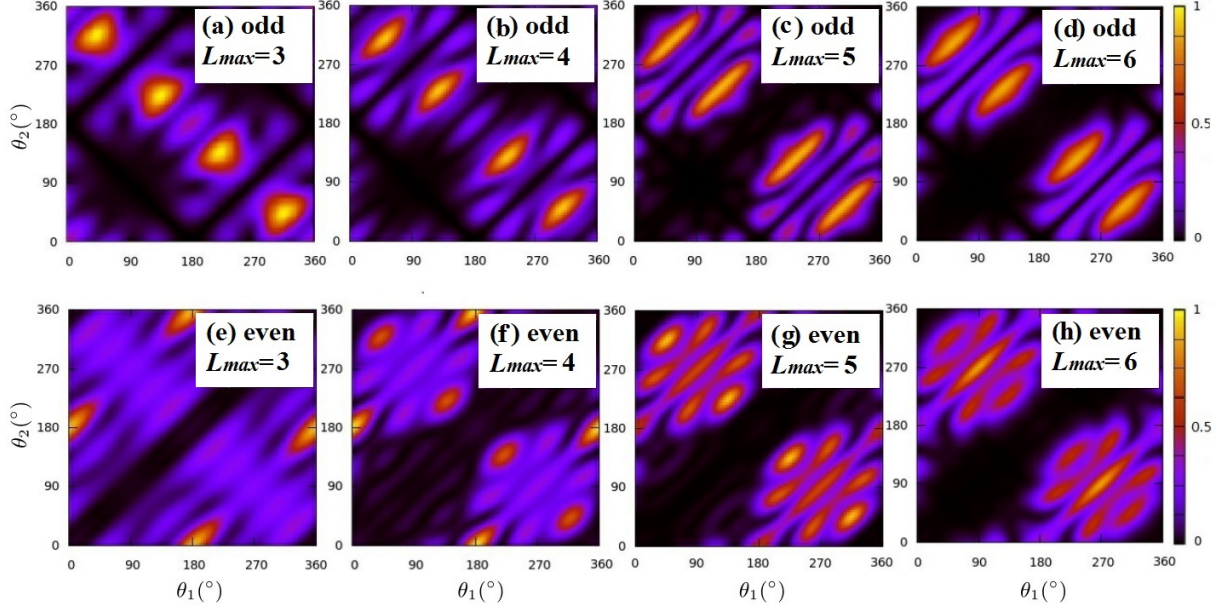


Figure C.1: Normalized joint angular distributions for IR-laser-assisted XUV double ionization of helium at equal energy sharing for maximal angular momentum quantum numbers (a, e) $(L, l_1, l_2)_{\max} \equiv (L_{\max}, l_1^{\max}, l_2^{\max}) = (3, 3, 3)$, (b, f) $(4, 4, 4)$, (c, g) $(5, 5, 5)$, and (d, h) $(6, 6, 6)$. (a-d) Results for odd and (e-h) even photon numbers. The photon numbers correspond to one absorbed XUV plus the number of absorbed minus emitted IR photons.

distributions for even (odd) total photon numbers. The total number of photons consists of one absorbed XUV photon plus the number of absorbed minus emitted IR photons. All JADs discussed in this section (Appendix C) are normalized to their maximal yields and color (gray-scale)-coded on a linear scale.

With increasing L_{\max} the JADs show more structures in Fig. C.1. In addition, though it is not directly observable, the low probability for side-by-side emission turns to be negligible. While the intensity distributions for $L_{\max} = 4, 5$, and 6 show small discrepancies, their main structures are the same, and the JADs appear to have converged at $L_{\max} = 5$ with regard to their main characteristics. For this reason we use $(L, l_1, l_2)_{\max} = (5, 5, 5)$ corresponding to 69 partial wave channels for all subsequent numerical results discussed in the work, unless specified otherwise.

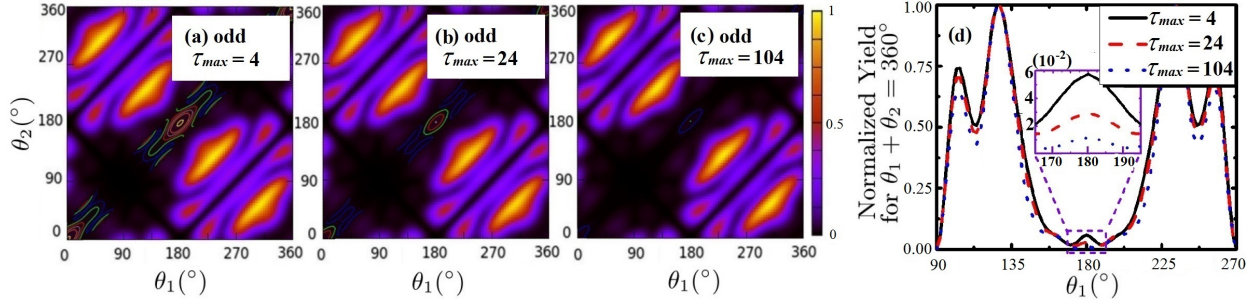


Figure C.2: Normalized joint angular distributions for IR-laser-assisted XUV-double ionization of helium at equal energy sharing for the different propagation times τ_{\max} past the end of the IR pulse. (a) $\tau_{\max} = 4$ a.u.; (b) $\tau_{\max} = 24$ a.u.; (c) $\tau_{\max} = 104$ a.u.. (d) Normalized double-ionization yields at $\theta_1 + \theta_2 = 360^\circ$. As the propagation time is increased, the side-by-side-emission yield at $\theta_1 = \theta_2 = 180^\circ$ disappears as physically expected.

C.5 Convergence in the Propagation Time

Figure C.2 shows JADs for laser-assisted XUV DI of helium for the equal energy sharing of the emitted electrons. The calculations are performed on Grid 3, using the Poisson-equation method for the $1/r_{1,2}$ interaction matrix elements and the angular-momentum limits $(L, l_1, l_2)_{\max} = (3, 3, 3)$. The three graphs display snapshots of JADs calculated according to Eqn. (2.77) and taken at different propagation times τ_{\max} past the end of IR pulse.

The JAD for $\tau_{\max} = 4$ a.u. in Fig. C.2(a) differs from the JAD for $\tau_{\max} = 24$ a.u. in Fig. C.2(b), mainly with regard to the smaller not observable contribution of side-by-side emission. This contribution is physically prohibited at large distances from the residual helium nucleus due to electronic repulsion. For $\tau_{\max} = 104$ a.u. the JAD is converged and it is indistinguishable from Fig. C.2(b), except for side-by-side emission, and no longer displays side-by-side emission [Fig. C.2(c)]. Indicative for the not observable contribution of side-by-side emission for finite τ_{\max} is the absolute value of the JAD at $\theta_1 = \theta_2 = 180^\circ$. These absolute values are not shown on the normalized graphs. They decrease from 0.059 to 0.029 to 0.01 for $\tau_{\max}=4, 24$ and 104 a.u. in Figs. C.2(a), (b), and (c), respectively. We performed a similar convergence test for even photon numbers (not shown) and found much

faster convergence in τ_{\max} than for odd photon numbers.

We display in Fig. C.2(d) the normalized angular yields obtained from the JADs in Fig. C.2(a-c) on the diagonal defined by $\theta_2 = 360^\circ - \theta_1$. This graph thus highlights the four dominant peaks in Fig. C.2(a-c) and side-by-side emission with $\theta_1 = \theta_2 = 0$ or 180° , where convergence in τ_{\max} is most difficult to achieve.

For an alternative quantitative comparison of the convergence in τ_{\max} , we also calculated relative integrated side-by-side yields obtained by integrating the JADs in Fig. C.2(a-c) over a narrow diagonal stripe defined by $\theta_2 = \theta_1$. The width of this stripe is taken as 10° , i.e., $|\theta_1 - \theta_2| \leq 5^\circ$, centered at $\theta_1 = \theta_2$, 5° for each side. The relative integrated side-by-side yield drops from 0.24% at $\tau_{\max} = 4$ to 0.13% at $\tau_{\max} = 24$ a.u., and to 0.05% at $\tau_{\max} = 104$ a.u., while the amplitudes of side-by-side-emission-peak heights decrease from 0.06 to 0.03, and finally to 0.01, respectively. Thus, as physically demanded, side-by-side emission disappears for sufficiently long propagation time, while for relative emission angles of the two photoelectrons outside the side-by-side range converged JADs are readily obtained at the end of the IR pulse. In particular, the nodal structure in Fig. C.2 for non-side-by-side emission is not affected by increasing τ_{\max} , as expected from the selection rules discussed by Maulbetsch and Briggs [56].

Currently, for each result in Fig. C.1 and Fig. C.2, we allocated 20 Gb RAM memory, and ran the jobs via OpenMP on 10 Intel Core i7-2600 3.40GHz central processing units (CPUs), about 200 hours on each CPU. The RAM memory requirement is of order of $3 \times 16 \times n_{Ch}^2 \times n_{size}^2 / 1024^3$ Gb, where 3 is number of the biggest matrix we used plus 1 (to include the many smaller matrix), 16 stands for the double complex variables we used, and n_{size} is the grid size in each dimension (r_1 and r_2). Currently, we adopt a 300×300 box (100 finite elements in each dimension), and 69 channels. To improve the results, for example, we take a configuration $(L, l_1, l_2)_{max} = (10, 10, 10)$. In this case, we have about 400 channels. This requires about 650 Gb RAM memory which well exceeds our local capability (32 Gb) now. For a 10 times longer pulse and longer propagation times, we have to extend

the box size, about 10 times in each dimension, which will also largely increase the memory requirement (from 20 Gb to 63 Tb). These increases will result in the CPU time requirement increasing about 3×10^4 times, from 2×10^3 to 6×10^7 CPU hours. If we use 100 nodes with 24 CPUs each, it would require 3 calendar years to finish one computing job. We started to investigate a graphics processing unit (GPU) based application [36], which might greatly reduce the computing time.

Appendix D

Copyright Clearance

In this thesis, we have cited and adapted some figures from the literature. To reuse these figures, we have to obtain the permission from American Physical Society. This has been done through Copyright Clearance Center on its website www.copyright.com.

D.1 Copyright Clearance for Fig. 4.3, 4.12, 4.13 and Fig. 4.14

**American Physical Society
License Details**

May 19, 2015

This is an Agreement between Aihua Liu ("You") and American Physical Society ("Publisher"). It consists of your order details, the terms and conditions provided by American Physical Society, and the payment instructions.

License Number	3623390665167
License date	May 06, 2015
Licensed content publisher	American Physical Society
Licensed content publication	Physical Review A
Licensed content title	Two-photon double ionization of helium: Evolution of the joint angular distribution with photon energy and two-electron energy sharing
Licensed copyright line	©2011 American Physical Society
Licensed content author	Zheng Zhang et al.
Licensed content date	Oct 6, 2011
Volume number	84
Type of Use	Thesis/Dissertation
Requestor type	Student
Format	Electronic
Portion	chapter/article
Rights for	Main product
Duration of use	Life of current edition
Creation of copies for the disabled	no
With minor editing privileges	no
For distribution to	United States
In the following language(s)	Original language of publication
With incidental promotional use	no
The lifetime unit quantity of new product	0 to 499
The requesting person/organization is:	Aihua Liu
Order reference number	None
Title of your thesis / dissertation	Energy- and angular-resolved infrared-laser-assisted XUV single and double ionization of helium
Expected completion date	May 2015
Expected size (number of pages)	165
Total	0.00 USD

D.2 Copyright Clearance for Fig. 4.6

American Physical Society License Details

May 19, 2015

This is an Agreement between Aihua Liu ("You") and American Physical Society ("Publisher"). It consists of your order details, the terms and conditions provided by American Physical Society, and the payment instructions.

License Number	3632610806389
License date	May 19, 2015
Licensed content publisher	American Physical Society
Licensed content publication	Physical Review A
Licensed content title	Symmetrized amplitudes of the helium-atom double photoionization
Licensed copyright line	Copyright © 2002, American Physical Society
Licensed content author	A. S. Kheifets and Igor Bray
Licensed content date	Jan 15, 2002
Volume number	65
Type of Use	Thesis/Dissertation
Requestor type	Student
Format	Print, Electronic
Portion	chapter/article
Rights for	Main product
Duration of use	Life of current edition
Creation of copies for the disabled	no
With minor editing privileges	no
For distribution to	United States
In the following language(s)	Original language of publication
With incidental promotional use	no
The lifetime unit quantity of new product	0 to 499
The requesting person/organization is:	Aihua Liu
Order reference number	None
Title of your thesis / dissertation	Energy- and angular-resolved infrared-laser-assisted XUV single and double ionization of helium
Expected completion date	May 2015
Expected size (number of pages)	165
Total	0.00 USD
Terms and Conditions	

D.3 Copyright Clearance for Fig. 4.11

American Physical Society License Details

May 19, 2015

This is an Agreement between Aihua Liu ("You") and American Physical Society ("Publisher"). It consists of your order details, the terms and conditions provided by American Physical Society, and the payment instructions.

License Number	3623390028538
License date	May 06, 2015
Licensed content publisher	American Physical Society
Licensed content publication	Physical Review A
Licensed content title	Dynamics of two-photon double ionization of helium in short intense xuv laser pulses
Licensed copyright line	Copyright © 2008, American Physical Society
Licensed content author	Xiaoxu Guan, K. Bartschat, and B. I. Schneider
Licensed content date	Apr 29, 2008
Volume number	77
Type of Use	Thesis/Dissertation
Requestor type	Student
Format	Electronic
Portion	chapter/article
Rights for	Main product
Duration of use	Life of current edition
Creation of copies for the disabled	no
With minor editing privileges	no
For distribution to	United States
In the following language(s)	Original language of publication
With incidental promotional use	no
The lifetime unit quantity of new product	0 to 499
The requesting person/organization is:	Aihua Liu
Order reference number	None
Title of your thesis / dissertation	Energy- and angular-resolved infrared-laser-assisted XUV single and double ionization of helium
Expected completion date	May 2015
Expected size (number of pages)	165
Total	0.00 USD
Terms and Conditions	

Appendix E

Sources and Data Files Descriptions

In this appendix, we list and describe all F90 source codes and input/output files for

(i) Our FE-DVR implementation for the solving TDSE by the Arnoldi-Lanczos propagator based on Krylov subspace projection techniques;

(ii) Data analysis by projection on products of Coulomb continuum wave functions;

(iii) Input and output files used in (i) and (ii).

All codes are written in F90. Numerical packages, such as *LAPACK*, *ARPACK* and *BLAS*, are employed in matrix algebra operations.

E.1 How to Use this Software

The operation routine is:

- (1) Compile executable file `he2color_fedvr`.
- (2) Compile `configcalc.f90` and run `configcalc.x` to obtain the angular-momentum configuration in selected partial-wave file.
- (3) Modify `parameter.inp` to configure FE-DVR settings.
- (4) Modify `tdse.inp` to configure the parameter-setting for the TDSE solution, including laser field, XUV pulse, read-in files (configuration file and initial wave-function file)

and their locations, Lanczos order and tolerance, wave-function absorption parameter, propagation time and step.

- (5) Modify the script file `run.uni` to configure parallelization. Then run `run.uni`.
- (6) Copy the data files to the directory *analysis*.
- (7) Run the executable files `or.x` / `er.x` / `ar.x` to analyze data.
- (8) Compile and run `theta12.f90`, `sbsrate.f90`. JAD file (`fort.700`) obtained from step (7) is required.

E.2 Source Codes and Files

Table E.1: This table lists and describes makefile, main program and subroutines.

file name	function description
Makefile	Compiles source files and makes executable file.
helium_fedvr.f90	The main program. It is the entry of whole program.
accuracy_real.f90	Defines the accuracy of real numbers.
globalmod_constants.f90	Defines the globally-used constants.
globalmod_discrete.f90	Defines the globally-used variables for DVR.
readin.f90	Reads in the FE-DVR parameters.
hamiltonian_matrix.f90	Calculates the 1-d Hamiltonian matrix.
lagrange_dvr_derivative.f90	Calculates the first derivative of DVR basis functions.
lgngr.f90	Finds Lagrange interpolation polynomials as a function of x and their first and second derivatives on an arbitrary grid y .
gaussq.f90	Generates the Gaussian quadratures.
expokit.f90	Includes all subroutines used for computing the operation $w = \exp(t * A) * v$ based on Krylov subspace projection techniques. A is a complex matrix; w and v are vectors.
mataid.f90	Includes all subroutines used for the matrix-vector multiplication routines.
localincludes.f90	Defines most of variables in the TDSE. Includes one parallelized subroutine for computing $w = \exp(t * A) * v$.
laser.f90	Defines and computes the laser field.
configcalc.f90	Selects the partial waves to be used in the TDSE.

Table E.2: This table lists and describes the files for data analysis. The .x files are executable files obtained from compiling the source files in the same row.

file name	function description
TDCS.f90, ar.x	Computes TDCSs, total cross sections, JEDs, and JADs.
eTDCS.f90, er.x	Computes JADs with even parity.
oTDCS.f90, or.x	Computes JADs with odd parity.
ylm.f90	Computes spherical harmonics $Y_l^m(\theta, \phi)$.
anglib.f90	Subroutines for ylm.f90.
gamma.f90	Computes the Gamma function $\Gamma(x)$.
theta12.f90	Computes mutual angular distributions.
sbsrate.f90	Computes rate of side-by-side emission.

Table E.3: This table lists and describes the input files.

file name	function description
parameter.inp	Parameters for FE-DVR setting.
tdse.inp	Parameters for TDSE setting.
initnxm	Saves initial-state wave function.
run.uni	Launches the executable program (e.g., <code>he2color_fedvr</code>).

Table E.4: This table lists and describes the output files.

file name	function description
fort.500	Original configuration (Computed through <code>configcalc.x</code>).
fort.509	Electric field data.
fort.526	Saves the grids and weights data.
fort.600	JED, saves in the form for <i>gnuplot</i> 3-D plotting.
fort.604	JED, saves in complex format.
fort.620	Distribution versus energy sharing.
fort.700	JAD $[\theta_1, \theta_2, P(\theta_1, \theta_2)]$
fort.748	Symmetrical-emission data on JAD.
fort.800	Products of Coulomb Waves.
fort.806	SDCS (E_1 , SDCS).
fort.810	TDCS (θ, ϕ , TDCS)
fort.850	Coulomb wave functions
fort.999	Error information.
fort.1000	Initial-state wave function.
fort.1001-fort.9999	Wave-function snapshots.
running	Records program execution history.

```

helium_fedvr.f90 x
0 10 20 30 40 50 60 70 80
1  !-----!
2  ! This code demonstrates the implementation of FE-DVR for one-electron atoms, !
3  ! and solves TDSE with FE-DVR / Lanczos / KSP for two-electron atoms. !
4  !-----!
5  ! Language : Fortran 90 !
6  ! Parallized : OMP,MPI !
7  ! !
8  ! Updated: included expokit;1 Ch imag. TDSE tested. Dec. 19, 2011 by iwaaw !
9  ! Updated: included anglib module,C-G,3j,6j,9j coef. Dec. 21, 2011 by iwaaw !
10 ! Updated: included laser field Dec. 22, 2011 by iwaaw !
11 ! Updated: 2d without correlation(1/|r12|) Dec. 25, 2011 by iwaaw !
12 ! Updated: changed to 2d with correlation(1/|r12|) Dec. 26, 2011 by iwaaw !
13 ! Updated: included laser field Jan. 10, 2012 by iwaaw !
14 ! Updated: OMP paralleled Jan. 20, 2012 by iwaaw !
15 ! Updated: Poisson sovled correlation(1/|r12|) Jan. 25, 2012 by iwaaw !
16 ! Updated: absorber added Feb. 08, 2012 by iwaaw !
17 ! Updated: pump-probe Mar. 22, 2012 by iwaaw !
18 ! Last updated : BB,SI,DI,Norm Oct. 05, 2012 by iwaaw !
19 !-----!
20 include "/lhome/iwaaw/linux/lib/anglib.f90"
21 include "f0includes.f90"
22 program helium_fedvr
23 use omp_lib
24 use accuracy_real
25 use globalmod_constants
26 use globalmod_discrete
27 use mymataid
28 use proppara
29 use anglib
30 use laser
31 use f00
32 use mpi
33 implicit none
34
35
36 write(idwrite,'(1x,a)') '-----'
37 write(idwrite,'(1x,a)') ' TAE-TDSE w/ Implimentation of FE-DVR in He Atom '
38 write(idwrite,'(1x,a)') '-----'
39 write(idwrite,*)
40 write(idwrite,*)
41 print*, '# Define ZERO as (1.d-80,0.d00)!'
42 call MPI_INIT( ierr )
43 call MPI_COMM_RANK( MPI_COMM_WORLD, myid, ierr )
44 call MPI_COMM_SIZE( MPI_COMM_WORLD, numprocs, ierr )
45

```

Figure E.1: A sample code of the file helium_fedvr.f90. The developing history of code is shown in comment lines.

E.3 Examples of Input Files

We here show examples for the input files parameter.inp and tdse.inp.

E.3.1 Example of “parameter.inp”

```
&HYDROGEN cnuclear =2, lang = 0, lmax=28 &END
&FEDVRDIS no_gp = 4, no_fe = 200, bound_start = 0.0, bound_end = 0.50, bslope = 0.0
&END
```

Description

The input file `parameter.inp` includes parameters for the one-electron FE-DVR scheme. In the first line, the list `HYDROGEN` includes three parameters. `cnuclear` is the nuclear charge of target, it is 1 for hydrogen or hydrogen-like targets, and 2 for helium atoms or TAE targets. `lang` and `lmax` are the minimal and maximum values of angular momenta. In TAE calculations, they will be reset by the configuration file.

In the second line, the list `FEDVRDIS` includes 5 parameters for FE-DVR method. `no_gp` is the number of grid points in one finite element, `no_fe` is number of finite elements in one radial coordinate. `bound_start` and `bound_end` are the start and end of first finite element. `bslope` is the slope of the FE-size increment. Set it to non-zero value for non-uniform FEs mapping.

E.3.2 Example of “tdse.inp”

1. *1. nL(# of config.), configuration file name*
2. *23 ~/lib/1112Llist333.txt*
3. *2. L0(max L1/L2 in init file), initial state filename,*
4. *3 init4x50*
5. *3. Lanczos order, tol*
6. *20 .1D-19*
7. *4. dt, start time, end time*
8. *0.005d0 0.d0 100.d0*
9. *5.(P1)IR energy(eV), # of IR cycles, intensity(E^2), CEP-IR(deg), delayIR(as)*

10.	42.d0	10	.5d15	0.d0	0.d0
11.6. <i>(P2)XUV energy(eV), # of XUV cycles, intensity(E^2), CEPXUV(deg), delayXUV(as)</i>					
12.	42.d0	10	0.d12	0.d0	0.d0
13.7. <i>absorb boundary (0:all,1:none, mostly 0.9)</i>					
14.	0.95d0				
15.8. <i>snapshot step, restart (1 Yes, else No), restart file #</i>					
16.	2000	0	1		
17.9. <i>static field</i>					
18.	0.d0				
19.10. <i>photon energy start (a.u.), photon energy end, photon energy step</i>					
20.	0.2	1.1	0.02		
21.11. <i>delay start (IR o.c.), delay end, delay step</i>					
22.	-2.0	2.0	0.05		

Description

- Lines 1-2: There are two parameters. The first one is the total number of partial waves employed E . It is shown in first line of the configuration file (e.g., `l112Llist333.txt`). The second parameter is the directory of the angular-momentum configuration file.

- Lines 3-4: Parameters for the initial state. $L_0 = 3$ for $(L, l_1, l_2)_{\max} = (3, 3, 3)$ configuration. The first four digits of line 4 are reserved for L_0 . The initial wave function is stored in the data file `init4x50`, which means that it has 4 grid points ($n = 4$) and 50 FEs ($m = 50$).

- Lines 5-6: Parameters for the wave-function propagating: Lanczos order and tolerance for each time step propagation.

- Lines 7-8: Time step, start time and end time for the propagation in atomic units. Remember to change the “start time” if you want to restart a calculation.

- Lines 9-10: The parameters for pulse 1 (laser field) with sin-squared profile. They

include photon energy (in eV unit), pulse duration (in unit of optical cycles), intensity (in unit of W/cm²), CEP phase (in unit of degree) and delay (in unit of as). The delay is the start point of sin-squared pulse; it is usually zero, but can be shifted.

- Lines 11-12: The parameters for pulse 2 (XUV pulse) with sin-squared profile. They include photon energy (in eV unit), pulse duration (in unit of optical cycles), intensity (in unit of W/cm²), CEP phase (in unit of degree) and delay (in unit of as). The delay is relative to the center of pulse 1.

If you want to perform a laser-free calculation, which has only one XUV pulse, the pulse 1 can serve as XUV pulse. Then set the intensity of pulse 2 as 0, as shown in the example above.

- Lines 13-14: To set up the absorption boundary. 0.95 means the wave function on the first 95% of grid points from 0 will not be absorbed, the absorber is applied to the outer 5% of grids.

- Lines 15-16: Snapshot and restart setting. To avoid data loss, we recommend to save intermediate data for the restart calculations. We save wave-function data every 2000×0.005 a.u. = 10 a.u. The restart parameter is set to 0 or 1 only. 1 means this is restarting calculation, and set the restarting file through “restart file #”. This “restart file #” must be consistent with the “start time” in lines 7-8.

- Lines 17-18: To set the parameter of the static field, if there is a static electric field presented.

- Lines 19-22: These four lines apply to ac-Stark shift and XUV transient-absorption calculations. They are disabled in most calculations. Uncomment the loops (lines 490/1042 and lines 491/1040.) in `helium_fedvr.f90` to enable them. Lines 17-18 set up the photon energy scale and step in atomic units; lines 19-20 set up the time delay setting in units of the IR laser optical cycles.

All source codes and sample input files are available upon request to collaborators and funding agencies.